

Washington University in St. Louis  
**Washington University Open Scholarship**

---

Engineering and Applied Science Theses &  
Dissertations

McKelvey School of Engineering

---

Summer 8-15-2018

# Bio-Inspired Multi-Spectral Image Sensor and Augmented Reality Display for Near-Infrared Fluorescence Image-Guided Surgery

Nan Cui

*Washington University in St. Louis*

Follow this and additional works at: [https://openscholarship.wustl.edu/eng\\_etds](https://openscholarship.wustl.edu/eng_etds)



Part of the [Electrical and Electronics Commons](#)

---

## Recommended Citation

Cui, Nan, "Bio-Inspired Multi-Spectral Image Sensor and Augmented Reality Display for Near-Infrared Fluorescence Image-Guided Surgery" (2018). *Engineering and Applied Science Theses & Dissertations*. 358.  
[https://openscholarship.wustl.edu/eng\\_etds/358](https://openscholarship.wustl.edu/eng_etds/358)

This Dissertation is brought to you for free and open access by the McKelvey School of Engineering at Washington University Open Scholarship. It has been accepted for inclusion in Engineering and Applied Science Theses & Dissertations by an authorized administrator of Washington University Open Scholarship. For more information, please contact [digital@wumail.wustl.edu](mailto:digital@wumail.wustl.edu).

WASHINGTON UNIVERSITY IN ST. LOUIS  
School of Engineering & Applied Science  
Department of Electrical and Systems Engineering

Dissertation Examination Committee:  
Shantanu Chakrabartty, Chair  
Viktor Gruev, Co-Chair  
Martin Arthur  
Roger Chamberlain  
Xuan Zhang

Bio-Inspired Multi-Spectral Image Sensor and Augmented Reality Display for Near-Infrared  
Fluorescence Image-Guided Surgery  
by  
Nan Cui

A dissertation presented to  
The Graduate School  
of Washington University in  
partial fulfillment of the  
requirements for the degree  
of Doctor of Philosophy

August 2018  
St. Louis, Missouri

© 2018, Nan Cui

# **Table of Contents**

List of Figures .....	v
List of Tables .....	ix
Acknowledgments.....	x
Abstract of the Dissertation .....	xi
Chapter 1: Introduction .....	1
1.1 Image-Guided Surgery with Fluorescent Molecular Markers.....	1
1.2 Research Goal and Achievements .....	5
1.3 Contributions of this Dissertation .....	5
1.4 Organization of this Dissertation.....	7
Chapter 2: Overview of FDA Approved Instruments for Fluorescence-Based Image-Guided Surgery .....	9
2.1 Requirements for Intraoperative Illumination and Intraoperative Imaging Instruments ....	10
2.2 FDA-Approved Instruments for NIR Fluorescence Image-Guided Surgery .....	13
2.2.1 Limited Dynamic Range in FDA Approved Instruments .....	14
2.2.2 Co-Registration Inaccuracy in FDA Approved Instruments.....	18
2.2.3 FDA Approved Instruments are Bulky and Interfere with the Surgical Workflow .....	22
Chapter 3: A Bio-Inspired 140 dB Dynamic Range 302 by 240 Resolution Color/Near-Infrared Logarithmic Imaging Sensor for Fluorescence-Guided Surgery .....	23
3.1 Introduction .....	23
3.2 Analysis on Logarithmic Pixel with Forward-Biased Photodiode.....	26
3.3 System Overview .....	30
3.4 Optoelectronic Characteristic Evaluation.....	31
3.5 Pre-clinical Evaluations and Animal Study .....	37
3.6 Conclusion and Discussion .....	40
Chapter 4: A 120 dB QVGA Resolution Time-Based Pulse-Width-Modulation Address-Event Representation Color-Infrared Imaging System for Fluorescence-Guided Surgery.....	43
4.1 Introduction .....	43
4.2 Time-Based PWM AER Color-Infrared Image Sensor.....	45
4.2.1 Sensor Architecture and AER Readout Scheme .....	46
4.2.2 Pixel Design .....	48

4.3 System Characterization.....	49
4.3.1 Spectral Response .....	49
4.3.2 Photo Response Non-Uniformity .....	51
4.3.3 Fluorescence Detectability .....	52
4.4 Pre-Clinical Studies .....	53
4.5 Imaging Tumors Under Surgical Light Illumination .....	54
4.6 Conclusions .....	55
Chapter 5: A Miniature Handheld Multi-Exposure Color/Near-Infrared Fluorescence Camera Prototype for Image-Guided Surgery.....	56
5.1 Introduction .....	56
5.2 System Overview of Handheld, Bio-Inspired Image Sensor .....	57
5.2.1 Custom Multi-Exposure Color/NIR CMOS Image Sensor.....	58
5.2.2 Pixelated Color/NIR Filters .....	62
5.2.3 Lens and Spectral Filter .....	63
5.2.4 Data Acquisition Module, Image Processing and Display.....	64
5.3 Optoelectronic Performance Evaluation .....	64
5.4 Imaging Spontaneous Tumors Under Surgical Light Illumination .....	71
5.5 Clinical Translation of My Bio-Inspired Technology .....	72
5.6 Conclusions .....	74
Chapter 6: Head-Mounted Augmented Reality System with Microsoft HoloLens for Near- Infrared Fluorescence-Based Image-Guided Surgery .....	76
6.1 Introduction .....	76
6.2 System Setup and Co-Registration Algorithm .....	79
6.2.1 System Setup.....	79
6.2.2 Co-Registration Algorithm .....	82
6.3 Input/Output Interface and Additional Features.....	85
6.4 System Evaluation.....	86
6.4.1 Sensitivity Evaluation .....	86
6.4.2 Resolution Evaluation .....	87
6.4.3 Co-Registration Evaluation.....	88
6.5 <i>In Vivo</i> and <i>Ex Vivo</i> Animal Study.....	90
6.6 Conclusions .....	91

Chapter 7: Conclusions and Future Work.....	93
7.1 Conclusions .....	93
7.2 Future Works .....	96
References .....	97

# List of Figures

Figure 1.1(a) Measured co-registration error between NIR and color image in FDA-approved Visionsense Iridium instrument. (b) and (c). Tumor-targeted agent correctly highlights the cancerous tissue at 15 °C (b), but at 35 °C the sciatic nerve (arrow) is tagged as cancerous tissue (c) due to temperature-induced co-registration error. ....	3
Figure 2.1 Modeling the dynamic range of an intraoperative imaging device for fluorescence-based image-guided cancer surgery. The dynamic range of an imaged scene exceeds 100 dB depending on the tumor location and concentration of molecular markers. ....	12
Figure 2.2 State-of-the-art image sensors utilize 4 transistors per pixel to achieve low readout noise. The transfer transistor coupled with pinned photodiode and peripheral correlated double-sampling circuitry enables removal of 1/f and reset noise. Hence, low readout noise of ~1 electron is achieved in today's state-of-the-art imagers. ....	14
Figure 2.3 Single-exposure cameras have limited capabilities for simultaneous imaging of color and near-infrared (NIR) images with high contrast under surgical light illumination. (a) Exposure time of 0.1 ms produces good color but poor NIR contrast images. (b) Exposure time of 40 ms produces oversaturated color image but good NIR contrast image. ....	18
Figure 2.4 Co-registration accuracy as a function of temperature. The instrument is calibrated at the starting temperature of 15 °C and achieves subpixel co-registration accuracy. However, when the instrument is heated up to 35 °C, the co-registration error increases up to 2.5 mm. When the instrument is cooled, different co-registration errors are observed. ....	19
Figure 2.5 Color/ NIR composite images recorded with a beam-splitter NIRF system while the instrument is at an operating temperature of (a) 15°C and (b) 32°C. ....	21
Figure 3.1 Pixel schematic. The sensor has QVGA resolution. Three registers control the reset and readout sequence. The pixel architecture is inspired by traditional active pixel sensor (APS) with a forward-biased photodiode. ....	27
Figure 3.2 Noise equivalent circuits for the logarithmic pixel with forward-biased photodiode. ....	29
Figure 3.3 Sensor architecture (left), the micrograph of the image sensor, and the micrograph of the pixelated spectral filter array (right). The QVGA resolution pixel array is addressed by 3 register banks. The output is digitized by a 14-bit ADC. ....	30
Figure 3.4 Measured signal and noise of a single on-chip photodiode.....	31
Figure 3.5 Logarithmic photo-response of the sensor. ....	32
Figure 3.6 The sensitivity of the image sensor. It is inverse-proportional to the optical power of the illumination. ....	33
Figure 3.7 Temporal noise of the sensor. The forward-biased diode's noise can be modeled by a noise-less resistor with a noise current source in parallel.....	34
Figure 3.8 Signal to noise ratio at different signal levels. 56dB SNR is achieved. ....	35
Figure 3.9 FPN of the sensor (left) and the histogram of the NIR channel at 1mW/cm <sup>2</sup> (right). ....	36

Figure 3.10 Histogram of the NIR channel at dark. The DCNU is 0.05%. The DDS removes most of the non-uniformity. ....	36
Figure 3.11 Quantum efficiency of the red, green, blue and NIR channels. ....	37
Figure 3.12 Comparison between the LDR color sensor (a) and this HDR color/NIR sensor (b,c,d). The commercial LDR sensor is not able to capture the details in the LED panel nor the vial in front of it (a). However, this HDR sensor can capture both HDR color image (b) and NIR image (c). The color and NIR images can be seamlessly superimposed (d). ....	38
Figure 3.13 Fluorescence detection limits. This sensor can detect as low as 40 nM ICG at 20 mW/cm <sup>2</sup> NIR excitation. ....	39
Figure 3.14 (a) Color image, (b) NIR fluorescence image and (c) superimposed image of a mouse with cancer. Tumor-targeted contrast agent was injected 24 hours before imaging. ....	40
Figure 3.15 Future 2-transistor pixel schematic. ....	42
Figure 4.1 (a) Traditional APS pixels. All pixels are exposed to light for the same amount of time. The dark pixels have a smaller voltage drop, while the bright pixels have a larger voltage drop. (b) Time domain PWM sensor. All pixels are discharged to the same voltage level. It takes the dark pixels a longer time to reach this voltage level, while it takes a shorter time for the bright pixels. ....	46
Figure 4.2 Sensor architecture and micrograph. ....	47
Figure 4.3 Pixel circuit. ....	48
Figure 4.4 Quantum efficiency of the imaging system. Blue, green, red, and NIR pixels have ~3%, 13%, 17% and 13% peak QE. Note that I added a 780-nm notch filter to block the NIR laser excitation, which leads to the QE around 780 nm being negligible. ....	50
Figure 4.5 FPN of the imaging system. (left) Before calibration, the FPN is between 3% and 7.5%, and (right) after calibration, the FPN drops down to less than 2%. ....	51
Figure 4.6 Signal to noise ratio of the imaging system. The SNR maintains 56 dB for 6 decades of different illumination. It drops at low optical power due to the readout noise. ....	52
Figure 4.7 Fluorescence detectability. This imaging system can detect as low as ~50 nM of ICG at 20 mW/cm <sup>2</sup> NIR excitation. ....	53
Figure 4.8 Image of the glass vial containing QDot800. A vial of water is placed next to it for comparison. The NIR image is correctly superimposed on the vial of Qdot800. ....	54
Figure 4.9 Color image, NIR fluorescence image and superimposed image of a mouse with ICG injected into the kidney. ....	54
Figure 5.1 System overview (a): System block diagram showing the fluorescence contrast agent injected into the patient's body prior to imaging. A NIR laser excites the fluorophore, and the custom image sensor captures the NIRF emission. The data are buffered by the field-programmable gate array (FPGA) data acquisition module and transferred to a PC. (b) Miniature image sensor next to a penny for scale. (c) Handheld prototype of my imaging device used during surgery. ....	58



Figure 5.2 (a) Circuit diagram of the image sensor. The pixel topology consists of a 2 by 2 super pixel pattern repeated across the 110 by 64 imaging array. (b) Chip micrograph.....	60
Figure 5.3 (a) Schematic of the pixel utilized in my custom image sensor. The typical 4-transistor active pixel architecture uses a shared reset and output bus to increase the fill factor. (b) Timing diagram of the read-out sequence. The multi-exposure readout scheme increases the signal level of the NIR channel.....	61
Figure 5.4 SEM micrograph of the interference filter and the underlying pixel. The interference filter is realized by alternatively stacking dielectric layers with high and low indices of refraction. ....	63
Figure 5.5 Block diagram of the optical setup for optoelectronic characterization of my custom multispectral image sensor.....	65
Figure 5.6 Quantum efficiency of the image sensor. Peak QE of the color and NIR channel are 18% and 8.5%. ....	66
Figure 5.7 Divergence response of the interference filter. The cutoff wavelength decreases as the incident angle increases. This is called the “blue-shift” effect. Blue shift will cause leakage of NIR excitation as well as visible illumination to the NIR channel, which degrades the NIR image quality and the fluorescence detection limit.....	67
Figure 5.8 (left) Uncalibrated FPN versus signal level. The FPN increases monotonically with signal level. The maximum FPN is 16% (color channels) and 11% (NIR channel) at full well. (right) Calibrated FPN versus signal level. The FPN is less than 2% for all intensities. ....	68
Figure 5.9 Signal-to-noise ratio versus signal level. At low illumination levels, the readout noise dominates the signal, whereas at a high illumination levels, the photon shot noise dominates the output signal. ....	69
Figure 5.10 Sensitivity for different ICG concentrations. The horizontal dashed lines represent the detection limit, while the solid lines represent the photo response. The multi-exposure sensor can detect 50 nM ICG.....	71
Figure 5.11 In vivo preclinical mouse study. NIR images use jet color map. (a) Single-exposure NIR image; (b) multi-exposure NIR image; (c) color image; (d) superimposed image. ..	72
Figure 5.12 Human SLN surgery study. NIR images use jet color map. (a) Single-exposure NIR image; (b) multi-exposure NIR image; (c) color image; (d) superimposed image.....	74
Figure 6.1 Comparison between the monitor-based display (left) and augmented reality-based display (right). Instead of displaying both the virtual NIRF image and virtual color image on a monitor, the augmented reality-based display system superimposes the virtual NIRF image directly on top of the patient’s body. ....	78
Figure 6.2 Augmented reality imaging system for NIRF IGS. (a) System setup including a custom NIR camera, a wireless router, a 780-nm laser with its optics, a calibration board and a HoloLens. (b) User wearing the HMD.....	80

Figure 6.3 Typical signal flow using augmented reality for NIRF IGS. The custom NIR camera captures the NIRF from the target and sends the raw data to a PC. The processed data are sent wirelessly to the HoloLens. ....	82
Figure 6.4 Co-registration calibration algorithm flow chart. ....	85
Figure 6.5 Pre-loaded CT images with the real-time NIR hologram. All commands such as zoom in/out of the CT images and going to next page is voice and gesture controlled. ....	86
Figure 6.6 Contrast of the imaging system. The red line represents the contrast for each ICG concentration level. The horizontal blue line represents contrast equal to 2. The augmented reality system can detect as low as ~10 nM ICG under an excitation illumination of 20 mW/cm <sup>2</sup> . ....	87
Figure 6.7 Horizontal and vertical modulation transfer function. The horizontal blue line represents the contrast under the Rayleigh criterion. The augmented reality system's resolution is 23.6 lp/mm and 29.8 lp/mm horizontally and vertically. ....	88
Figure 6.8 Co-registration error model. The error is a function of the target height and viewing angle. ....	89
Figure 6.9 Co-registration error from a 60-degree viewing angle. ....	90
Figure 6.10 In vivo (left) and ex vivo (right) animal study for SNL removal assisted by the augmented reality HMD .....	91

# **List of Tables**

Table 2.1 Summary of the FDA-approved intraoperative NIRF imaging instruments .....	14
Table 3.1 Design summary and comparison with the state-of-the-art linear CMOS sensors.....	41
Table 3.2 Design summary and comparison with the state-of-the-art logarithmic sensors.....	41
Table 5.1 The summary and comparison between this multi-exposure multispectral image sensor and related work.....	69
Table 6.1 Summary and comparison between this augmented reality HMD and related work ...	92
Table 7.1 Design Summary of this work and comparison with the FDA-approved instruments. .....	95
Table 7.2 The comparison between the major contribution of this dissertation and the state-of- the-art low-noise high-dynamic-range image sensor.....	95

# **Acknowledgments**

I would especially like to thank Dr. Viktor Gruev for his guidance and encouragement during the years I pursued my doctoral degree. Without his support, I could not have continued my academic journey. I would also especially like to thank Dr. Shantanu Chakrabartty for serving as my dissertation defense committee chair. I would also like to thank my dissertation committee members for their time, patience and precious feedback. Finally, I would like to thank my family, lab mates and friends who have supported me financially, technically and spiritually during these years.

Nan Cui

*Washington University in St. Louis*

*August 2018*

## ABSTRACT OF THE DISSERTATION

### Bio-Inspired Multi-Spectral Image Sensor and Augmented Reality Display for Near-Infrared Fluorescence Image-Guided Surgery

by

Nan Cui

Doctor of Philosophy in Electrical Engineering

Washington University in St. Louis, 2018

**Background:** Cancer remains a major public health problem worldwide and poses a huge economic burden. Near-infrared (NIR) fluorescence image-guided surgery (IGS) utilizes molecular markers and imaging instruments to identify and locate tumors during surgical resection. Unfortunately, current state-of-the-art NIR fluorescence imaging systems are bulky, costly, and lack both fluorescence sensitivity under surgical illumination and co-registration accuracy between multimodal images. Additionally, the monitor-based display units are disruptive to the surgical workflow and are suboptimal at indicating the 3-dimensional position of labeled tumors. These major obstacles have prevented the wide acceptance of NIR fluorescence imaging as the standard of care for cancer surgery. The goal of this dissertation is to enhance cancer treatment by developing novel image sensors and presenting the information using holographic augmented reality (AR) display to the physician in intraoperative settings.

**Method:** By mimicking the visual system of the *Morpho* butterfly, several single-chip, color-NIR fluorescence image sensors and systems were developed with CMOS technologies and pixelated interference filters. Using a holographic AR goggle platform, an NIR fluorescence IGS display system was developed. Optoelectronic evaluation was performed on the prototypes to evaluate the performance of each component, and small animal models and large animal models were used to verify the overall effectiveness of the integrated systems at cancer detection.

**Result:** The single-chip bio-inspired multispectral logarithmic image sensor I developed has better main performance indicators than the state-of-the-art NIR fluorescence imaging instruments. The image sensors achieve up to 140 dB dynamic range. The sensitivity under surgical illumination achieves  $6 \times 10^8 \mu\text{V}/(\text{mW}/\text{cm}^2)$ , which is up to 25 times higher. The signal-to-noise ratio is up to 56 dB, which is 11 dB greater. These enable high sensitivity fluorescence imaging under surgical illumination. The pixelated interference filters enable temperature-independent co-registration accuracy between multimodal images. Pre-clinical trials with small animal model demonstrate that the sensor can achieve up to 95% sensitivity and 94% specificity with tumor-targeted NIR molecular probes. The holographic AR goggle provides the physician with a non-disruptive 3-dimensional display in the clinical setup. This is the first display system that co-registers a virtual image with human eyes and allows video rate image transmission. The imaging system is tested in the veterinary science operating room on canine patients with naturally occurring cancers. In addition, a time domain pulse-width-modulation address-event-representation multispectral image sensor and a handheld multispectral camera prototype are developed.

**Conclusion:** The major problems of current state-of-the-art NIR fluorescence imaging systems are successfully solved. Due to enhanced performance and user experience, the bio-inspired sensors and augmented reality display system will give medical care providers much needed technology to enable more accurate value-based healthcare.

# **Chapter 1: Introduction**

Cancer remains a major public health problem in the US and poses a huge economic burden [1]. One in four deaths in the US is caused by cancer [2]. Although chemotherapy and radiotherapy continue to play major roles in cancer treatment, surgery remains the primary curative option for most solid cancers[3]. Despite advancements of imaging technologies in the operating room, an overwhelming majority of physicians still rely on their unaided eyes and palpation to distinguish cancerous from healthy tissue, leading to subjective decision making and variable outcomes. Studies show that incomplete tumor resections are observed in all types of cancer, for example, 20-70% for breast cancer [4, 5], 28% for colon cancer [6] and 40% for head and neck cancer [7]. Secondary surgeries not only are expensive but also have limited success because of the difficulty in seeing microscopic tumors or diffuse cells. Additionally, scar tissue formation perturbs the surgical planes, making it more difficult for the physician to identify the remaining tumor tissue. These studies underscore the importance of complete tumor removal during the first surgery and the need for a paradigm shift in the design of imaging systems for image-guided surgery (IGS).

The remainder of this chapter will provide an overview of the current state-of-the-art image guided surgical instruments. I will highlight the major issues with FDA approved instruments for IGS and will outline my research contributions in this thesis.

## **1.1 Image-Guided Surgery with Fluorescent Molecular Markers**

Fluorescence-based intraoperative imaging techniques were first explored in the 1950s using fluorescein to identify brain tumors [8]. With the recent FDA approval of the metabolic marker 5-

ALA, brain cancer surgery is routinely performed under image guidance [9]. The visible-spectrum fluorescence emitted by both fluorescein and 5-ALA enables physicians to assess the location of tumors under a surgical microscope. However, due to tissue's high absorption coefficients in the visible spectrum, only fluorophores near the tissue surface can be imaged, which limits their diagnostic potential. For imaging more than a few millimeters below the surface of the skin, near infrared (NIR) fluorophores (700 to 950 nm) are used because of the low absorption coefficient of water and oxy- and deoxy-hemoglobin in this spectrum [10-12]. Furthermore, the low autofluorescence in the NIR spectrum coupled with the use of non-ionizing radiation enable high-contrast imaging without exposing the patient to harmful radiation [13].

There are currently only two FDA-approved, non-specific molecular markers with NIR fluorescence (NIRF): indo-cyanine green (ICG) and methylene blue [11]. Both markers are used either for mapping the primary draining lymphatic nodes near the tumor site, known as sentinel lymph nodes (SLNs), or for assessing blood perfusion in tissue [14]. Preliminary results from our lab on 11 patients with breast cancer [15, 16] concur with other published studies [17] that NIRF from ICG has higher sensitivity for identifying SLNs than does visible inspection of ICG or radioactive tracers. Despite these promising results, fluorescence-based SLN mapping using ICG is not currently adopted as the standard of care during oncology procedures.

- **Inaccuracy of Intraoperative NIRF Instruments:** The FDA stipulates several criteria for intraoperative use of NIRF instruments [10-12], including a minimum range of operational temperatures between 10 °C and 35 °C. The reason for the large operational temperature range is that large thermal gradients exist within standard operating rooms (ORs) due to building cooling and heating, and these ranges are even greater for ORs outside the US. Current FDA-



approved instruments combine at least two separate image sensors, one for visible-spectrum imaging and one for NIR imaging, with optimized dichroic beam splitters and spectral filters [15]. Since each individual component has a different thermal expansion coefficient, co-registration between color and NIRF images is a function of temperature. Although the FDA does not yet stipulate any co-registration accuracy, the preliminary data indicate co-registration errors in FDA-approved instruments ranging from several millimeters to a centimeter within the 10-35 °C range (Figure 1.1(a)).

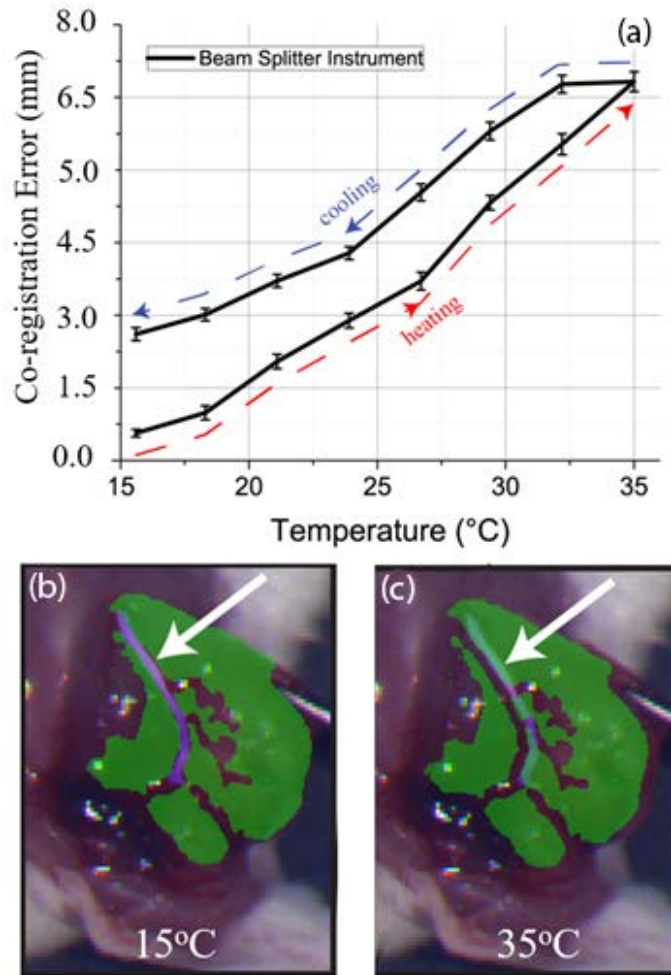


Figure 1.1(a) Measured co-registration error between NIR and color image in FDA-approved Visionsense Iridium instrument. (b) and (c). Tumor-targeted agent correctly highlights the cancerous tissue at 15 °C (b), but at 35 °C the sciatic nerve (arrow) is tagged as cancerous tissue (c) due to temperature-induced co-registration error.

By gradually heating and then cooling the instruments, different co-registration errors are observed at the same temperatures, which makes off-line corrections intractable. The co-registration errors result in incorrect superposition of tumor-targeted tissue on anatomical features (Figure 1.1 (b), (c)). Superposition can lead to incomplete resection of tumor tissue and iatrogenic damage of healthy tissue and is a liability for FDA-approved instruments.

- **Intraoperative Display Devices:** Displaying information in the OR without intruding in the surgical flow is a major challenge for IGS. Three-dimensional real-world information is projected on two-dimensional monitors, resulting in loss of important depth information. Wearable goggles are ideal for displaying information in the OR: they provide protection to the physician's eyes and can present 3-D information to the operator without interfering in the surgical workflow. In our previous research, we integrated various types of video- [18] and see-through [19-21] goggles with beam-splitter multispectral cameras and provided real-time information to physicians about the location of SLNs in patients with breast cancer. One of the major shortcomings of our goggle technology is the fact that NIR fluorescence information is not co-registered with the physician's natural vision, which leads to confusion and distraction of the physician.

Despite the fact that the first fluorescence-based IGS was performed more than 70 years ago, two obstacles have stood between molecular imaging in the NIR spectrum and its wide acceptance as the standard of care for cancer surgery: (1) Current state-of-the-art NIRF imaging systems are bulky and costly—they use an external monitor to display information, which interferes with the surgical workflow—and they lack both sensitivity under surgical illumination and co-registration accuracy between multimodal images (Fig. 1) [10-12]. (2) Large molecular markers targeting monoclonal antibodies do not highlight proliferating tumor edges [22, 23]. Tumor detection can

be further improved by utilizing small molecular probes targeting affibodies or peptides, instead of large, monoclonal antibody (mAb) probes [22, 24]. Due to the small size of affibody-based molecular probes, unbound tracer is quickly removed from blood and normal tissue, and the patient is typically imaged 2-6 hours post-injection, whereas mAb-based markers take 3 to 7 days to clear from normal tissue [25, 26]. Thus, affibody- and peptide-based markers can enable same-day administration of the probe and surgery, thereby reducing hospital stays and overall treatment costs [23, 27].

## **1.2 Research Goal and Achievements**

The overarching goal of this dissertation is to enhance cancer treatment by decreasing, and ideally eliminating, positive tumor margins and small metastatic tumors by imaging small tumor-targeted molecular probes with novel bio-inspired image sensors and presenting this information using holographic display to the physician in intraoperative settings. I have leveraged complementary, small molecular probes targeting different tumor marker antigens to highlight tumor margins and small tumors during surgery. I have tested my complete imaging system on both small and large animals with naturally occurring tumors. My pre-clinical data reveals high sensitivity of my imaging system to NIR-fluorescent molecular markers under surgical light conditions. Furthermore, the integration of my bio-inspired imaging system with wearable holographic augmented reality (AR) goggles enables seamless integration in the surgical workflow.

## **1.3 Contributions of this Dissertation**

Toward achieving the overarching goal of this thesis, I have made several key contributions outlined below:

1. To address the high dynamic range and low-noise imaging requirements in the operating room, I developed a bio-inspired, single-chip, visible-NIR fluorescent image sensor with dynamic range exceeding 140 dB (120 dB logarithmic response). The image sensor successfully mimics the visual system of the *Morpho* butterfly by utilizing (a) logarithmic photodetector necessary to image scenes with dynamic range exceeding 140 dB and (b) pixelated spectral filters necessary to simultaneously image both visible and NIR spectra. The image sensor was designed and fabricated in a standard 0.35 $\mu$ m CMOS process by TSMC. Pixelated spectral filters were integrated with the CMOS image sensor in the cleanroom facilities at University of Illinois. I performed detailed optoelectronic evaluation of the image sensor and then tested the sensor's ability to detect and specify tumors with small NIR fluorescent molecular markers. Due to the low read-out noise and high dynamic range, the sensor achieved ~95% sensitivity and ~94% specificity in detecting orthotopic prostate cancers in murine models when imaged under surgical light illumination.
2. To address changes in displaying information in the operating room without intruding in the surgical work flow, I integrated my bio-inspired image sensor with a holographic AR goggle platform to display real-time NIR fluorescent information to the physician. My key contribution is the accurate co-registration of NIR fluorescent information with the physician's natural eyesight. With the complete imaging and display system, the physician observes the patients with his or her natural eyesight, which is augmented with NIR information that highlights the location of the tumors. The imaging system was tested in the veterinary science operating room on canine patients with naturally occurring cancers. According to the feedback from the veterinarian physician, my system provided critical information about the location of the lymphatic nodes during the surgery without intruding in the surgical workflow.

3. To ensure that there are no cancerous cells left in the patient's body, I developed a handheld imaging device that can provide close inspection of the surgical cavity. The imaging platform, inspired by the visual system of the *Morpho* butterfly, combines a custom designed CMOS image sensor in 180nm image specific technology with pixelated spectral filters. My CMOS image sensor contains custom circuitry that enables high-dynamic-range imaging under surgical light illumination. Due to the monolithic integration of spectral filters with CMOS imaging elements, the NIR-fluorescent information is correctly reregistered with color information over large temperature range. I could achieve accurate temperature-independent image co-registration compared to state-of-the-art, FDA approved imaging instruments.
4. To address the high dynamic range needs for intraoperative procedures, I designed the first time-domain pulse-width-modulation (PWM) address-event representation (AER) multispectral imaging system. The AER image sensor provides temporal information when a corresponding pixel in the array has relevant information. The pixel's address is reported outside the image sensor when its intensity value crosses a user-set threshold value, and an external processing unit aggregates and displays the image information. The monolithic integration of the AER image sensor with a pixelated spectral filter array enables imaging of weak fluorescent signals under bright surgical light illumination. The image sensor was able to detect tumors with 85% sensitivity and 87% specificity when an antibody-targeted molecular marker was used.

## **1.4 Organization of this Dissertation**

This dissertation is organized as follows. Literature overview and motivation for fluorescence-based image-guided surgery is presented in Chapter 2. A bio-inspired, high dynamic range, multispectral image sensor based on logarithmic domain pixel is presented in Chapter 3. Chapter

4 describes a time-domain pulse-width-modulation address-event representation bio-inspired multispectral imaging system. Chapter 5 presents a handheld, bio-inspired multispectral image sensor for image-guided cancer surgery. Chapter 6 describes my work on the holographic AR goggles display unit integrated with a bio-inspired image sensor for real-time assessment of tumors and lymphatic nodes in large animals with naturally occurring tumors. Concluding remarks are presented in Chapter 7.

## **Chapter 2: Overview of FDA Approved Instruments for Fluorescence-Based Image-Guided Surgery**

The goal of image-guided surgery (IGS) is to provide critical information to the physician about the location of tumor vs. healthy tissue during intraoperative procedures. Various techniques have been developed for IGS, including: x-ray imaging, two-photon imaging, fluorescence and others. Fluorescence imaging is of particular interest because it utilizes fluorescent molecular markers to highlight the location of the cancerous tissue and enables high signal-to-background imaging. Fluorescence imaging in the near infrared (NIR) spectrum (wavelengths from 700 nm to 1000 nm) has gained lot of traction during the last decade for numerous reasons. First, due to tissue's low absorption and scattering coefficient in the NIR spectrum, NIR photons can travel and penetrate several centimeters deep in the tissue [10-12]. Second, the low auto-fluorescence in the NIR spectrum coupled with the use of non-ionizing radiation enables high-contrast imaging without exposing the patient to harmful radiation [13]. Third, the human eye is invisible to the NIR spectrum. Hence, imaging in the NIR spectrum does not interfere with or obstruct the physician's natural vision. However, specialized image sensors are needed to sense NIR photons.

Despite the fact that the first fluorescence-based IGS was performed more than 70 years ago, molecular imaging in the NIR spectrum is not widely accepted as the standard of care for cancer surgery because (1) current state-of-the-art NIRF imaging systems are bulky and costly; they use an external monitor to display information, which interferes with the surgical workflow, and they lack both sensitivity under surgical illumination and co-registration accuracy between multimodal

images [10-12]; and (2) large-size molecular markers targeting monoclonal antibodies do not highlight proliferating tumor edges [22, 23].

This chapter first outlines the Food and Drug Administration (FDA) requirements for intraoperative procedures, then describes in detail the shortcomings of current FDA-approved instruments which are preventing wide dissemination of newer instruments.

## **2.1 Requirements for Intraoperative Illumination and Intraoperative Imaging Instruments**

The goal of NIR fluorescence-based image-guided cancer surgery is to simultaneously capture both visible and NIR images. NIR fluorescence images capture only information about the location of the molecular fluorescent dye and lack any anatomical information. Fluorescent images resemble a bright spot against a black background. Hence, the location of the fluorescent marker is needed so that the physician can correctly remove all cancerous tissue without damaging healthy tissue. Therefore, the patient wound site must be illuminated with both visible and NIR spectra and imaged with sensors that can capture photons in both spectra.

The FDA regulates the optical properties for both visible and NIR light sources, such as maximum optical power, temperature color and color rendering index among others. Surgical light sources must adhere to the following FDA requirements to be used in the operating room. First, the optical power for visible spectrum illumination must be between 40 kLux and 160 kLux. Second, the color temperature of the light source must be between 3000 K and 6700 K. Third, the color rendering index must be greater than 0.85. To excite NIR fluorophores from tumor targeted dyes, laser light illumination is preferred over LED-based illumination because of the higher excitation optical power over a narrow spectral bandwidth. The narrower spectral bandwidth is important when



imaging molecular markers with small Stokes shift, i.e. the difference between the maximum absorption and maximum emission of the molecular marker. The maximum optical power for laser-based illumination at 780 nm without inflicting tissue damage is approximately 150 mW/cm<sup>2</sup>. However, protective laser goggles are required for everyone in the operating room, including the patient, posing an immense hurdle for seamless integration of this technology in the operating room. Hence, maximum laser light illumination at 780 nm is typically limited to 10 mW/cm<sup>2</sup> in the operating room because protective goggles are not necessary.

- Dynamic Range Requirements for Intraoperative Imaging Devices:** An image sensor for fluorescence-based IGS must simultaneously capture both visible and NIR photons. Next, I consider the photon flux from both visible and NIR photons impinging on an image sensor during an intraoperative procedure of a patient model with a tumor that is 5 mm beneath the surface (Figure 2.1). I will assume that the visible spectrum illumination is 40 kLux and NIR laser-based excitation power is 10 mW/cm<sup>2</sup>. Based on this assumption, the visible spectrum illumination sources will generate  $\sim 4 \times 10^{16}$  photons/cm<sup>2</sup>\*sec. Since the index of refraction for human skin is between 1.33 and 1.51, about  $1 \times 10^{15}$  photons/cm<sup>2</sup>\*sec will be reflected based on Snell's law for reflection. The reflected photon flux will be recorded by the imaging instrument placed 1 m above the patient's body and a color image will be formed.

The 780 nm laser light source will generate  $8 \times 10^{16}$  photons/cm<sup>2</sup>\*sec NIR photons and impinge on the patient's body. About  $4 \times 10^{15}$  photons/cm<sup>2</sup>\*sec NIR photons will get reflected from the patient's body and will impinge on the image sensor. These photons must be blocked with high-optical-density spectral filters because they carry no information about the fluorescent markers. The photons that are refracted in the patient's body will undergo multiple scattering

and absorption events. About  $4 \times 10^{14}$  photons/cm<sup>2</sup>\*sec NIR photons will reach the tumor and excite fluorophores from the tumor targeted dye. If the quantum yield and concentration of the molecular marker are 5% and 10μM, respectively, then approximately  $1 \times 10^{13}$  photons/cm<sup>2</sup>\*sec fluorescent photons will be radially emitted by the molecular marker. Some of fluorescent photons will travel back toward the surface, where they will undergo multiple scattering and absorption events. Lastly,  $6 \times 10^{10}$  photons/cm<sup>2</sup>\*sec fluorescent photons will emerge from the tissue into air and will be registered by the image sensor. Hence, the image sensor has to capture both color and NIR photons with 100 dB difference in photon flux. This difference is further exacerbated if the tumor is located deeper in the tissue and the fluorophen concentration is lower than that assumed in this example. Hence, an image sensor must have at least 100 dB dynamic range imaging capabilities for successful clinical translation.

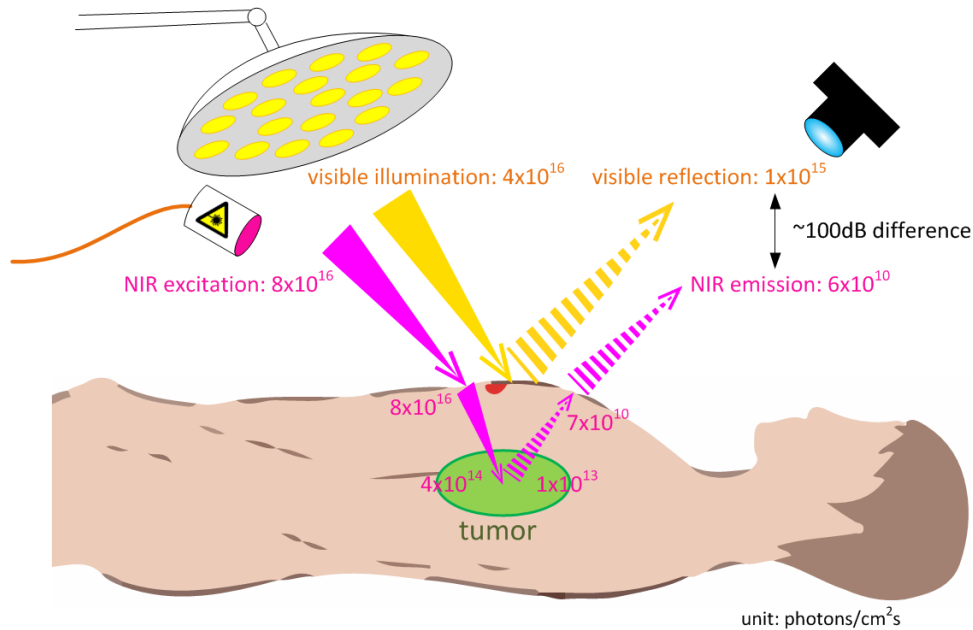


Figure 2.1 Modeling the dynamic range of an intraoperative imaging device for fluorescence-based image-guided cancer surgery. The dynamic range of an imaged scene exceeds 100 dB depending on the tumor location and concentration of molecular markers.

The FDA regulations also require the operational temperature for intraoperative imaging instruments to be between 10 °C and 35 °C. The reason for this large operating temperature range is because temperature gradients in the operating room are common due to room heating and cooling. Although the average temperature in the operating room is typically between 18 °C and 20 °C, large temperature gradients across the operating room are observed. The optoelectronic performance of the imaging device, such as co-registration accuracy between NIR and visible images, across this temperature range should be critically evaluated. Unfortunately, FDA does not have any requirements about the co-registration accuracy between these two imaging modalities and FDA-approved instrument lack co-registration accuracy.

## **2.2 FDA-Approved Instruments for NIR Fluorescence Image-Guided Surgery**

There are currently five FDA approved imaging devices for fluorescence-based NIR image-guided surgery (see Table 2.1). All FDA approved instruments are based on a beam splitter design: two separate image sensors are combined together with a beam splitter and spectral filters and used to separately capture visible and NIR spectrum photons. The visible image sensor captures photons with wavelengths between 400 nm and 650 nm, and the NIR image sensor captures photons with wavelength between 650 nm and 1000 nm. The visible spectrum image is enhanced with the NIR fluorescent image, which provides the location of the cancerous tissue. It is imperative that these two images are correctly co-registered across all possible operating conditions, including the specified operating temperature range of 10 °C and 35 °C. However, FDA approved instruments have three major shortcomings, which can explain the limited dissemination of these instruments in the operating room: limited dynamic range imaging capabilities, temperature-dependent co-registration inaccuracy and large footprint which intrudes on the surgical workflow.

Table 2.1 Summary of the FDA-approved intraoperative NIRF imaging instruments

Description	Fluobeam	PDE	SPY Elite	Iridium	Spectrum
Designer	FluoOptics	Hamamatsu	Novadaq	Vision Sense	Quest
Instrument type	Single camera	Single camera	Two adjacent cameras	Beam splitter	Optical prism
Real-time color/NIR overlay	No	No	No	Yes	Yes
Surgical light	Dim	Dim	Dim	Dim	On
Sensor bit depth	8	8	8	12	12
Exposure time	1 ms to 1 s	NS	NS	NS	NS
Maximum FPS	25	20	20	NS	20
Resolution	$720 \times 576$	$640 \times 480$	$1024 \times 768$	$960 \times 720$	$1024 \times 1024$
Fluorescence Detection Limit	$\sim 5$ nM	$\sim 15$ nM	$\sim 5$ nM	$\sim 50$ pM	$\sim 10$ nM

### 2.2.1 Limited Dynamic Range in FDA Approved Instruments

FDA approved instruments have low dynamic range of  $\sim 80$  dB. Since the dynamic range in the operating room exceeds 100 dB, the physician has to stop the surgery, dim the surgical lights, use the imaging instrument to identify the location of the fluorescent markers and then continue the surgery without guidance under normal surgical illumination conditions. The limited dynamic range is a result of using current state-of-the-art CMOS imagers based on a 4 transistor per pixel paradigm (Figure 2.2).

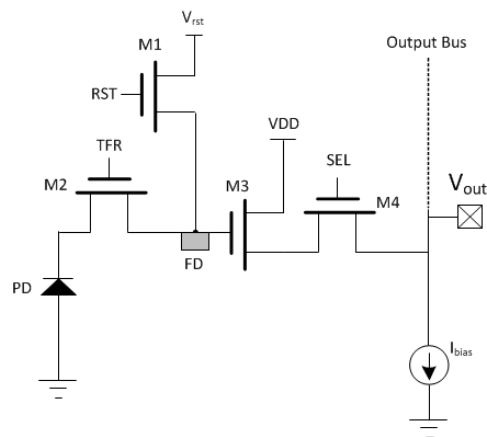


Figure 2.2 State-of-the-art image sensors utilize 4 transistors per pixel to achieve low readout noise. The transfer transistor coupled with pinned photodiode and peripheral correlated double-sampling circuitry enables removal of  $1/f$  and reset noise. Hence, low readout noise of  $\sim 1$  electron is achieved in today's state-of-the-art imagers.

State-of-the-art image sensors have pixels comprised of 4 transistors: a reset transistor  $M_1$ , a charge transfer  $M_2$ , an amplifier  $M_3$  and a row select switch  $M_4$ . The switch transistor controls access to the pixel's output by the read-out bus and peripheral circuitry. The source follower buffers the integrated and reset voltage before providing the result to the readout bus. The transfer transistor is closely integrated with the pinned photodiode and enables charge transfer of the integrated photodiode voltage to the floating diffusion node. The gates of all transistors are controlled by digital circuits placed in the periphery of the imaging array. The pixel operates as follows. First the floating diffusion and photodiodes are reset to a reference voltage level,  $V_{rst}$ , by turning on both  $M_1$  and  $M_2$  transistors. Next, both  $M_1$  and  $M_2$  transistors are turned off and the photodiode integrates the incident photon converted to electron-hole pairs on its intrinsic capacitor.

After the end of the integration period, the pixel is accessed by turning on  $M_4$  transistor. During the read-out phase, first transistor  $M_1$  is pulsed and the output voltage is sampled on the peripheral correlated double sampling circuit, typically constructed using switch capacitor circuits. The output voltage from the pixel can be represented by equation (2.1):

$$V_{out1} = V_{rst} - V_{t3} - \sqrt{\frac{2I_{bias}}{k'W^3/L^3}} \pm V_{reset\ noise} \quad (2.1)$$

In equation (2.1),  $V_{rst}$  is the reference voltage to which the photodiode was set during the reset period;  $V_{t3}$  is the threshold voltage of the source follower transistor  $M_3$ ; the third term on the right-hand side describes the contributions of the biasing current for the source follower; and the last term is the reset noise, which is equal to  $kT/C$ .

Once the reset voltage is sampled in the peripheral circuitry, the transfer transistor is turned on and integrated photodiode charges are transferred on the floating diffusion node. The output voltage at this point can be represented by equation (2.2):

$$V_{out2} = V_{photo} - V_{t3} - \sqrt{\frac{2I_{bias}}{k'W^3/L^3}} \pm V_{reset\ noise} \pm V_{shot\ noise} \quad (2.2)$$

In equation (2.2),  $V_{photo}$  is the integrated photodiode voltage and  $V_{shot\ noise}$  is the noise associated with the photocurrent across the photodiode. Note that the photodiode is biased in reverse mode and the photocurrent linearly discharges the photodiode capacitance. High photon flux will generate more electron-hole pairs, which will lead to larger photocurrent. Hence, the photodiode voltage will discharge quicker when illuminated with higher light intensities. The reverse-bias photodiode enables a linear relationship between photocurrent and output voltage, which is desirable when generating color images.

Correlated double sampling (CDS) is a method whereby two samples with correlated noise sources are subtracted to provide an output with lower noise. CDS circuits in the periphery of the image sensor provide the final output by subtracting the voltage samples described by equations (2.1) and (2.2). The final output is described by equation (2.3):

$$V_{out} = V_{out1} - V_{out2} = V_{rst} - V_{photo} \pm V_{shot\ noise} \quad (2.3)$$

The shot noise term in equation (2.2) is proportional to the square root of the generated electron-hole pairs at the photodiode node. Shot noise is regarded as the limiting factor when imaging scenes with moderate to high light intensities, while readout noise, i.e. temporal noise associated with all transistors in the pixel and read-out circuitry, is the limited factor for low light imaging applications. Furthermore, the dynamic range of the pixel is defined as the ratio of the pixel well

depth capacity to the readout noise in dark. Since a state-of-the-art image sensor can achieve close to  $1e^-$  readout noise and have pixel well depth  $\sim 10 ke^-$ , the dynamic range of current state-of-the-art image sensor is around 80 dB. The dynamic range of the image sensor can be improved with multiple integration readout or by completely redesigning the pixel to fit the demands of the applications.

- **Imaging tumor bearing animals with FDA approved instrument under surgical illumination:** We demonstrate the limited dynamic range imaging capabilities of FDA approved instruments in a murine animal model of breast cancer. 4T1 breast cancer cells are orthotopically injected in the animal and left to grow for  $\sim 2$  weeks. A tumor-targeted agent is injected 24 hours prior to imaging the animals. The animal is imaged under 60 kLux surgical light illumination and laser light excitation power of  $5 \text{ mW/cm}^2$  at 785 nm. The objective is to provide a good SNR image for both color and NIR spectra to the end-user with an instrument with 80 dB dynamic range. The results are presented in Figure 2.3. The images in Figure 2.3 are obtained with exposure times of 0.1 ms and 40 ms, respectively. When the animal was imaged with an exposure time of 0.1 ms, the color image is well illuminated, while the NIR image has very low contrast. The animal was then imaged with 40 ms exposure time, resulting in a well-illuminated NIR image but a saturated color image. This is due to the large difference between the visible and NIR photon flux in the operating room. Utilizing a single exposure time in a pixelated camera enables only one of the two imaging modalities to have satisfactory contrast and high signal-to-noise ratio, rendering this technology incompatible with the demands of intraoperative imaging applications.

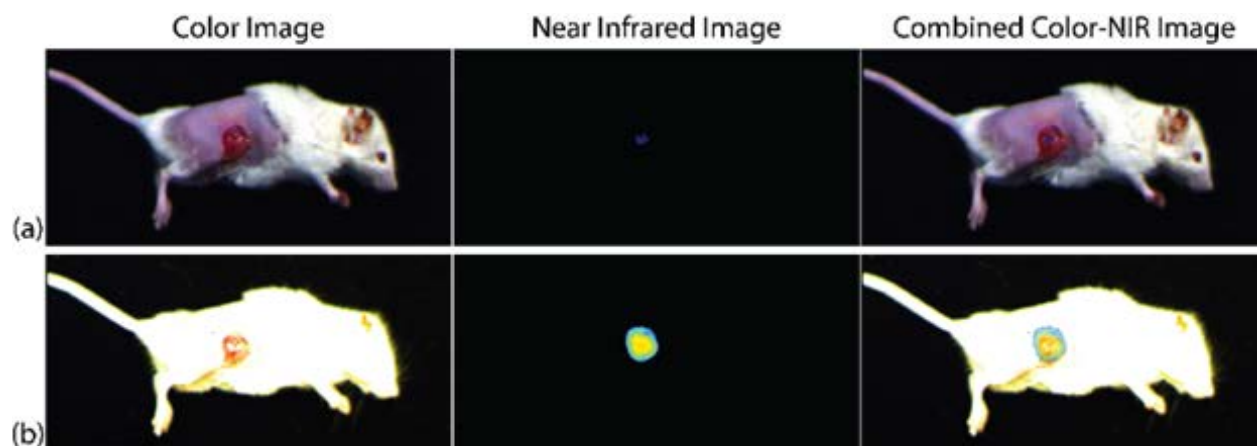


Figure 2.3 Single-exposure cameras have limited capabilities for simultaneous imaging of color and near-infrared (NIR) images with high contrast under surgical light illumination. (a) Exposure time of 0.1 ms produces good color but poor NIR contrast images. (b) Exposure time of 40 ms produces oversaturated color image but good NIR contrast image.

### 2.2.2 Co-Registration Inaccuracy in FDA Approved Instruments

Co-registration accuracy between color and NIRF images is one of the most important attributes for an instrument to be clinically relevant. Yet, state-of-the-art NIRF instrumentation comprising a beam splitter and dichroic mirrors suffers from temperature-dependent co-registration inaccuracy due to thermal expansion and thermal shifts of individual optical components. These FDA-approved instruments are rated to function between 10 °C and 35 °C, though they fail to maintain co-registration accuracy in this range.

We evaluated co-registration accuracy as a function of temperature for both our bio-inspired sensor and a state-of-the-art NIRF imaging system composed of a single lens, beam splitter, and two image sensors (Figure 2.4). The sensors were placed 60 cm from a calibrated checkerboard target to emulate the distance at which the sensor will be placed during preclinical and clinical trials. At the starting operating point, the beam-splitter NIRF system achieves subpixel co-registration accuracy using standard calibration methods. However, the disparity between the two images increases as the instrument's operating temperature increases, leading to large co-registration errors. And, as the instrument is cooled, the trajectory of the co-registration error differs from that



when the instrument is heated up. Hence, placing a temperature sensor on the instrument will not sufficiently correct for thermal expansion of the individual optical elements.

- **Clinical Implications for Co-Registration Inaccuracy:** The implication of the temperature-dependent co-registration error between the NIR and color images in state-of-the-art NIRF systems is demonstrated in a murine model where 4T1 cancer cells are implanted next to a sciatic nerve. At ~2 weeks post-implantation, the tumor size is ~1 cm and is imaged with the tumor-targeted agent. The animal is imaged with a beam-splitter NIRF image sensor placed inside a thermal chamber, which has a viewing port that allows imaging of the animal without perturbing the temperature of the instrument. The animal is kept on a heated thermal pad to maintain constant body temperature of ~37 °C.

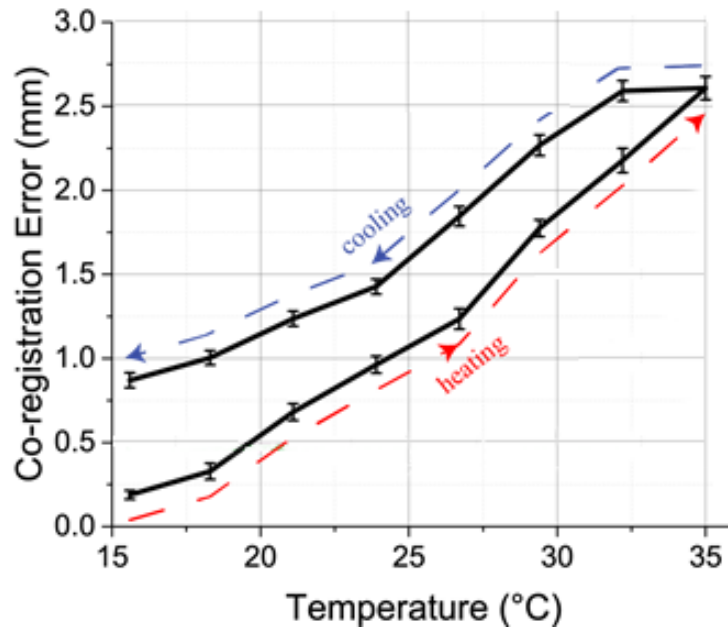


Figure 2.4 Co-registration accuracy as a function of temperature. The instrument is calibrated at the starting temperature of 15 °C and achieves subpixel co-registration accuracy. However, when the instrument is heated up to 35 °C, the co-registration error increases up to 2.5 mm. When the instrument is cooled, different co-registration errors are observed.

Figure 2.5(a) is a composite image taken with the NIRF system at 15 °C operating temperature. The green false color indicates the NIRF signal from the tumor-targeted agent. The fluorescence signal from the tumor tissue underneath the sciatic nerve is much weaker than the fluorescence signal from the surrounding tumor tissue. After thresholding the fluorescence signal, the location of the sciatic nerve is observed due to the absence of fluorescence signal (Figure 2.5(a), arrow). Since the image sensor is calibrated at 15 °C operating temperature, the NIR image (i.e., location of the tumor) is correctly co-registered on the color image (i.e., anatomical features).

Figure 2.5(b) is another set of images recorded with the NIRF sensor at 32 °C. Because of the thermally induced shift in the optical elements of the NIRF instrument, the fluorescence image is shifted with respect to the color image. The NIRF image incorrectly marks the sciatic nerve as cancerous tissue, while the cancerous tissue immediately next to the sciatic nerve has low fluorescence signal. This incorrect labelling of cancerous and nerve tissue can lead to iatrogenic damage to healthy tissue, which might not be visible to physicians, while leaving behind cancerous tissue in the patient.

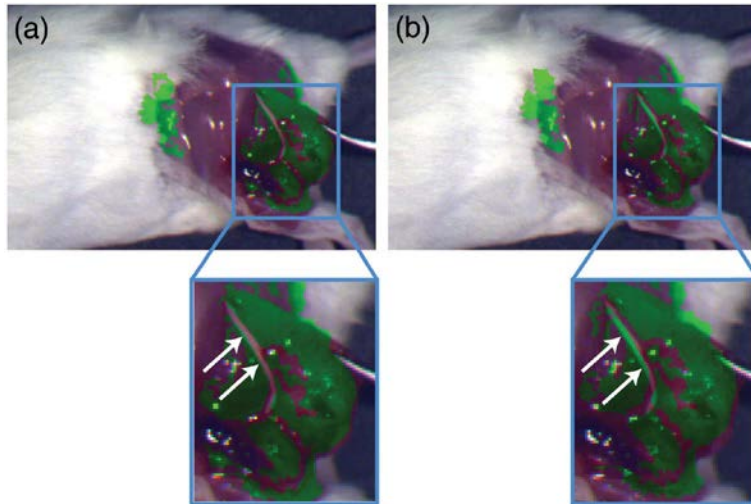


Figure 2.5 Color/ NIR composite images recorded with a beam-splitter NIRF system while the instrument is at an operating temperature of (a) 15°C and (b) 32°C.

Similar co-registration issues have been observed in color imaging technology. Prior to 1975, color cameras were constructed in the same way as today's FDA-approved instruments for NIR fluorescence image-guided surgery. They were constructed from a beam splitter, relay lenses and three individual CCD sensors with macroscopic red, green and blue filters. Temperature dependent co-registration errors were a major issue for color technology, and many papers and patents tried to solve this problem. However, with the emergence of the Bayer color pattern, which led to the monolithic integration of color filters with imaging arrays, co-registration errors were no longer an issue. Furthermore, this monolithic integration reduced the cost, power consumption and size of the image sensor, which enabled the emergence of cellphone-based cameras.

Inspired by this design methodology, various commercial image sensors have integrated pixelated color-NIR filters with imaging arrays. For example, Omnivision provides a 1 Mega-pixel image sensor constructed from polymer based pixelated spectral filters. Although, these sensors provide an interesting step toward single-chip imaging solution, the optical filters lack the transmission and optical density requirements for intra-operative procedures. Coupled with the single

integration method for all pixels in the imaging array, these sensors can achieve very poor fluorescence detection capabilities under surgical light illumination.

### **2.2.3 FDA Approved Instruments are Bulky and Interfere with the Surgical Workflow**

The large footprints of the current FDA-approved instruments are due to two factors: large imaging instruments and external monitors for displaying information. The external monitor encumbers integration of this technology in the surgical arena. First, monitors are not ideal for displaying 3-D information in surgical settings. Physicians must stop the surgery, look away from the surgical area and search for information on monitors, upsetting the surgical workflow. Second, operating rooms are very crowded, and so introducing large and costly instruments is not widely accepted. Hence, integrating compact instruments with smaller displays will be critical for wide dissemination of this technology.

# **Chapter 3: A Bio-Inspired 140 dB Dynamic Range 302 by 240 Resolution Color/Near-Infrared Logarithmic Imaging Sensor for Fluorescence-Guided Surgery**

## **3.1 Introduction**

The threat that cancer poses to human health and the necessity to improve the current imaging instruments for cancer surgery was discussed in the previous chapter. However, it is worthwhile to emphasize this because this chapter serves as one of the core parts of this dissertation. Cancer remains a major public health problem worldwide and poses a huge economic burden [1]. One in four deaths in the US is caused by cancer [2]. Although chemotherapy and radiotherapy continue to play major roles in cancer treatment, surgery remains the primary curative option for most solid cancers [28]. Image-guided surgery aims to provide critical decision-making information, such as locations of cancerous tissues, during intraoperative procedures and hence improve surgical outcome by complete removal of tumorous tissues. Specifically, near-infrared fluorescence image-guided surgery utilizes molecular markers and imaging instruments to identify tumor locations and presents this information to the surgeon without interrupting the surgical workflow. However, current state-of-the-art near-infrared (NIR) fluorescence imaging systems are bulky, costly, and lack both sensitivity under surgical light illumination and co-registration accuracy between multimodal images [29, 30]. As a result, an overwhelming majority of physicians still rely on their unaided eyes and palpation as primary sensing modalities to distinguish cancerous tissues from healthy tissues, leading to subjectivity and variable outcomes. Incomplete tumor resections are observed in many types of cancer. For example, 20-70% of breast cancers [4, 5], 28% of colon

cancers [6] and 40% of head and neck cancers [7] patients will have positive tumor margins. Secondary surgeries are expensive and have limited success rates because of the difficulty in identifying microscopic tumors or diffuse cells. Additionally, scar tissue formation from primary surgery disrupts surgical planes, making it more difficult for the physician to identify remaining tumor tissues. These studies underline the added importance of complete tumor removal during the first surgery and the need for a paradigm shift in the design of NIR fluorescence imaging systems for IGS.

Fluorescence-based intraoperative imaging techniques were first explored in the 1950s using fluorescein to identify brain tumors [8]. With recent FDA approval of the metabolic marker 5-ALA, brain cancer surgery is starting to be routinely performed under image guidance [9]. The visible-spectrum fluorescence emitted by fluorescein and 5-ALA enables physicians to assess the location of tumors under a surgical microscope. However, due to high absorption coefficients of tissues in the visible spectrum, only fluorophores near the tissue surface can be imaged, which limits diagnostic potential. For imaging more than a few millimeters below the surface of the skin, NIR fluorophores (700 to 950 nm) are used because of the low absorption coefficient of water and oxy- and deoxy-hemoglobin in this spectrum [10]. Furthermore, the low auto-fluorescence in the NIR spectrum coupled with the use of non-ionizing radiation enables high contrast to background imaging without exposing the patient and caregiver to harmful radiation [13]. Because human vision cannot detect near-infrared light, the surgeon's vision is not obscured when using NIR light. However, an imaging sensor capable of capturing both color and NIR light needs to be utilized for intraoperative procedures to localize and correctly superimpose tumor tissue on the correct anatomy of the patient.

Tumor-specific molecular markers are designed by targeting tumor antigens (or tumor markers) that are overexpressed in diseased tissues. Surgeons perform primary tumor biopsies to determine appropriate tumor biomarkers, which are then targeted with fluorescent markers to enable intraoperative tumor localization. The tumor microenvironment is very different from that of healthy tissue. For example, the metabolic rates of tumor cells are much higher than that of normal tissues, leading to higher glucose consumption rates and the formation of new vasculature necessary to deliver nutrients to the diseased tissues. Hence, a metabolic marker targeting glucose consumption can be used to highlight and localize tumor tissue. Metabolic glucose probes labeled with F, Cu and Ga are widely used for SPECT and CT imaging to localize tumor tissue [31]. For intraoperative imaging, NIR fluorescent probes targeting glucose metabolism have shown promising results for localizing tumor tissues.

Commercial IGS instruments, like FLARE [32], SPY [33], and PED [34], suffer from two major drawbacks. First, these instruments use multiple cameras with complex optics like beam splitters and optical filters to capture different wavelengths of light. These optical elements are subject to misalignment and thermal expansion. Color and NIRF information will not be correctly co-registered if the temperature changes or misalignment occurs. This will lead to the generation of false positive signals because the NIRF information no longer indicates the correct position of the tumor. Second, traditional linear CCD/CMOS image sensors with dynamic range of up to 80 dB are incapable of capturing high dynamic range (HDR) images (greater than 100 dB) in the operating room [35]. Since the photodiodes are reverse biased, the maximum signal the sensor can detect (full well capacity) is limited by the power rail and photodiode capacitance. The minimum signal is limited by the noise floor including the reset noise, electronic read-out noise, and photon shot noise. Many methods, including multiple exposures and time domain imaging, have been used

to extend the dynamic range of linear imaging systems. These methods increase the computation load of the systems or decrease the video frame rate due to slow exposure. There is a need to improve the pixel architecture to enable HDR imaging.

To address these problems, I designed an image sensor based on the compound eye of the *Morpho* butterfly. Individual ommatidium's in the compound eye have different combinations of tapetal filter stacks, which comprise stacks of alternating layers of air and cytoplasm. These tapetal filter stacks have selective spectral sensitivity across ultraviolet, visible, and NIR spectra. Furthermore, individual ommatidium responds logarithmically to light intensity, which enables high dynamic range imaging capabilities while capturing multispectral information. We have mimicked both concepts from the *Morpho* butterfly by monolithically integrating pixelated spectral filters with an array of logarithmic photodetectors. The pixel is composed of three transistors and a forward biased photodiode, which enables dynamic range imaging capabilities more than 140 dB (120dB logarithmic response). By reshaping the photon shot noise, the noise power at the photodiode become constant, leading to high SNR up to 56dB. The pixelated spectral filters record both visible spectrum and NIR images that are inherently co-registered. In this chapter, I will discuss in greater detail the image sensor operation and optoelectronic characteristics as well as present data from pre-clinical study.

## **3.2 Analysis on Logarithmic Pixel with Forward-Biased Photodiode**

The logarithmic pixel (Figure 3.1) has three transistors and an N-diffusion/P-sub forward-biased photodiode (PD). The PD is connected in parallel with an NMOS reset transistor ( $M_1$ ) so that the photodiode could be reset from output voltage to reset voltage. The open circuit voltage  $V_{oc}$  of the forward-biased PD can be derived from Shockley equation, I obtained a close form expression of



$V_{oc}$  in equation (3.1), where  $I$  is the output current of photodiode,  $I_0$  is the reverse saturation current,  $V$  is the output voltage,  $k$  is the Boltzmann's constant,  $T$  is temperature, and  $I_{ph}$  is the photocurrent. The open circuit voltage is the logarithm of the photocurrent.

$$V_{oc} = \frac{kT}{q} \ln\left(\frac{I_{ph}}{I_0} + 1\right) \quad (3.1)$$

A source follower consists of a PMOS transistor ( $M_2$ ). A current source buffers the open circuit voltage of PD with unit gain before outputting it on the column output bus. An NMOS transistor ( $M_3$ ) selects specific rows such as the pixels in the same column sharing the same output bus.

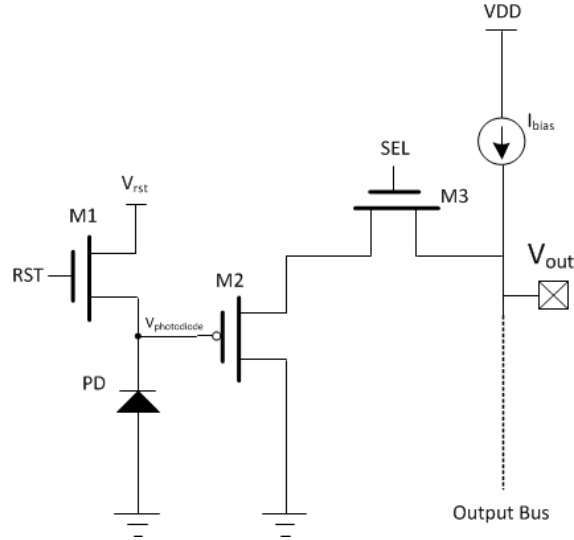


Figure 3.1 Pixel schematic. The sensor has QVGA resolution. Three registers control the reset and readout sequence. The pixel architecture is inspired by traditional active pixel sensor (APS) with a forward-biased photodiode.

The logarithmic compression increases the dynamic range. As shown in equation (3.1), the maximum detectable signal is no longer limited by the power rail and the capacitance of the photodiode. Semiconductor physics shows that the theoretical maximum open circuit voltage is  $E_g/q$ , where  $E_g$  is the bandgap of silicon and  $q$  is elementary charge [36]. In reality, the maximum open circuit voltage is affected by the recombination rate of the material.

The fixed pattern noise (FPN) and temporal noise are two major noise sources that degrade the image and reduce the detectability of the sensor, thus define the minimum detectable signal. A major drawback of traditional logarithmic sensors is their sensitivity to device parameter variations. These variations offset the pixel response. Because the traditional logarithmic sensor continues sensing without a deterministic reference level, a regular double sampling technique cannot reduce this variation and leads to high FPN. However, the deterministic reset voltage in this design can be used for differential double sampling (DDS). Before a new read-out cycle, the reset voltage, i.e., -0.3 V, is buffered by  $M_2$  and the output voltage  $V_{out1}$  is given by

$$V_{out1} = V_{rst} + |V_{t2}| \quad (3.2)$$

where  $V_{t2}$  is the threshold voltage of  $M_2$ .

After exposure time  $t$ , the output voltage  $V_{out2}$  is sampled.

$$V_{out2} = \frac{kT}{q} \ln\left(\frac{I_{ph}}{I_0} + 1\right) + |V_{t2}| \quad (3.3)$$

By subtracting  $V_{out1}$  from  $V_{out2}$ , the final output voltage of the pixel is read out. The DDS removes the FPN caused by transistor parameter, i.e., threshold voltage variations.

Generally, shot noise power spectral density is calculated as:  $\langle i^2 \rangle = 2qI$ , where  $q$  is the elementary charge and  $I$  is the current flow. The current in the photodiode consists of a current  $I_0 \exp \frac{qV}{kT}$  due to holes injected into the n-region, a current  $I_0 + I_{ph}$  due to holes generated in the n-region and being collected by the p region current. I assumed that these currents occurred independently. Here,  $I_0$  is reverse saturation current,  $V$  is the voltage between the anode and cathode,  $k$  is the Boltzmann's constant,  $T$  is temperature, and  $I_{ph}$  is the photocurrent. These relations indicated that

$\langle i^2 \rangle = 2q \left( I_0 \exp \frac{qV}{kT} + I_0 + I_{ph} \right)$ . I introduced the effective noise temperature ratio  $t \equiv \frac{\langle i^2 \rangle}{4kTG}$ .

Because the low frequency conductance is  $G = \frac{dI}{dV} = \frac{q}{kT} (I + I_0 + I_{ph})$ , I obtained  $t = 0.5[1 + (1 + \frac{I_{ph}}{I_0}) \exp(-\frac{qV}{kT})]$ . At open circuit,  $I = 0$ ,  $V = V_{oc} = \frac{KT}{q} \ln(\frac{I_0 + I_{ph}}{I_0})$ , yielded  $t = 0.5(1 + 1) = 1$ , which indicated  $\langle i^2 \rangle = 4kTG$ . Thus, the open circuit noise of a forward-biased photodiode under illumination only exhibited thermal noise. This can be modeled as a resistor. Thus, the noise equivalent circuit of the pixel with forward-biased photodiode can be modeled as a noisy current source, a noiseless conductor, a capacitor connected in parallel (Figure 3.2). This circuit has  $RC$  time constant equals to  $1/RC$ . As a result the output noise power across the whole spectrum equals to  $kT/C$  [37]. With increasing signal level and constant noise, this pixel architecture boosts the SNR as well.

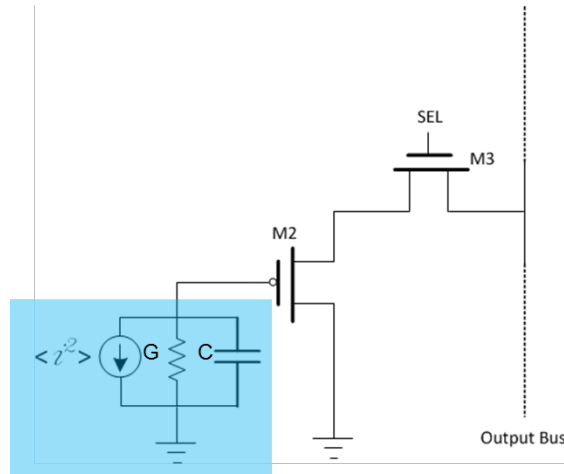


Figure 3.2 Noise equivalent circuits for the logarithmic pixel with forward-biased photodiode.

Different from pixels using reversed-biased photodiode, the exposure time for the forward-biased diode has insignificant impact. Because of the low  $RC$  constant of the forward-biased photodiode, it reaches illumination-dependent steady state in few microseconds. After stabilized, the reset noise is also automatically canceled.

### 3.3 System Overview

The sensor was implemented with an imaging array with  $302 \times 240$  pixels on a standard  $0.35\text{-}\mu\text{m}$  mixed signal CMOS process. Each pixel was  $15\text{ }\mu\text{m} \times 15\text{ }\mu\text{m}$  with a 68% fill factor. As shown in Figure 3.3, the pixel topology consisted of a  $2 \times 2$  super pixel pattern repeated across the imaging array. Red, green, blue, and NIR interference filters were integrated on top of the pixels to capture the visible and NIR spectra. Photolithography and physical vapor deposition (PVD) were used to pattern and deposit interleaved layers of dielectric with different indices of refraction, i.e.,  $\text{SiO}_2$  and  $\text{TiO}_2$ . By tuning the thickness and the number of dielectric layers, the cut-off wavelength and the shape of the passband were tuned.

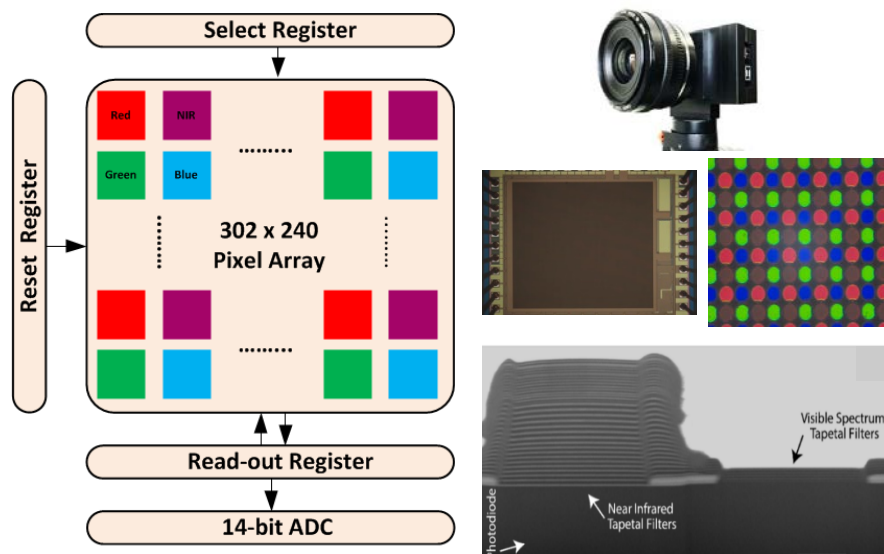


Figure 3.3 Sensor architecture (left), the micrograph of the image sensor, and the micrograph of the pixelated spectral filter array (right). The QVGA resolution pixel array is addressed by 3 register banks. The output is digitized by a 14-bit ADC.

The row reset registers, row select register and column read-out register were interfaced with individual pixels to control the transistor gates within each pixel, thereby enabling the read-out of each pixel. Off-chip reference voltage generators provided accurate reference voltages. A 14-bit analog-to-digital converter (ADC) was utilized to digitize the data. A field-programmable gate

array (FPGA) was used to transfer the raw data through USB2.0 at a frame rate of 30 fps (up to 100 fps) for real-time processing.

### 3.4 Optoelectronic Characteristic Evaluation

Before translating to fluorescence detection sensitivity, the optoelectronic characteristic of this sensor was tested. Several different optical setups were used to measure the opto-electrical characteristics. Various light sources were coupled into an integrating sphere (Newport, 819D-SF-4). The output port of the integrating sphere was aligned to an adjustable iris (Thorlabs, SM2D25) and an aspherical condensing lens (Thorlabs, ACL7560) to produce uniform and collimated illumination. A single forward-biased on-chip photodiode was first tested to verify the theoretical analysis. The voltage signal and the noise were measured by Agilent B2912A precise source/measurement unit. As shown in Figure 3.4, the voltage signal was a logarithmic function of illumination and the noise was constant.

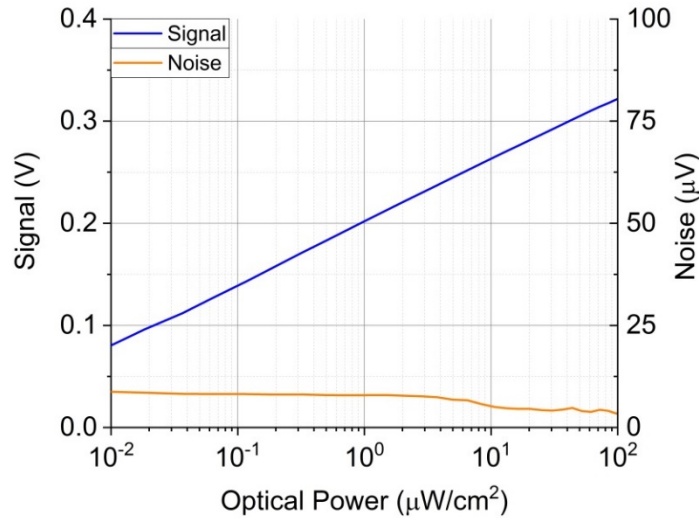


Figure 3.4 Measured signal and noise of a single on-chip photodiode

The dynamic range and photo response of the sensor were measured by coupling a broadband halogen light source into the integrating sphere. The halogen light source was fed with a constant current using a direct current (DC) power supply (Agilent Technologies, N5746A) to generate constant illumination. By tuning the intensity of the light source, the digital values for different illumination were measured. As shown in Figure 3.5, the sensor had a logarithmic response from  $10^{-6}$  mW/cm<sup>2</sup> to 1 mW/cm<sup>2</sup>, or 120 dB. The response from  $10^{-7}$  mW/cm<sup>2</sup> to  $10^{-6}$  mW/cm<sup>2</sup> was closed to linear due to the reverse saturation current. The dynamic range of this image sensor enables real-time fluorescence imaging under surgical illumination in the operating room. During the experiment, I noticed that the image sensor was not saturated at 1 mW/cm<sup>2</sup>. However, because of the limited research resources, I was not able to produce stronger illumination with uniform and stable photon flux. The major trade-off is the decreasing sensitivity of the forward biased photodiode.

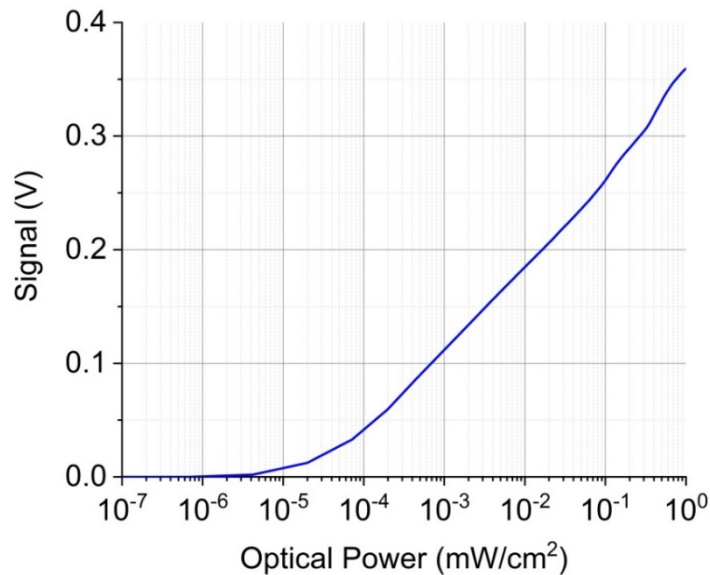


Figure 3.5 Logarithmic photo-response of the sensor.

As shown in Figure 3.6, the sensitivity is inverse-proportional to the optical power under medium to high illumination because the logarithmic photo response “compress” the output data. As the sensitivity drops, the sensor needs more photons to generate higher digital value. Eventually, the sensitivity drops below the noise floor of the ADC and the image sensor reaches its full scale. However, compared with a state-of-the-art linear 4-transistor (4T) CMOS camera [38], this sensor still has up to 25 time higher sensitivity under low to medium illumination. This boosts the detectability of weak fluorescence. Other factors, like the swing of the source follower, the carrier recombination inside the photodiode, also limits the dynamic range.

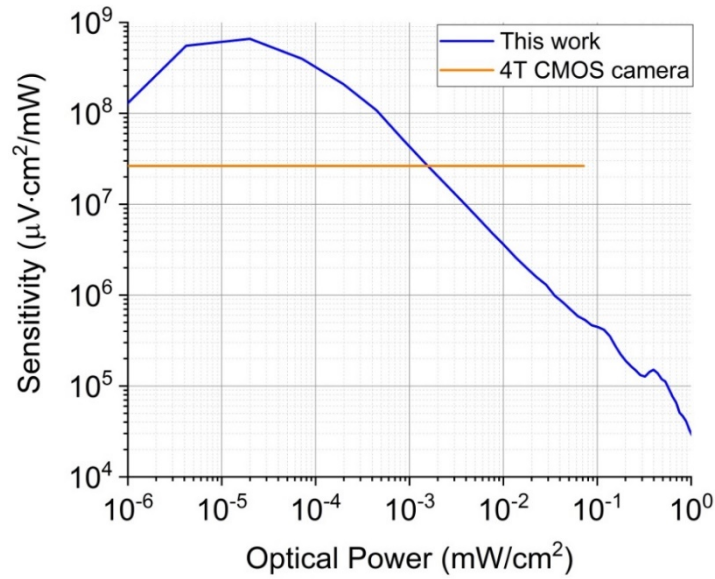


Figure 3.6 The sensitivity of the image sensor. It is inverse-proportional to the optical power of the illumination. As shown in Figure 3.7, the measured temporal noise from this sensor was constant. This conclusion is generally accepted by the electrical circuit community since the 1970s [39]. Another explanation is that the noise is also “compressed” by the logarithmic response. Although the photon shot noise increases with the photon flux, the logarithmic photo response performs a non-linear transformation and suppresses the noise. Adding the reset noise and readout noise, the

overall noise becomes constant. Both explanations reach the same conclusion. Compared with a state-of-the-art linear 4-transistor (4T) CMOS camera [38] which has dominant photon shot noise, the constant readout noise of this sensor leads to more than 56 dB signal-to-noise ratio (SNR) at full scale (Figure 3.8). The SNR of this sensor is up to 180 times greater (or 25 dB more) than the SNR of the state-of-the-art 4T CMOS camera.

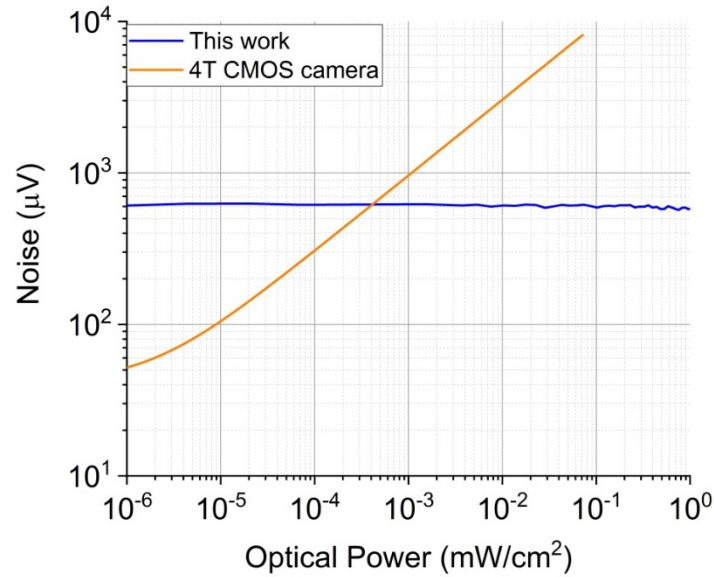


Figure 3.7 Temporal noise of the sensor. The forward-biased diode's noise can be modeled by a noise-less resistor with a noise current source in parallel.



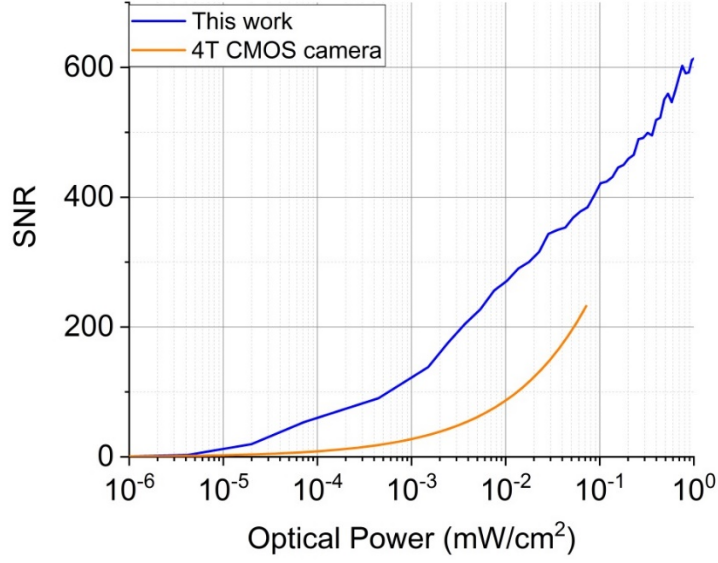


Figure 3.8 Signal to noise ratio at different signal levels. 56dB SNR is achieved.

The spatial uniformity or fixed pattern noise (FPN) of the red, green, blue and NIR channels was below 0.6% as a function of light intensity (Figure 3.9). The spatial variations primarily came from two sources: 1) the device parameter variation in the pixels, such as the different threshold voltages of the source followers, the non-uniform biasing current for each column and the non-uniformity of the reverse saturation current of each photodiode, i.e., dark current non-uniformity (DCNU) (Figure 3.10); and 2) the non-uniform thickness of the dielectric layers of each interference filter, which introduces photo-response non-uniformity (PSNU). Whereas the DDS removed most of the non-uniformity caused by 1), further improvement of the nanofabrication process could be possible to reduce 2).

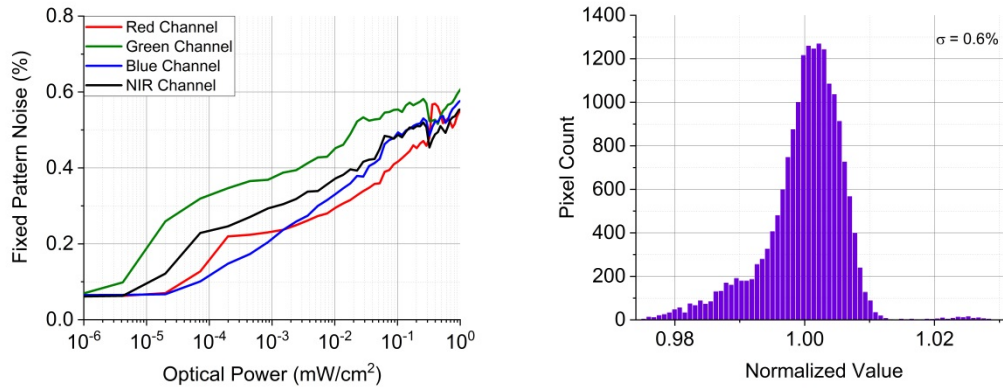


Figure 3.9 FPN of the sensor (left) and the histogram of the NIR channel at 1mW/cm<sup>2</sup> (right).

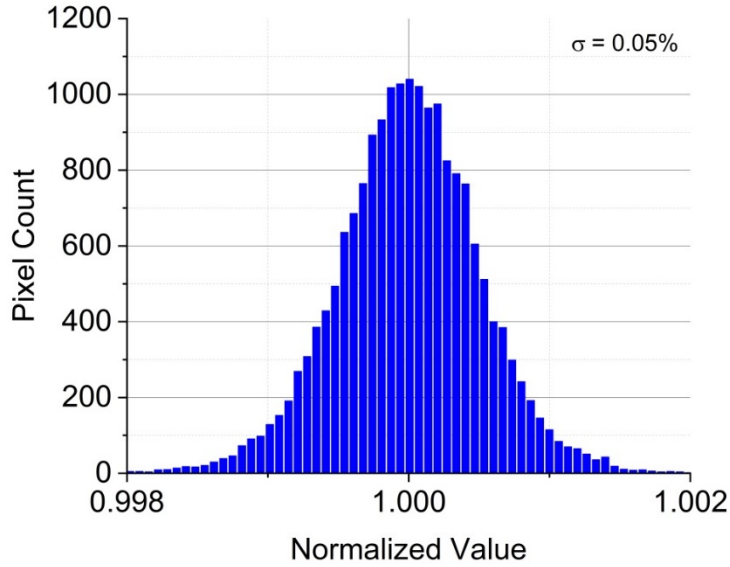


Figure 3.10 Histogram of the NIR channel at dark. The DCNU is 0.05%. The DDS removes most of the non-uniformity.

The quantum efficiency (QE) was measured by coupling the output of a monochromator (Princeton Instrument, Acton SP 2150) into the integrating sphere. The photon flux was measured by a calibrated photodiode (Thorlabs, S130C) driven by a power meter (Thorlabs, PM100D). The measured QE is shown in Figure 3.11. The peak QEs of the red, green, blue and NIR channels were between 3 and 9% across a 400 nm to 1000 nm wavelength range. The low QE is due to the

non-optimized fabrication process and the destruction of micro-lens array while integrating the pixelated filter.

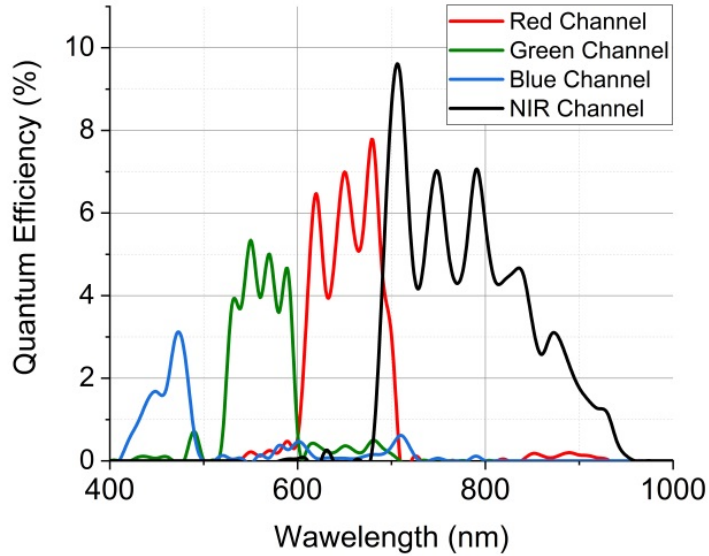


Figure 3.11 Quantum efficiency of the red, green, blue and NIR channels.

### 3.5 Pre-clinical Evaluations and Animal Study

Figure 3.12 demonstrates the high dynamic range (HDR) capability of this sensor. The LED panel with visible short-pass filter was directly pointed at the sensor. A vial of QDot 800 was placed in front of the LED panel and excited by a 785-nm laser to produce fluorescence emissions at 800 nm. The scene had approximately 100dB DR. A commercial digital single-lens reflex camera with the same lens ( $f = 35$  mm, aperture  $f/2.8$ , exposure time  $1/30$  s) was used for comparison. Compared with the low dynamic range (LDR) commercial imaging sensor (Figure 3.12(a)), this sensor captures the entire DR without losing details in the color image, such as the outline of the vial (Figure 3.12(b)) and captured the NIR fluorescence (Figure 3.12(c)). The color and NIR images are co-registered thus can be superimposed onto each other (Figure 3.12(d)).

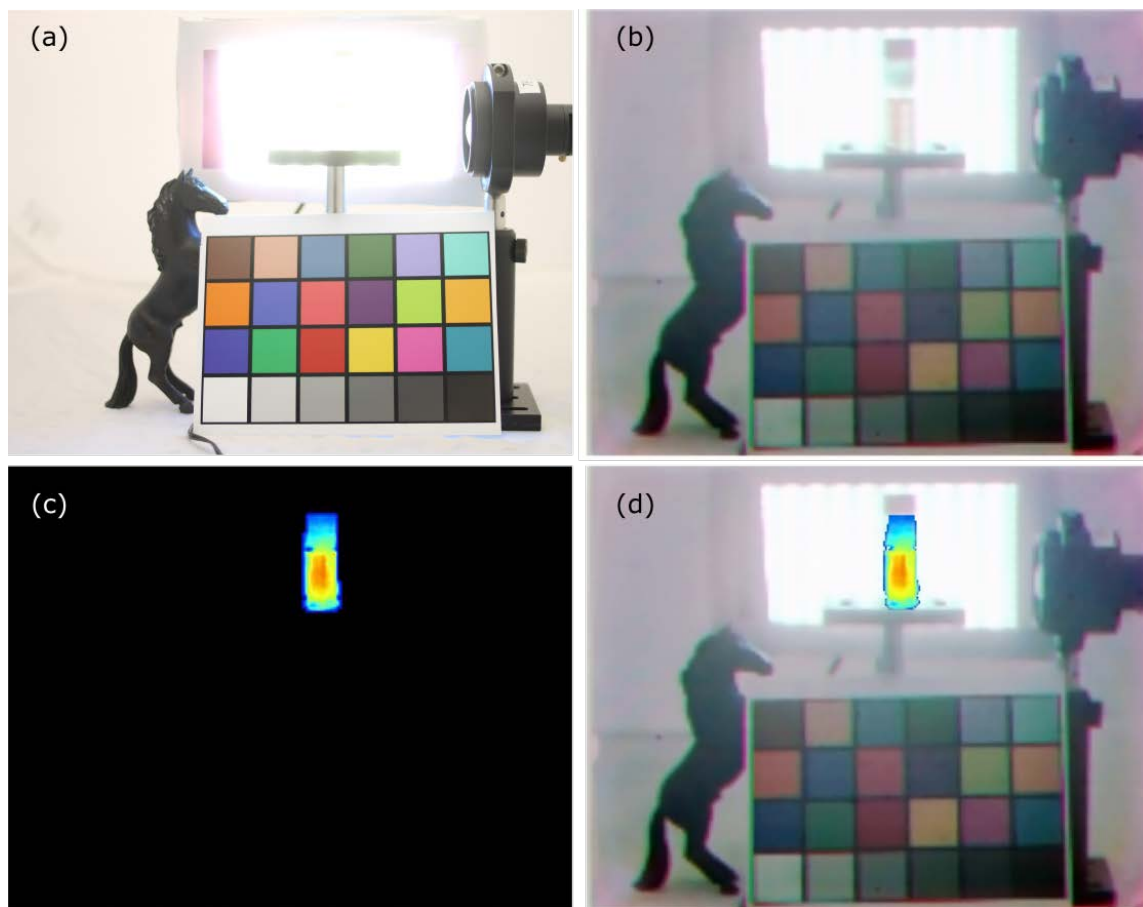


Figure 3.12 Comparison between the LDR color sensor (a) and this HDR color/NIR sensor (b,c,d). The commercial LDR sensor is not able to capture the details in the LED panel nor the vial in front of it (a). However, this HDR sensor can capture both HDR color image (b) and NIR image (c). The color and NIR images can be seamlessly superimposed (d).

The fluorescence sensitivity of this sensor was tested by imaging 9 different ICG concentrations in plastic vials under surgical light illumination and excited with a laser light excitation power of  $20 \text{ mW/cm}^2$  at 785 nm. For each concentration, three different vials were tested and a control vial with deionized water imaged at a frame rate of 30 fps. A  $10 \times 10$  region of interest within each vial was selected to avoid edge artifacts, such as specular reflection of the plastic itself. An average intensity value and standard deviation of the NIR pixels were computed within the region of interest. The detection threshold was determined as the average NIR signal plus three standard deviations of the control vial. Figure 3.13 shows that this sensor can detect as low as 40 nM ICG.

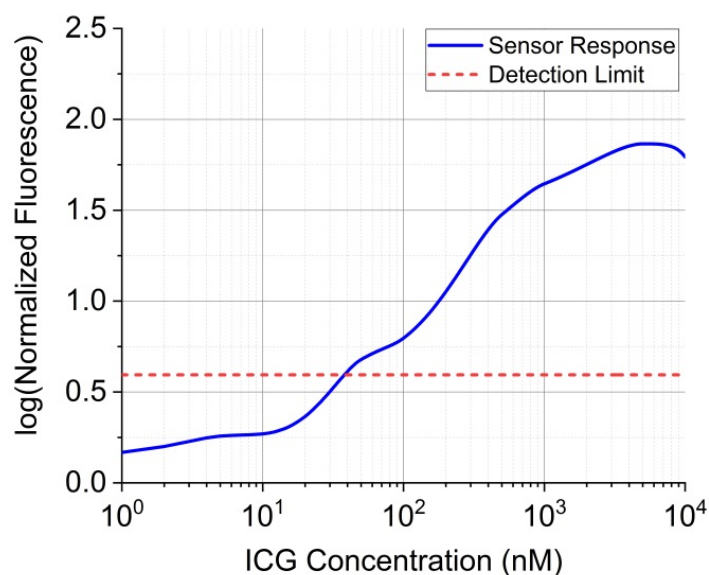


Figure 3.13 Fluorescence detection limits. This sensor can detect as low as 40 nM ICG at 20 mW/cm<sup>2</sup> NIR excitation.

We used J:NU mice with tumors to demonstrate the fluorescence detection capability of this sensor. Animals were obtained from The Jackson Laboratory, Bar Harbor, ME. A 2-month-old male J:NU nude mouse with PC3 cancer was imaged 24 hours post-injection of 20 nmol IRDye 800 CW, i.e., an EGFR tumor-targeted NIR fluorescence contrast agent. The imaging setup consisted of the custom sensor with a Canon EF lens ( $f = 35$  mm, aperture  $f/2.8$ ), a laptop (Lenovo Thinkpad W530), a 780-nm laser (B&W TEK Inc., BWF2-780-0.8) and a visible-light LED panel (Genaray, LED-7100T). A 780-nm band-stop filter (Semrock, NF03-785E-25) was placed in front of the sensor to block fluorescence excitation. The laser was coupled to the optics by an optical fiber. The laser optics consisted of a bandpass filter at 780 nm (Semrock, LL01-780-12.5), an aspheric condenser lens (Thorlabs, ACL25416U-B), and a diffuser (Edmund Optics, 47-994) to create a 10-cm uniform circular illumination pattern with 5-20 mW/cm<sup>2</sup> excitation power. The LED panel produced 5 kLux of visible light at the surface of the imaging with a light temperature of 5,000 K. A visible short-pass filter (3M, Cool Mirror Film 330) was placed on top of the LED

panel to suppress any leakage of wavelengths above 700 nm that would deteriorate the fluorescence signal acquired by the sensor. Figure 3.14 shows the color image, the NIR fluorescence image in jet color and the superimposed image. The sensor accurately highlighted the position of the tumor. The sensor achieved ~95% sensitivity and ~94% specificity.

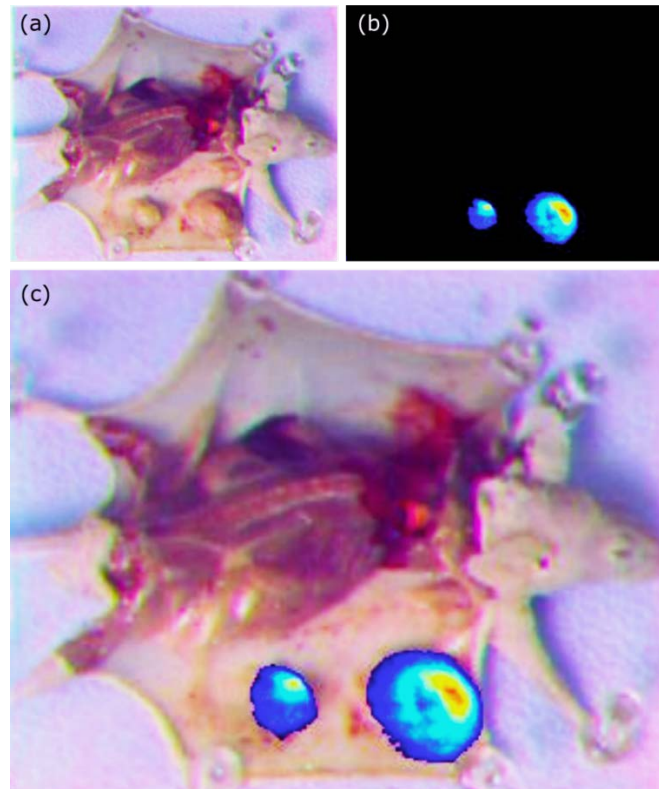


Figure 3.14 (a) Color image, (b) NIR fluorescence image and (c) superimposed image of a mouse with cancer. Tumor-targeted contrast agent was injected 24 hours before imaging.

### 3.6 Conclusion and Discussion

In this chapter, I presented an HDR color/near-infrared logarithmic imaging sensor using forward-biased photodiode for fluorescence-guided surgery. I described the design method in detail and experimentally measured the optoelectronic characteristic and the fluorescence sensitivity of this sensor. With the pixelated multispectral filter array, the imaging system provides color and co-registered NIR information to the end user. Compared with the state-of-the-art linear CMOS image

sensors (Table 3.1), this sensor has equivalent thermal noise as dominant noise. The exposure time does not affect the output significantly, thus a shutter is not needed. It has higher DR, SNR, sensitivity and frame rate.

Table 3.1 Design summary and comparison with the state-of-the-art linear CMOS sensors

Description	This work	[38]	[40]
Pixel size	<b>15 <math>\mu\text{m} \times 15 \mu\text{m}</math></b>	6.5 $\mu\text{m} \times 6.5\mu\text{m}$	7.8 $\mu\text{m} \times 7.8\mu\text{m}$
Dominant noise	<b>equivalent thermal noise</b>	photon shot noise	photon shot noise
Shutter type	<b>No shutter</b>	Rolling shutter	Rolling shutter
Dynamic range	<b>140dB</b>	95dB	62dB
Maximum SNR	<b>56dB</b>	45dB	48dB
Full well capacity	<b>Not applicable</b>	54,000 electrons	72,000 electrons
Sensitivity	<b>up to <math>10^8 \mu\text{V}/(\text{mW}/\text{cm}^2)</math></b>	$10^7 \mu\text{V}/(\text{mW}/\text{cm}^2)$	N/A
Resolution	<b>302<math>\times</math>240</b>	2048 $\times$ 2048	1280 $\times$ 720
Maximum FPS	<b>100</b>	74	40

This sensor also solves the common problems of traditional logarithmic CMOS image sensors: high FPN, high temporal noise and low SNR. The comparison is shown in Table 3.2.

Table 3.2 Design summary and comparison with the state-of-the-art logarithmic sensors

Description	This work	[41]	[42]	[43]
CMOS technology	<b>0.35 <math>\mu\text{m}</math></b>	0.5 $\mu\text{m}$	0.18 $\mu\text{m}$	0.25 $\mu\text{m}$
Pixel size	<b>15 <math>\mu\text{m} \times 15 \mu\text{m}</math></b>	7.5 $\mu\text{m} \times 10 \mu\text{m}$	5.6 $\mu\text{m} \times 5.6 \mu\text{m}$	10 $\mu\text{m} \times 10 \mu\text{m}$
Fill factor	<b>68%</b>	Near 100%	33%	43%
Dynamic range	<b>140 dB</b>	120 dB	143 dB	120 dB
Imaging array size	<b>302 <math>\times</math> 240</b>	525 $\times$ 525	352 $\times$ 288	N/A
Temporal noise	<b>625 <math>\mu\text{V}</math></b>	2280 $\mu\text{V}$	950 $\mu\text{V}$	N/A
Fixed pattern noise	<b>0.6%</b>	2.5%	2%	2.46%
Signal-to-noise ratio	<b>56 dB at full scale</b>	N/A	48.1dB	N/A
Quantum efficiency	<b>3%-9%*</b>	N/A	N/A	N/A
Fluorescence detection	<b>40 nM ICG**</b>	N/A	N/A	N/A

\* Blue 3%, Green 5%, Red 8%, NIR 9%, \*\* under 20mW/cm<sup>2</sup> excitation

We also demonstrated the application using an animal model. The imaging system provides color and co-registered NIR information to users. Because of its compact size, inherent accurate co-

registration and excellent dynamic range, this sensor can assist physicians under surgical illumination without impacting the normal surgical workflow.

Because the photodiode voltage reaches illumination-dependent steady state regardless of the initial value, the reset transistor could be removed in future design (Figure 3.15). It will reduce the number of transistors to 2 and number of metal lines to 4. In this way the photosensitive area can be enlarged. Therefore, the capacitance of the photodiode can be increased, and the equivalent thermal noise can be reduced. Without having DDS, other FPN removal techniques need to be incorporated. Other future work includes increasing the imaging array size, reducing pixel pitch, and integrating the ADC and peripheral circuits on a chip.

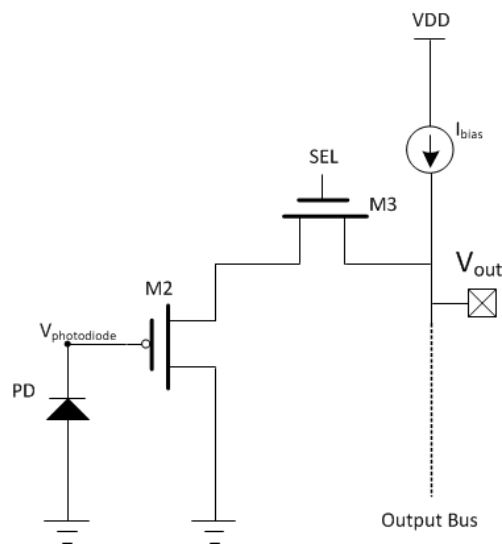


Figure 3.15 Future 2-transistor pixel schematic.



# **Chapter 4: A 120 dB QVGA Resolution** **Time-Based Pulse-Width-Modulation** **Address-Event Representation Color-** **Infrared Imaging System for Fluorescence-** **Guided Surgery**

## **4.1 Introduction**

Surgery is the primary curative option for patients with cancer. Surgeons rely on two main sensing modalities during intraoperative procedure, namely touch and visual inspection to differentiate healthy from diseased tissue. However, the low visual contrast between healthy tissue and tumor's proliferating edges results in incomplete resection of all types of tumors. For example, 20-70% of patients with breast cancer [4, 5], 28% with colon cancer [6] and 40% with head and neck cancer [7] will have positive tumor margins and will require either secondary surgeries and chemotherapy. However, secondary surgeries not only are expensive but also have limited success because of the difficulty in seeing microscopic tumors or diffuse cells. Additionally, scar tissue formation perturbs the surgical planes, making it more difficult for the surgeon to identify the remaining tumor tissue. These studies underscore the importance of complete tumor removal during the first surgery and the need for a paradigm shift in the design of imaging systems for image-guided surgery (IGS).

Fluorescence based image guided surgery in the NIR spectrum has gained a lot of traction in the last decade due to proliferation of FDA-approved instruments and novel tumor targeted molecular probes. The low absorption coefficient of water, oxy- and deoxy-hemoglobin combined with low auto-fluorescence in the NIR spectrum, enables imaging tumor targeted molecular markers from

several millimeters deep in the tissue. There are currently only two FDA-approved, non-specific molecular markers with NIR fluorescence (NIRF): indocyanine green (ICG) and methylene blue [11]. Both markers are used either for mapping the primary draining lymphatic nodes near the tumor site, known as sentinel lymph nodes (SLNs), or for assessing blood perfusion in tissue [14]. There are many tumor-targeted molecular probes being developed and tested in variety of clinical trials. Although none of them are FDA approved, some of the molecular probes have successfully completed phase 2 and phase 3 clinical trials.

Variety of IGS instruments have been approved by the FDA during the last decade and have been typically adopted in large clinical centers. However, most FDA approved instrument suffer from two major drawbacks: temperature dependent co-registration error and dynamic range of less than 80 dB which limits its usability during intraoperative procedures. The limited dynamic range of the current FDA approved instrument, require surgeons to stop the surgery, turn off the surgical light, use image guidance to identify the location of the cancerous tissue, and continue the surgery either in dimmed light conditions or without image guidance under regular surgical illumination. Although these instruments provide invaluable information to the surgeons, their integration in the operating room is far from ideal.

To address these problems, in this chapter I will describe our efforts to develop a bio-inspired, multispectral imaging system with high dynamic range imaging capabilities. The design of the imaging system is inspired by the visual system of the *Morpho* butterfly in two respects: (1) pixelated multispectral filters comprised of layers of stacked dielectrics, and (2) the image sensor utilizes an address-event representation (AER) read-out scheme which is similar to an integrate-and-fire neuron. To boost the dynamic range, the sensor uses time-domain pulse-width-modulation (PWM) technology. The pixelated spectral filters were integrated in the cleanroom facilities at

University of Illinois at Urbana-Champaign. The complete system was used together with an affibody molecular marker targeting epidermal growth factor receptor which is overexpressed in cancerous cells. The imaging system with affibody NIR molecular marker was able to detect orthotopic implanted prostate cancer cells with sensitivity and specificity of ~85% and 87%, respectively. The small foot print of the imaging system, coupled with the high dynamic range, and low cost can enable value-based health care in both resource-limited and resource-rich hospitals.

## **4.2 Time-Based PWM AER Color-Infrared Image Sensor**

The DR of an image sensor is defined by the ratio of the maximum output signal and the minimum detectible signal. A traditional active pixel sensor (APS) converts different illuminances into different voltages as shown in Figure 4.1 (a), i.e., the darker the image is, the higher the reported voltage after a fixed integration time. The DR is limited by the power rail, full well capacity, reset noise, readout noise and fabrication process. The typical DR of a traditional APS is limited to 60–80 dB.

To overcome the DR limit of APS, several approaches have incorporated piecewise linear response pixels [44], logarithmic pixels [41] and linear-log pixels [42]. Another design is based on measuring the time required for the photodiode to discharge to a given voltage. This technique is known as time-based pulse width modulation (PWM) imaging. This technique allows for each pixel to have an individual integration time. Because the brightness of the image is extracted from the time domain instead of the voltage domain, the DR is not limited by the power rail and full well capacity. As shown in Figure 4.1 (b), the DR is only limited by the shortest integration time when the maximum photocurrent is generated and the longest integration time when only dark

current discharges the photodiode. The time domain PWM sensors have been reported to achieve DRs up to 140 dB [35].

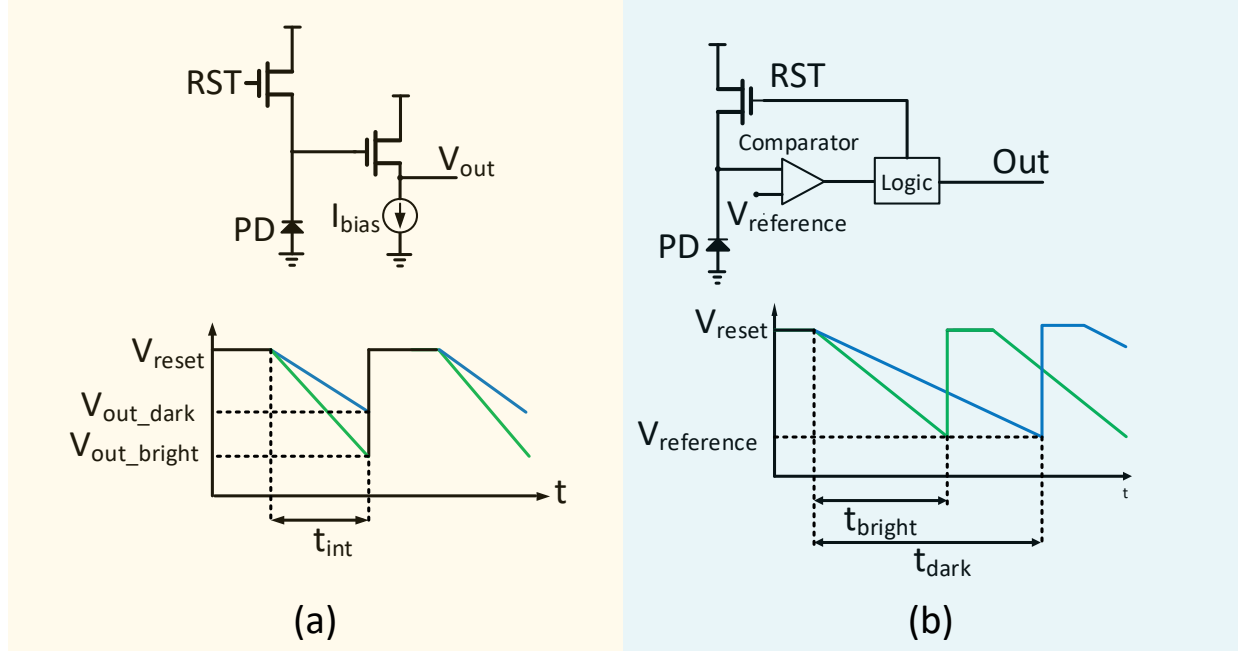


Figure 4.1 (a) Traditional APS pixels. All pixels are exposed to light for the same amount of time. The dark pixels have a smaller voltage drop, while the bright pixels have a larger voltage drop. (b) Time domain PWM sensor. All pixels are discharged to the same voltage level. It takes the dark pixels a longer time to reach this voltage level, while it takes a shorter time for the bright pixels.

#### 4.2.1 Sensor Architecture and AER Readout Scheme

The sensor was designed with an imaging array of  $304 \times 240$  pixels, implemented in a standard 0.18- $\mu\text{m}$  mixed signal CMOS process. The pixel array covered 77% of the total die area of 9.9 mm by 8.2 mm. As shown in Figure 4.2, the pixel topology consists of a 2 by 2 super pixel pattern repeated across the imaging array. Red, green, blue, and NIR interference filters are integrated on top of the pixels to capture visible and NIR spectra. Physical vapor deposition (PVD) is used to deposit multiple dielectric layers with different indices of refraction, i.e.,  $\text{SiO}_2$  and  $\text{TiO}_2$ . By tuning the thickness and dielectric layer numbers, I tuned the cut-off frequency and the passband shape of the filters. The imaging array is controlled by on-chip X/Y reset control registers, address

encoders and address-event-representation (AER) arbiters for asynchronous data transfer [45]. An on-chip reference voltage generator provides accurate reference voltages.

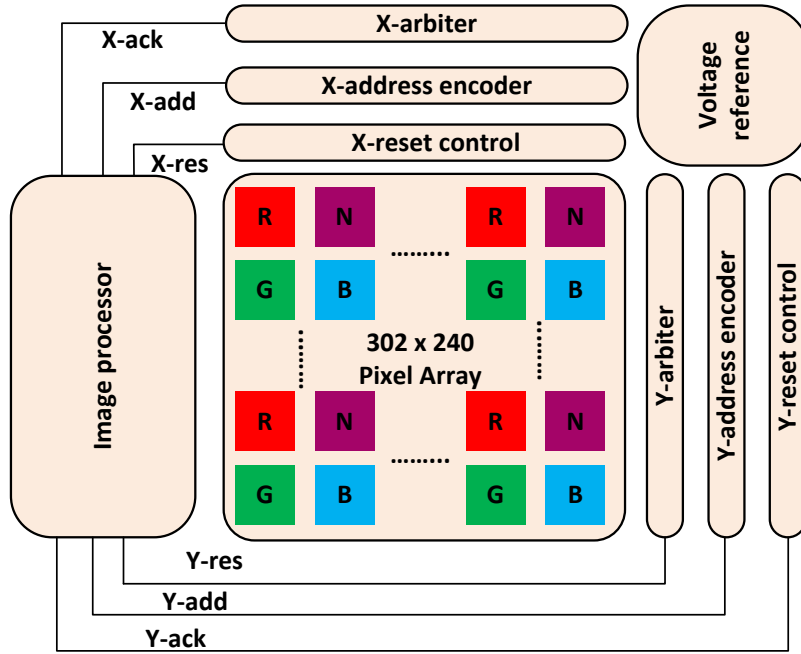


Figure 4.2 Sensor architecture and micrograph.

The pixel values are read out asynchronously. Compared with conventional image sensors, which acquire the voltage of all photodiodes after a pre-determined integration time and report values by scanning the whole imaging array, this sensor reports the timestamp and address of a pixel only after an event is generated. An event includes whether a pixel is reset or discharged to the reference voltage level. The X/Y address encoder represents the 9-bit X address and 8-bit Y address for that pixel. The 4-phase AER handshaking circuits communicates with the X/Y arbiters. Because the request and acknowledgement signals of the pixels are shared across each row and column, events are transmitted on a “first-come-first-serve” basis. When one pixel finishes integration, a “Y-Request” is first pulled to generate an event. As soon as the Y address encoder generates the address and the “Y-Acknowledge” signal is received, the pixel pulls down the “X Request” and the X address encoder generates the X address. Once the external image processor receives the



The signal-to-noise ratio (SNR) of the sensor is reduced by reset noise, readout noise, dark current shot noise and photon shot noise. The readout noise, dark current shot noise and photon shot noise are determined by the circuit and fabrication process. However, the reset noise is largely reduced by CDS. It eliminates the reset noise by subtracting two timestamps when  $V_{int}$  crossed two different voltages. The dark current non-uniformity can also be suppressed using CDS, leading to low fixed pattern noise (FPN).

## 4.3 System Characterization

The electrical characteristic of this sensor is comprehensively evaluated in [35]. This sensor has been reported to achieve >50 dB uniform SNR from 10 to 10,000 lux due to the complete discharge of photodiodes. This is sufficient to realize 8-bit color resolution. The integration time is less than 10 ms from 10 to 10,000 lux for a 500-mV integration swing, enabling video rate data streaming. The following sections focus on evaluating the optical performance and fluorescence detection of the proposed imaging system.

### 4.3.1 Spectral Response

To capture both color and NIR fluorescence images, the imaging system has an array of pixelated interference filters to create 4 different channels and efficiently convert different photon wavelengths to a photocurrent. The blue, green, red and NIR filters roughly have passbands from 400 – 500 nm, 500 – 580 nm, 570 – 700 nm and 700 – 1000 nm, respectively. The quantum efficiency (QE) for each channel was evaluated using a monochromator (Princeton Instruments Acton SP2150). A DC power supply (Agilent N5746A) was used to provide a constant power supply to the illumination bulb of the monochromator. An optical fiber and an aspheric condensing lens (Thorlabs ACL 7560) were used to expand the beam while maintaining the uniformity of the monochromator output. The measured QE is plotted in Figure 4.4. The color channels have 3 –

17% QE, whereas the NIR channel has 7% QE above 800 nm. To suppress the 780 nm NIR excitation, I used a 780-nm notch filter (Semrock, NF03-785E-25) with optical density 6 in front of the imaging system.

The QE of the blue channel is low because the fabrication technology is not optimized for imaging. The shallow p-n junction causes low photon absorption. The high-density surface defects introduce recombination center and reduces the net generation rate of electron-hole pairs. Furthermore, the micro-lens array which focuses the beams onto the photodiodes is not available in this fabrication process. By optimizing the p-n junction depth and adding a micro-lens array, the QE could be increased.

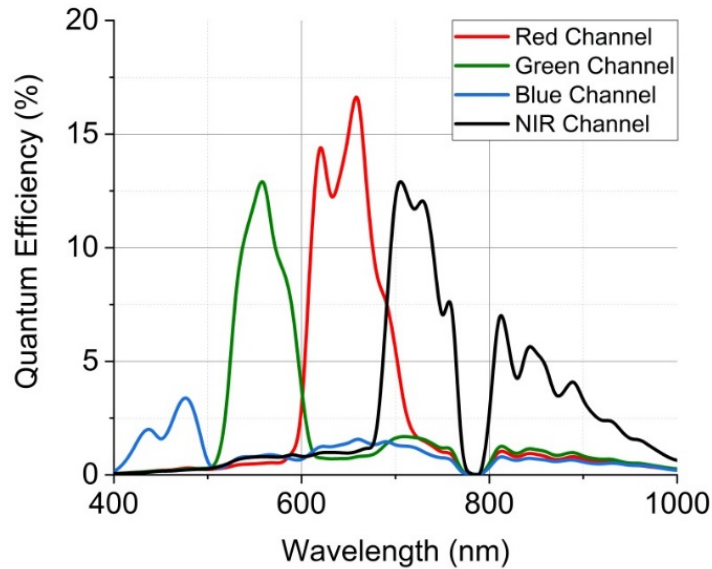


Figure 4.4 Quantum efficiency of the imaging system. Blue, green, red, and NIR pixels have ~3%, 13%, 17% and 13% peak QE. Note that I added a 780-nm notch filter to block the NIR laser excitation, which leads to the QE around 780 nm being negligible.



### 4.3.2 Photo Response Non-Uniformity

Although CDS largely eliminates dark current non-uniformity, photo response non-uniformity caused by fabrication variations across the silicon wafer, especially thickness variation and the misalignment of the pixelated interference filter, still exists and contributed toward the FPN. To evaluate the FPN, a broad-band tungsten light source (Thorlabs, OSL1) and an integrating sphere (Newport 819D-SF-4) were used to generate uniform illumination. The FPN is plotted against the reference voltage in Figure 4.5. The FPN is approximately 3% for the red and green channels and 7% for the blue and NIR channels.

Because the photodiode has a linear response, I applied a flat field calibration using linear regression. I used 6 sets of training data and mapped the gain and offset of each pixel to the average ones. This reduced the FPN of all channels to less than 2%.

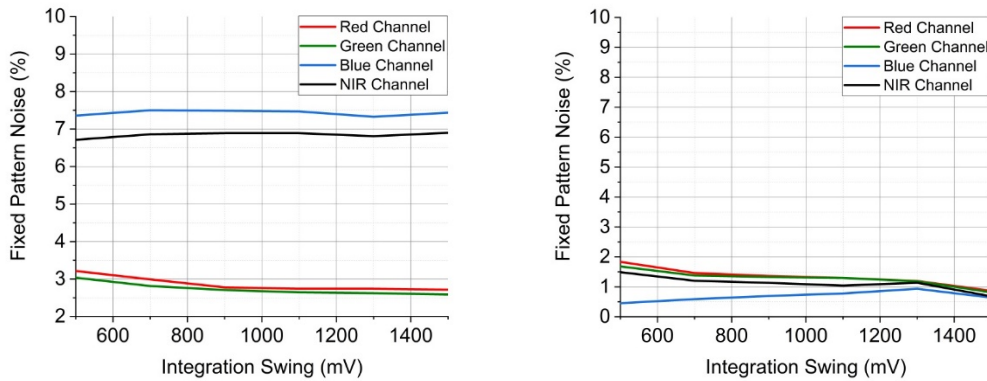


Figure 4.5 FPN of the imaging system. (left) Before calibration, the FPN is between 3% and 7.5%, and (right) after calibration, the FPN drops down to less than 2%.

An important feature of this imaging system is that the signal to noise ratio (SNR) is approximately a constant number for each pixel regardless of the photon flux. Because the photodiodes are always completely discharged, photon shot noise is the dominant noise source: the SNR only depends on the number of photon-generated electrons. Once the potential well depth is fixed, the SNR is approximately a constant number within 6 decades of illumination range (Figure 4.6).

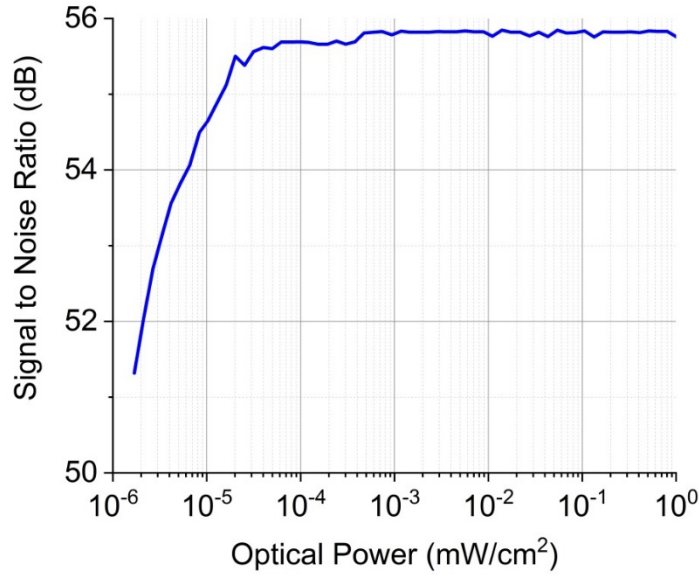


Figure 4.6 Signal to noise ratio of the imaging system. The SNR maintains 56 dB for 6 decades of different illumination. It drops at low optical power due to the readout noise.

### 4.3.3 Fluorescence Detectability

The fluorescence detectability was evaluated using ICG water solution at different concentrations. Two sets of ICG solutions were tested, and the average response was reported to minimize the error caused by weighing and dilution. The ICG solution was excited by a 780-nm laser (BWF2-780-0.8) filtered by a laser clean-up filter (Semrock, LL01-780-12.5) at 20 mW/cm<sup>2</sup> power. An aspheric condenser lens (Thorlabs, ACL25416U-B) and a diffuser (Edmund Optics, 47-994) were placed in front of the filter to create a uniform illumination pattern. The modified LED light source was turned on during the experiment to provide 40 kLux visible illumination. Background subtraction [46] was applied to remove auto-fluorescence and other background noise. Figure 4.6 shows the normalized photo response versus ICG concentration. I used distilled water as a reference sample. The detection limit was defined by (2) [47]:

$$I_{limit} = I_0 + 3\sigma_0 \quad (2)$$

where  $I_{limit}$  is the photo response of the detection limit,  $I_0$  is the photo response of the reference sample, and  $\sigma_0$  is the standard deviation of the reference sample photo response. The horizontal dashed line indicates  $I_0+3\sigma_0$ , and the solid line indicates the photo response at different concentrations. Figure 4.7 shows that this imaging system can detect approximately 50 nM of ICG under surgical illumination.

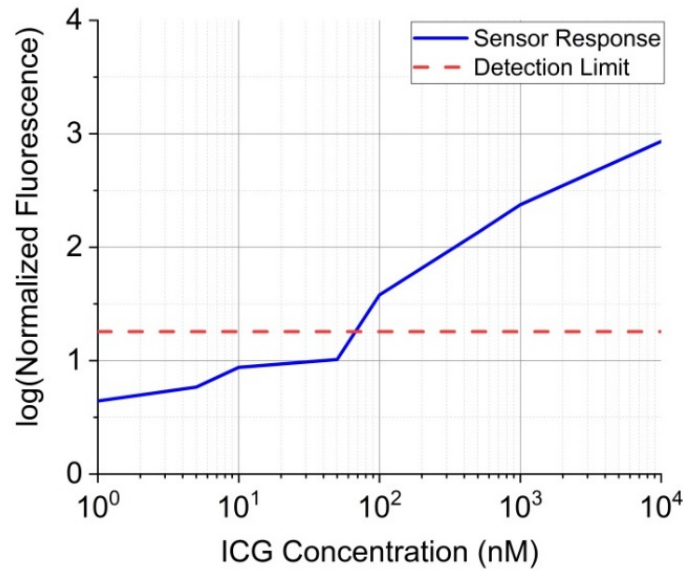


Figure 4.7 Fluorescence detectability. This imaging system can detect as low as ~50 nM of ICG at 20 mW/cm<sup>2</sup> NIR excitation.

## 4.4 Pre-Clinical Studies

Quantum dots (Qdot) 800 has sufficient absorption at 780 nm and emission at 800 nm [48]. I filled a glass vial with approximately 5 mL of QDot 800 and verified the performance of this imaging system under surgical illumination by recording the color image, NIR image and the superimposed image, as shown in Figure 4.8. The NIR signal is clearly emitted from QDot800. The NIR image is correctly superimposed over the color image without any co-registration error.

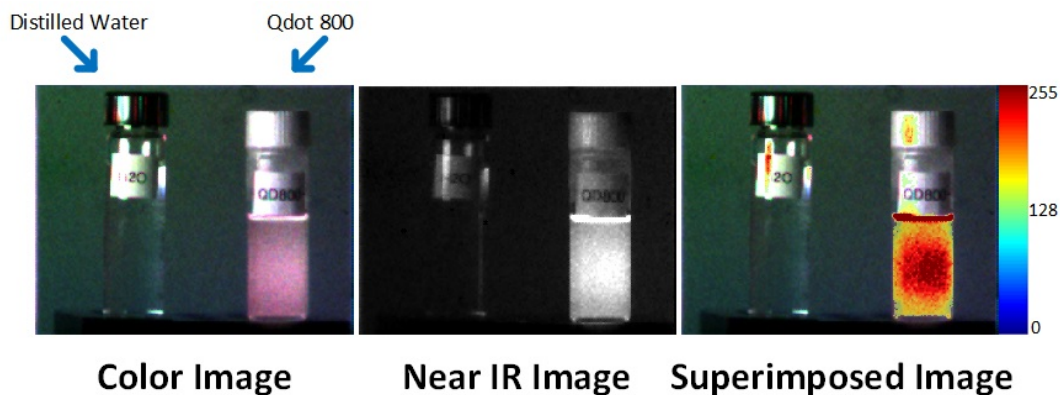


Figure 4.8 Image of the glass vial containing QDot800. A vial of water is placed next to it for comparison. The NIR image is correctly superimposed on the vial of Qdot800.

## 4.5 Imaging Tumors Under Surgical Light Illumination

I used this imaging system to identify orthotopic prostate cancer in a murine model (n=3). The animal was injected with IR800CW-EGFR targeted marker. Because this imaging system has high co-registration accuracy and NIRF sensitivity, the physician could easily locate the tumors, resect them, and ensure that the tumor margins were negative (Figure 4.9). When I compared results obtained with my bio-inspired imaging system against histology results, I found that my imaging system together with the tumor-targeted probe had a sensitivity of 85%, a specificity of 87%.

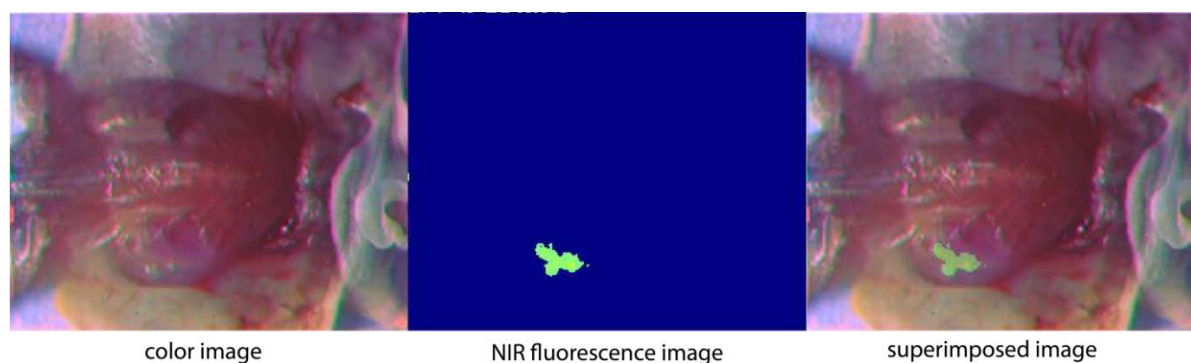


Figure 4.9 Color image, NIR fluorescence image and superimposed image of a mouse with ICG injected into the kidney.

## 4.6 Conclusions

Fluorescence-guided surgery gives the surgeon anatomical information of healthy tissue and the intraoperative position of tumor tissue. Current technology is limited by co-registration accuracy and the DR of state of the art image sensors. Most state-of-the-art instruments are not capable of capturing weak fluorescence signals under surgical light conditions. I developed a time-based PWM AER color/NIR imaging system. This imaging system solved the co-registration problem by monolithic integration of pixelated spectral filters with bio-inspired image sensor. Due to the time-based PWM imaging technique, the DR of the sensor can be extended up to 120 dB. I evaluated the performance of this imaging system and demonstrated its effectiveness using fluorescence molecular markers in prostate cancer animal models.

# **Chapter 5: A Miniature Handheld Multi-Exposure Color/Near-Infrared Fluorescence Camera Prototype for Image-Guided Surgery**

## **5.1 Introduction**

The goal of image-guided surgery (IGS) is to provide time critical information to the physician about the locations of tumor and healthy tissue during intraoperative procedures. Various techniques have been developed for IGS, including x-ray imaging, two-photon imaging, fluorescence and others. Fluorescence imaging is of particular interest because it utilizes fluorescent molecular markers to highlight the location of the cancerous tissue and enables high signal-to-background imaging. Fluorescence-based intraoperative imaging techniques were first explored in the 1950s using fluorescein to identify brain tumors [8]. With the recent FDA approval of the metabolic marker 5-ALA, brain cancer surgery is routinely performed under image guidance [9]. The visible-spectrum fluorescence emitted by both fluorescein and 5-ALA enables physicians to assess the location of tumors under a surgical microscope. However, due to tissue's high absorption coefficients in the visible spectrum, only fluorophores near the tissue surface can be imaged, which limits its diagnostic potential. For imaging more than a few millimeters below the surface of the skin, near infrared (NIR) fluorophores (700 to 950 nm) are used because of the low absorption coefficient of water and oxy- and deoxy-hemoglobin in this spectrum [10-12]. Furthermore, the low auto-fluorescence in the NIR spectrum coupled with the use of non-ionizing radiation enables high contrast to background imaging without exposing the patient to harmful radiation [13].

Despite the fact that the first fluorescence-based IGS was performed more than 70 years ago, molecular imaging in the NIR spectrum is not widely accepted as the standard of care for cancer surgery because (1) current state-of-the-art NIRF imaging systems are bulky and costly, (2) they lack both sensitivity under surgical illumination and co-registration accuracy between multimodal images [10-12].

To address these shortcomings, I have developed, designed and tested a compact, handheld, bio-inspired, single-chip, multispectral imaging device for image-guided cancer surgery. The image sensor is realized by monolithic integration of pixelated spectral filters with a custom CMOS image sensor. The custom CMOS image sensor, fabricated in Tower Semiconductors 180 nm process dedicated for image sensor, has custom peripheral circuitry that enables pixel wise control of light exposure. Hence, each group of pixels in the imaging array (i.e. red, green, blue and NIR pixels) can capture information with maximum signal-to-noise ratio and high contrast for each individual channel. The monolithic integration of filters and pixels enables temperature invariant co-registration accuracy between NIR and color images. This co-registration accuracy is critical for complete resection of all cancerous tissue and prevention of iatrogenic damage to healthy tissue. Detailed optoelectronic evaluation of the sensor is presented in this chapter, followed by both preclinical and clinical evaluation of the sensor.

## **5.2 System Overview of Handheld, Bio-Inspired Image Sensor**

Surgery is the primary curative option for patients with cancer. During open surgery, the physician uses his or her touch and eyesight to identify cancerous tissue. However, tumor margins are very difficult to identify because healthy and tumor tissues blend in very well in terms of color and structure. To alleviate this issue, I have developed a compact, handheld multispectral imaging

device that can be inserted in the surgical wound site and enable physicians to evaluate tumor margins (Figure 5.1). The image sensor is comprised of three major components: a compact lens for the collection of visible and NIR light, a custom CMOS image sensor with pixelated visible-NIR pixels and independent exposure control for different subpixels in the imaging array, and a data acquisition module for data transfer, image processing and display.

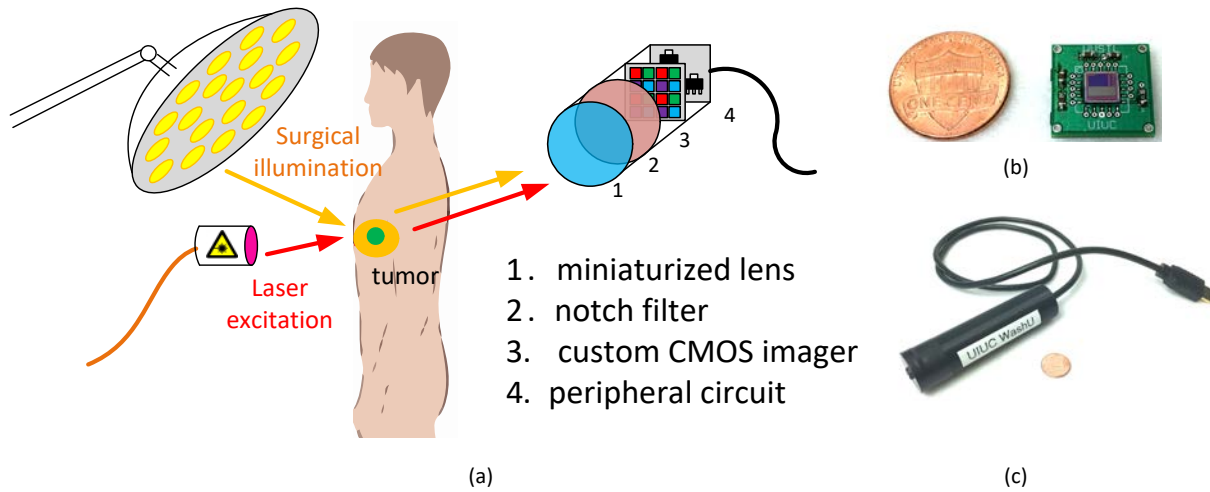


Figure 5.1 System overview (a): System block diagram showing the fluorescence contrast agent injected into the patient's body prior to imaging. A NIR laser excites the fluorophore, and the custom image sensor captures the NIRF emission. The data are buffered by the field-programmable gate array (FPGA) data acquisition module and transferred to a PC. (b) Miniature image sensor next to a penny for scale. (c) Handheld prototype of my imaging device used during surgery.

### 5.2.1 Custom Multi-Exposure Color/NIR CMOS Image Sensor

There are two important aspects of my image sensor design: small form factor and independent exposure time for individual groups of pixels. The exposure control is important for the following reason. The minimum FDA-approved surgical illumination in the operating room is 40 kLux, whereas typical NIR laser light excitation is between 5 mW/cm<sup>2</sup> and 25 mW/cm<sup>2</sup>. Hence, the photon flux from the visible light reflected from tissue and fluorescence fluency rate can have a dynamic range exceeding 100 dB. State-of-the-art CMOS image sensors have typical dynamic



range of 60 dB to 80 dB, which is insufficient for intraoperative applications. Therefore, a custom CMOS image sensor with a compact form factor is necessary to address this clinical application.

The small form factor for my imaging system is important because of the need to image small surgical cavities and place the sensor as close as possible to the imaged tissue for improved magnification. An alternative approach would be to use a fiber probe to inspect the tissue of interest. However, the size and number of optical fibers will limit the imaging spatial resolution. Optical losses within the fiber would also decrease the sensitivity of the instrument, which can lead to incomplete tumor resection. Hence, using an image sensor capable of simultaneously recording color and NIR information, and that is compact enough to be placed near the tissue of interest, is the preferred approach.

To satisfy the above described criteria, I designed, fabricated and tested a custom image sensor prototype using Tower Jazz 180 nm custom image sensor technology. A block diagram and micrograph of the image sensor is presented in Figure 5.2. The sensor has 110 by 64 front-side illuminated pixels controlled by several peripheral registers, such as column and row select register, pixel reset register and charge transfer shift register. The size of the sensor is 2.2 mm  $\times$  1.3 mm including the pixel array and peripheral circuitry. Voltage regulators and digital-to-analog converters are used to provide the proper reference voltages to both pixels and peripheral analog circuits. The photo signal from individual pixels is provided to the peripheral readout circuits, where correlated double sampling and analog-to-digital conversion are performed.

After the image sensor was fabricated by Tower Jazz semiconductor, I monolithically integrated an array of pixelated spectral filters on the surface of the CMOS image sensor. The pixelated spectral filters were realized by depositing different thicknesses of alternating layers of silicon

dioxide and silicon nitride. I integrated four different spectral filters in a 2-by-2 pattern across the image sensor with center passband wavelengths at the red, green, blue, and NIR spectrum. Since the four spectral filters are adjacent to each other, the color and NIR images are inherently co-registered. The co-registration accuracy was independent of the operating temperature and distance of the imaged object, which is not the case with FDA-approved NIRF instruments [15].

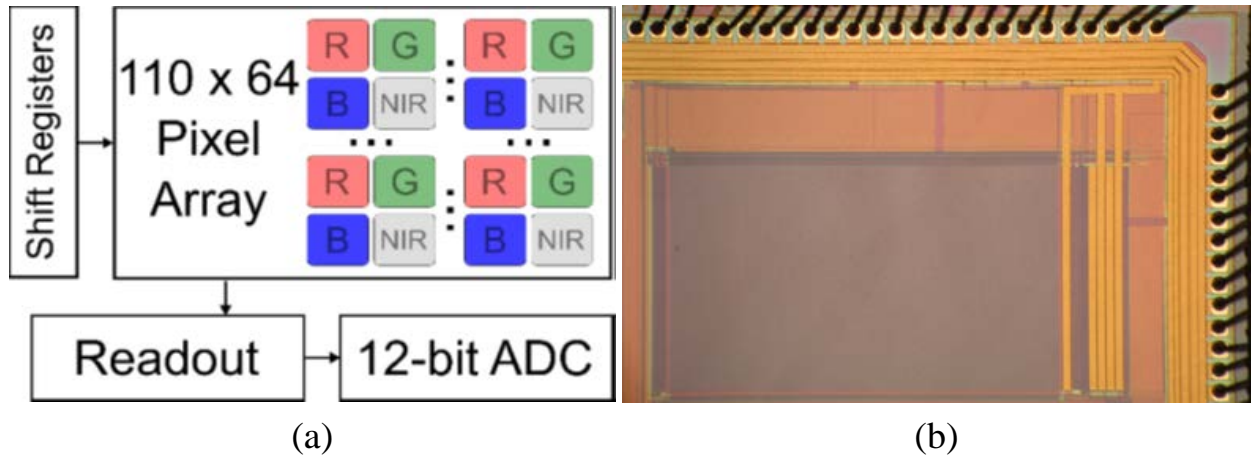


Figure 5.2 (a) Circuit diagram of the image sensor. The pixel topology consists of a 2 by 2 super pixel pattern repeated across the 110 by 64 imaging array. (b) Chip micrograph.

Figure 5.3 (a) shows the pixel schematic of my custom image sensor. The pixel is composed of a photodiode and four transistors: reset, charge transfer, source follower and address transistors. The charge transfer transistor is optimized to allow full transfer of all charges from the photodiode capacitance to the floating diffusion node. To minimize the pixel pitch, the reset potential bus and the readout bus are shared. The readout circuitry controls the connectivity of the pixel output bus. During the reset phase of the pixel, the output bus is connected to a  $V_{reset}$  potential, which sets the voltage on the photodiode node. During the readout phase, the output bus is connected to a current source, and the photodiode voltage is read out from the pixel.

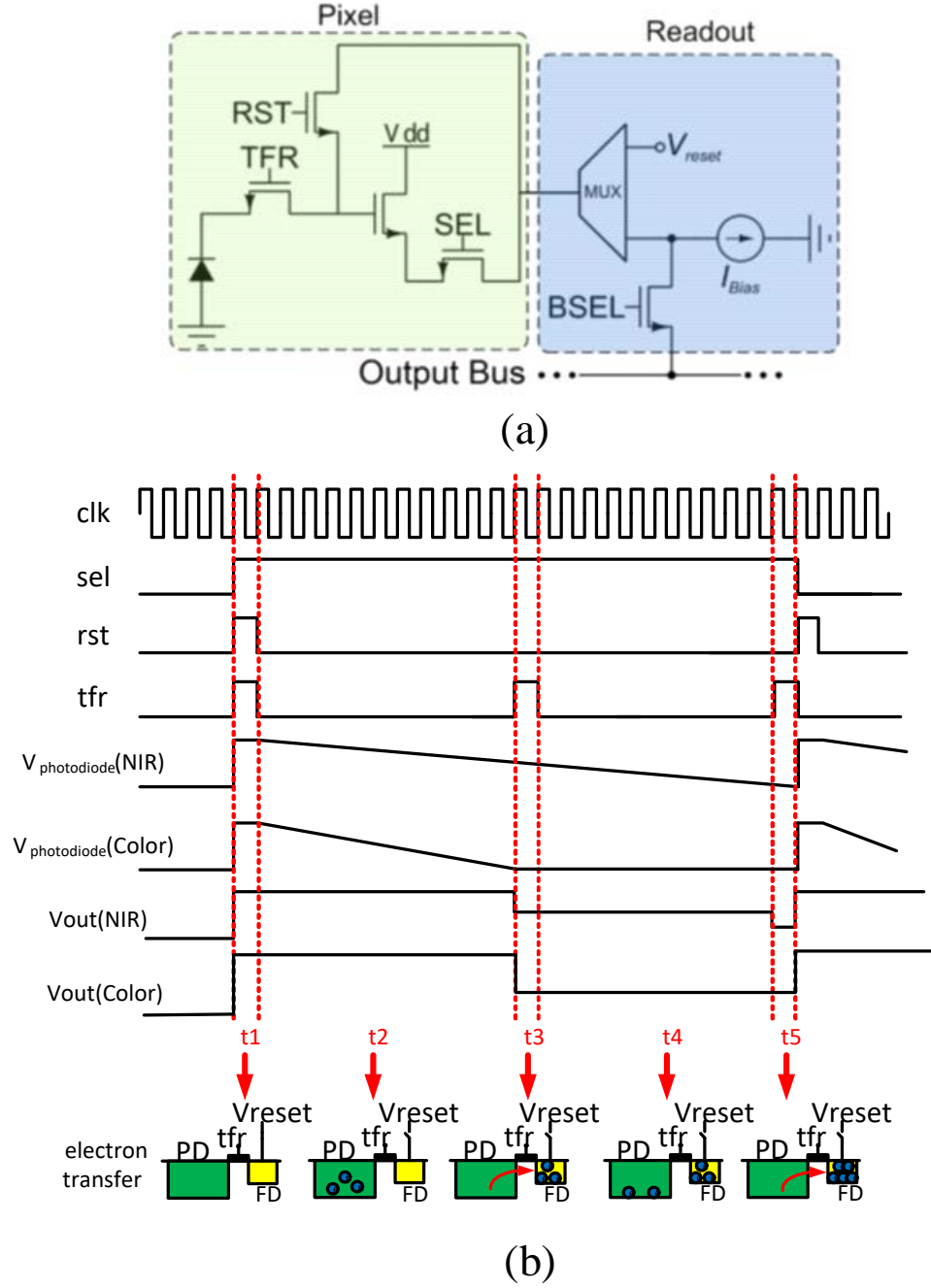


Figure 5.3 (a) Schematic of the pixel utilized in my custom image sensor. The typical 4-transistor active pixel architecture uses a shared reset and output bus to increase the fill factor. (b) Timing diagram of the read-out sequence. The multi-exposure readout scheme increases the signal level of the NIR channel.

The timing sequence for reading out both color and NIR pixels is shown in Figure 5.3 (b). During the reset phase ( $t1$ ), all pixels are reset to  $V_{reset}$  potential by setting a high RST signal. The charges in the potential well of the photodiode and the float diffusion node are cleared during this phase.

The voltage at the float diffusion node is read out for correlated double sampling (CDS). After a short exposure time ( $t_2$ ), the charge transfer transistors of visible pixels are turned on ( $t_3$ ) and charges accumulated on the photodiode ( $Q1$ ) during  $t_2$  are transferred to the floating diffusion node. After the charge transfer is completed, all visible spectrum pixels are read out. After a longer exposure time ( $t_4$ ), the charge transfer transistors of the NIR pixels are turned on ( $t_5$ ) and the photodiode charge ( $Q2$ ) accumulated on the photodiode is transferred on the floating diffusion node. The NIR pixels are read out only from the imaging array during the next timing sequence. Finally, all pixels are reset and another frame is started.

### 5.2.2 Pixelated Color/NIR Filters

Pixelated spectral filters were designed by stacking layers of materials with different dielectric constants and different thicknesses. The pixel's transmission can be modeled by equation (5.1):

$$\begin{bmatrix} B \\ C \end{bmatrix} = \left\{ \sum_{r=1}^q \begin{bmatrix} \cos \delta_r & (i \sin \delta_r) / \eta_r \\ i \eta_r \sin \delta_r & \cos \delta_r \end{bmatrix} \right\} \begin{bmatrix} 1 \\ \eta_m \end{bmatrix} \quad (5.1)$$

where  $q$  is the number of thin film assemblies in the filter,  $\eta_r$  is the optical admittance of each thin film,  $\delta_r$  is the phase factor of the light in each thin film, and  $\eta_m$  is the optical admittance of the substrate. The optical admittance of the filter is a function of the index of refraction and incident angle of the incoming light beam. The phase factor is a function of the index of refraction, the thickness of the film, the frequency of the light and the incident angle. The transmission of the filter is described by equation (5.2):

$$T = \frac{4\eta_0 \text{Re}(\eta_m)}{(\eta_0 B + C)(\eta_0 B + C)^*} \quad (5.2)$$

By tuning the material and thickness of each layer, spectral filters with different cutoff frequencies can be achieved. The spectral filters were realized by using physical vapor deposition (PVD) to

alternatively deposit layers of low dielectric material, SiO<sub>2</sub>, and high dielectric material, TiO<sub>2</sub>, onto the top surface. The spectral filters were pixelated and matched the 7.4  $\mu\text{m}$  pitch of the underlying CMOS pixels. A cross-sectional profile of a single pixel with interference filters residing on top is presented in Figure 5.4. The photodiode was realized by doping two silicon junctions with positive and negative ions. The three metal layers (M1, M2 and M3) are metal connections between the four transistors in the pixel. The interference filter has a periodic pattern of the two dielectric materials.

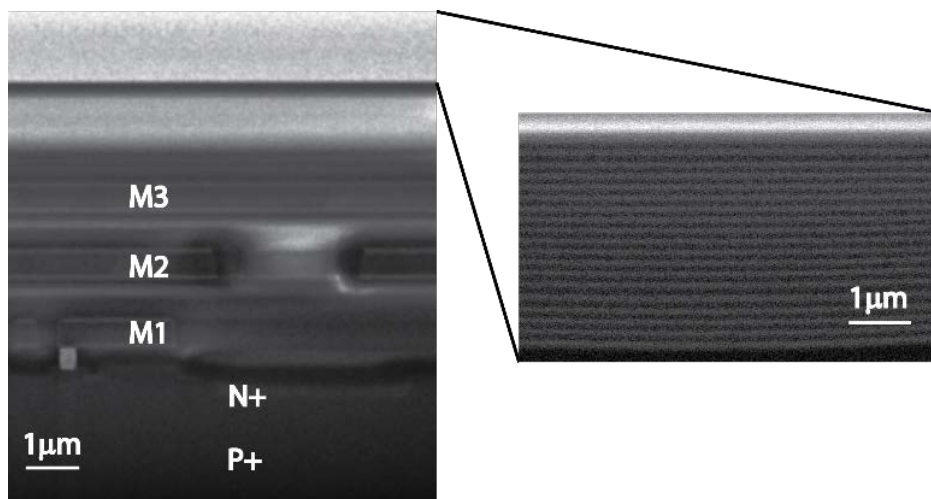


Figure 5.4 SEM micrograph of the interference filter and the underlying pixel. The interference filter is realized by alternatively stacking dielectric layers with high and low indices of refraction.

### 5.2.3 Lens and Spectral Filter

A miniature lens with an  $f/4.5$  aperture and a fixed focal length of 27 mm is integrated with the image sensor. The diameter of the lens is 12 mm, and the weight of the lens is 30 g. The miniature form factor of both lens and image sensor reduced the overall size and weight of the handheld system to improve compactness and maximize ergonomics. Because a 780 nm laser light source is used to excite the molecular probe, a notch filter (NF03-785E-25, Semrock) with high optical density ( $\text{OD} = 6.011$ ) was placed between the lens and the image sensor.

### **5.2.4 Data Acquisition Module, Image Processing and Display**

A 12-bit parallel data stream is acquired and serialized by a field-programmable gate array (FPGA) data acquisition board (XEM3010, Opal Kelly Inc., USA). The data from the image sensor is transferred to a computer (Thinkpad W530, Lenovo) via a USB 2.0 port. System software and firmware ensured that no frames or pixel data are dropped during the serial transfer of data. A custom program written in C++ acquires the data from the image sensor and performs color correction and flat field calibration for all pixels in the four different channels. The calibrated data is split into color image acquired after short integration time, NIR image acquired after long exposure time and a composite image with both imaging modalities combined. The C++ program utilized parallel threads such that when data is recorded to a solid state hard drive, high priority is allocated to the saving thread. Hence, no data is lost when saving the data, whereas some data may be skipped or lost when displayed on the screen.

## **5.3 Optoelectronic Performance Evaluation**

The image sensor's performance is evaluated for quantum efficiency, divergence response, fixed pattern noise, signal-to-noise ratio and sensitivity using the optical setup depicted in Figure 5.5. The setup consists of a computer-controlled monochromator (Acton SP2150, Princeton Instrument), an adjustable iris (SM2D25, Thorlabs), an aspheric collimating lens (ACL7560, Thorlabs) and a motor-controlled rotation stage (NR360S, Thorlabs).

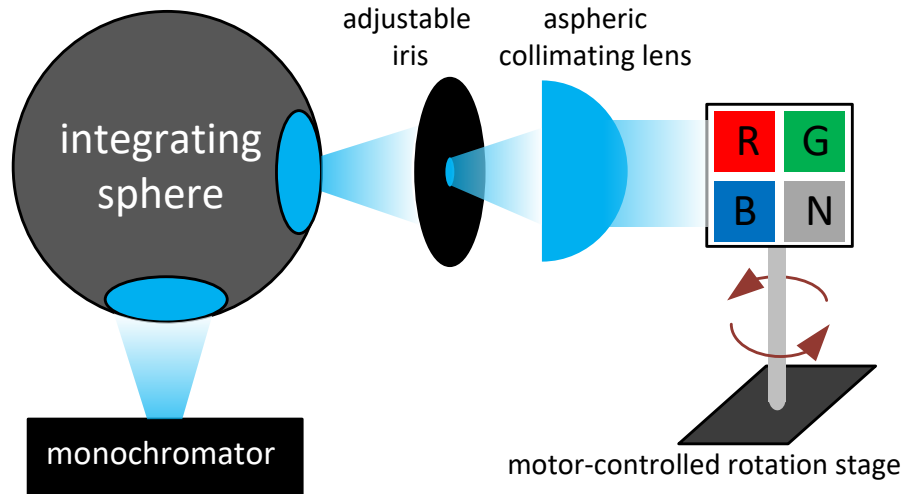


Figure 5.5 Block diagram of the optical setup for optoelectronic characterization of my custom multispectral image sensor.

Quantum efficiency is defined as the ratio of photon-generated electrons to the number of incident photons. The number of electrons is calculated from the conversion gain of the sensor and the digital output. The number of photons is measured by a calibrated photodiode (S130C, Thorlabs) driven by a power meter (PM100D, Thorlabs). The incident wavelengths are swept from 400 nm to 1000 nm in 10 nm step increments and the monochromatic light impinges on the surface of the image sensor at normal incident angle.

The quantum efficiency of the image sensor is presented in Figure 5.6. The blue, green, and red filters have quantum efficiency (QE) peaks of approximately 18% at 450, 550, and 625 nm, respectively. The NIR pixel had a peak QE of 8.5% at 805 nm, which matched the peak emission wavelength of indo-cyanate green (ICG) dye used during surgery. The sensor under testing also contained an additional notch filter at 780 nm to block the excitation light for ICG fluorophores.

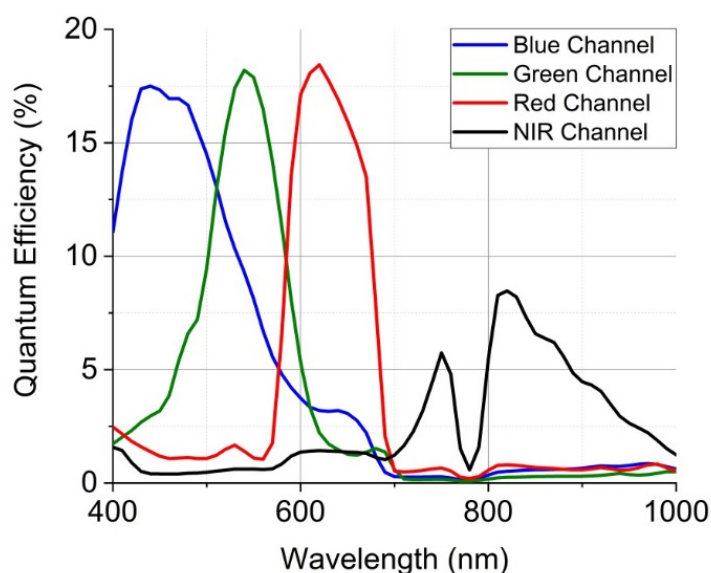


Figure 5.6 Quantum efficiency of the image sensor. Peak QE of the color and NIR channel are 18% and 8.5%.

The low quantum efficiency of the pixels was partially due to the lack of micro-lens array on each pixel and the shallow p-n junction utilized in the process. The use of micro-lens array and deeper p-n junctions to realize photodiodes would significantly increase the quantum efficiency especially in the NIR spectrum.

The light's incident angle on the interference filters affects the transmission band. When the incident angle increases, the distance that light travels within each thin film layer of the interference filter increases causing a change in the phase factor  $\delta$ , as described by equation (5.2). Since the fluorescence emitted by a molecular probe radiates equally in all directions, the transmission band of the interference filter will shift toward shorter wavelength. This phenomenon is called "blue shift". Blue shifting will cause leakage of backscattered excitation light, resulting in a low signal-to-background ratio and a decreased sensitivity at peak emission wavelengths for ICG. As a result, the detection limit of fluorescence is compromised.



To evaluate the impact of divergent light on the image sensor, I rotated the sensor such that the incident angle was swept from  $0^\circ$  to  $30^\circ$  in increments of  $5^\circ$ . The recorded spectral response is shown in Figure 5.7.

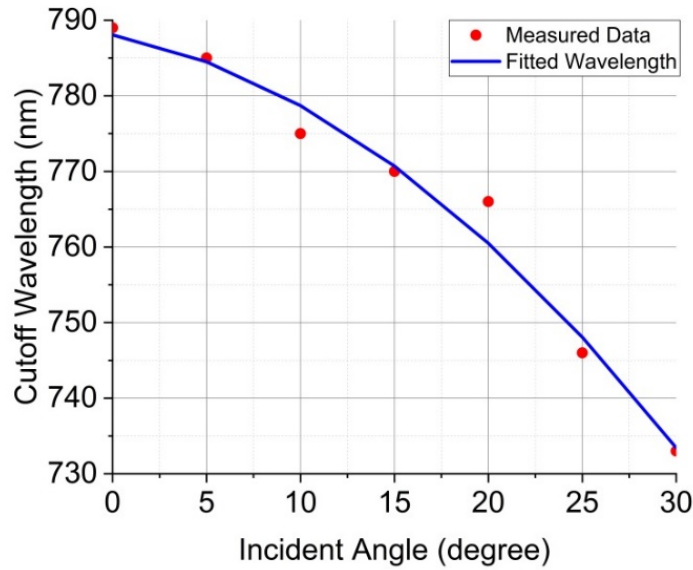


Figure 5.7 Divergence response of the interference filter. The cutoff wavelength decreases as the incident angle increases. This is called the “blue-shift” effect. Blue shift will cause leakage of NIR excitation as well as visible illumination to the NIR channel, which degrades the NIR image quality and the fluorescence detection limit.

The figure indicates that when the incident angle for the incoming light is less than  $10^\circ$ , the cutoff wavelength for the NIR filter is decreased by 15 nm. Since the full-width at half-maximum for the notch filter is 15 nm, the excitation light source is successfully suppressed. In real applications, the sensor is placed behind the lens. The chief ray angle (CFA) of the lens is the angle of light incident directly on the surface of the sensor. By selecting the correct lens and properly limiting the field of view, the CFA can be constrained to maintain the performance of the sensor. When the CFA angle exceeds  $10^\circ$ , the passband for the NIR filter will be significantly blue shifted and excitation photon will be registered by the NIR pixel. At high CFA angles, the detection limit of ICG will be therefore significantly decreased.

The spatial non-uniformity of the sensor is characterized by fixed pattern noise (FPN). The FPN versus signal level is shown in Figure 5.8(left). The maximum FPN for visible spectrum pixels is approximately 16% at full well, and the FPN for the NIR spectrum pixels is approximately 12%. Although CDS removes most of the dark current non-uniformity (DCNU), the fabrication dependent non-uniformity of the pixelated filter introduces photo-response non-uniformity (PRNU), which is the dominant source of FPN. The major defect in the filters is the structural collapse of the dielectric layers near the pixel edge. To suppress the FPN, flat field correction method is introduced. The FPN after calibration is shown in Figure 5.8(right) where the maximum FPN is less than 2% at full well dynamic range.

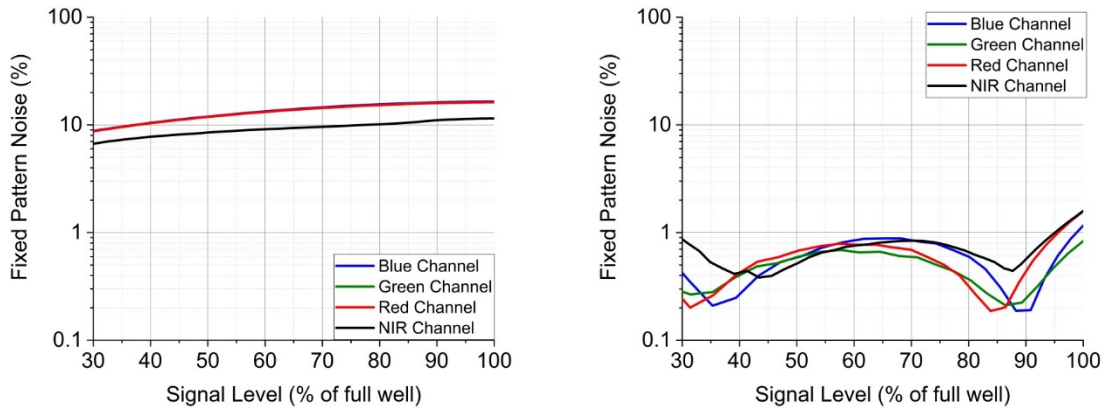


Figure 5.8 (left) Uncalibrated FPN versus signal level. The FPN increases monotonically with signal level. The maximum FPN is 16% (color channels) and 11% (NIR channel) at full well. (right) Calibrated FPN versus signal level. The FPN is less than 2% for all intensities.

The signal-to-noise ratio (SNR) is evaluated using the same optical setup that is used for the FPN measurement. The SNR versus signal level is shown in Figure 5.9. The SNR at a low signal level is limited by the readout noise of the sensor, which is  $54e^-$ . As the signal level increases, the photon shot noise becomes the dominant source of the noise and SNR approaches the shot noise limit. To obtain the best quality image and maximum detectability, the multi-exposure scheme is used to ensure that both color and NIR channels have sufficient signal levels to maintain high SNRs.

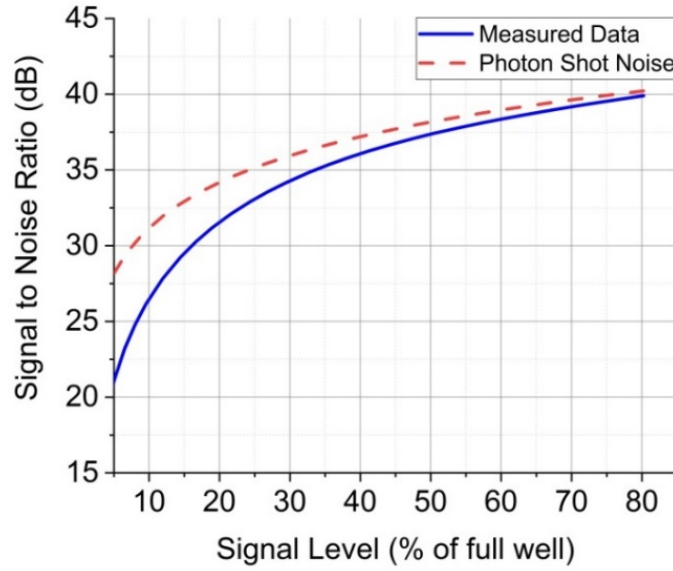


Figure 5.9 Signal-to-noise ratio versus signal level. At low illumination levels, the readout noise dominates the signal, whereas at a high illumination levels, the photon shot noise dominates the output signal.

A summary of the image sensor performance is presented in Table 5.1

Table 5.1 The summary and comparison between this multi-exposure multispectral image sensor and related work.

Description	This work	[49]	[50]	[51]
Filter type	<b>Stacked dielectric</b>	Plasmonic	Fabre-Perot	Fabre-Perot
Detection range (nm)	<b>400-1000</b>	400- 700	470- 1000	400- 750
# of spectral bands	<b>4</b>	6	100	3
Visible bandwidth (nm)	<b>80-100</b>	100-150	10	100-150
Visible transmission	<b>60%</b>	50%	85%	65%
NIR bandwidth (nm)	<b>&gt;250</b>	N/A	10	N/A
NIR transmission	<b>80%</b>	<10%	85%	<5%
NIR filter optical density	<b>2.5</b>	N/A	>2	N/A
NIR filter type	<b>long pass</b>	N/A	band pass	N/A
Multi-exposure	<b>Yes</b>	No	No	No
Pixel size ( $\mu\text{m}$ )	<b>7.4</b>	10	5.5	1.75
Number of pixels	<b>7k</b>	10k	2M	3M
Fabrication technology	<b>0.18 <math>\mu\text{m}</math> CMOS</b>	0.35 $\mu\text{m}$ CMOS	CMOS	CMOS
Fill factor	<b>50%</b>	N/A	N/A	N/A
Well capacity	<b>25k electrons</b>	N/A	N/A	N/A
Input referred noise	<b>54 electrons</b>	N/A	N/A	N/A
Maximum SNR	<b>45 dB</b>	N/A	N/A	N/A
Dynamic range	<b>54 dB</b>	N/A	N/A	N/A
Power consumption	<b>150 mW</b>	N/A	N/A	N/A

An important attribute for the camera is the lowest detectable ICG concentration under surgical light. I prepared vials with aqueous solutions of ICG at different concentrations from 1 nM to 1000

nM. The vials are placed 20 cm from the camera to emulate typical distance during clinical trials. A control group with deionized water is used to measure background signal. The vials are illuminated with a modified light emitting diode surgical light source [52] providing approximately 40 kLux luminance and a 780 nm excitation light source (BWF2-780-0.8-200-0.22-SMA, BWTEK) filtered with a laser clean-up filter (LL01-780-12.5, Semrock). The optical power of the excitation source is 10 mW/cm<sup>2</sup>. The exposure time is set to 10 ms for color pixels and 35 ms for NIR pixels. The mean and standard deviation of the fluorescence signal are calculated from a region of 10 by 10 pixels. The experiments are repeated three times with the different vials with the same ICG concentrations. The results are plotted in Figure 5.10. The dashed lines represent the average fluorescence intensity level of the control group  $\mu_0$  plus 3 times the standard deviation of the average signal  $\sigma_0$ . The solid lines show the normalized average fluorescence intensity level of different ICG concentrations  $\mu_k$ . The detection limit of the camera is defined as:

$$\mu_{\text{limit}} = \text{argmin}_{\mu_x} (\mu_x > \mu_0 + 3\sigma_0) \quad (5.3)$$

Because the NIR pixels are sufficiently exposed regardless of the short exposure time of visible color channels, the multi-exposure camera can detect 50 nM ICG. Compared with single-exposure results with detection limit of 100 nM, the performance was twice as high.

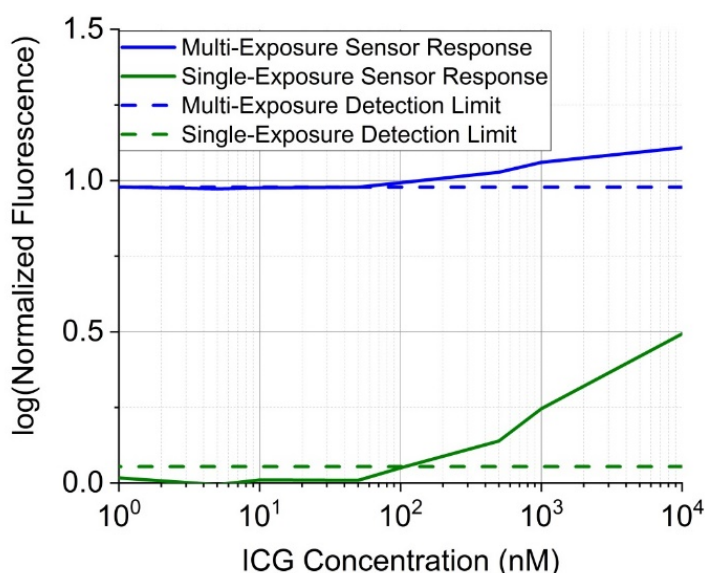


Figure 5.10 Sensitivity for different ICG concentrations. The horizontal dashed lines represent the detection limit, while the solid lines represent the photo response. The multi-exposure sensor can detect 50 nM ICG.

## 5.4 Imaging Spontaneous Tumors Under Surgical Light Illumination

I used my bio-inspired sensor to identify spontaneous tumor development in a transgenic PyMT murine model for breast cancer (n=3). All animals developed multifocal tumors throughout the mammary tissues by 5-6 weeks, and some of the small tumors blended in well with surrounding healthy tissue due to their color and were difficult to differentiate visually with the unaided eye. However, because my bio-inspired sensor has high co-registration accuracy and NIRF sensitivity, the physician could easily locate the tumors, resect them, and ensure that the tumor margins were negative (Figure 5.11). When I compared results obtained with my bio-inspired image sensor against histology results, I found that my sensor together with the tumor-targeted probe had a sensitivity of 78%, a specificity of 73%, and an area under the receiver operator curve of 72% using parametric analysis. In addition, while visible-spectrum imaging picks up only surface information, fluorescence imaging in the NIR spectrum enables deep-tissue imaging, which helps

identify the location of tumors before surgery. Compared to the state-of-the-art, non-real-time, bulky Pearl imaging system, with a receiver operator curve of 77.9% and relevant standard error of 7.1% [53], my bio-inspired sensor provides similar real-time accuracy under surgical light illumination.

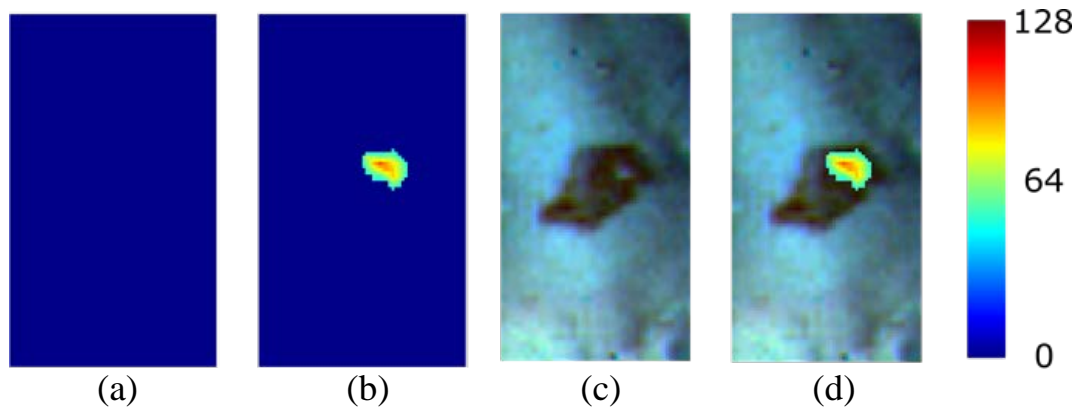


Figure 5.11 In vivo preclinical mouse study. NIR images use jet color map. (a) Single-exposure NIR image; (b) multi-exposure NIR image; (c) color image; (d) superimposed image.

## 5.5 Clinical Translation of My Bio-Inspired Technology

My bio-inspired, handheld image sensor was then used in an operating room to track sentinel lymph nodes (SLNs) in patients with breast cancer. Human study protocols were approved by the Institutional Review Board of Washington University in St. Louis. The human procedure was carried out in accordance with approved guidelines. The inclusion criteria for patients in this study were newly diagnosed clinically node-negative breast cancer, negative nodal basin clinical exam, and at least 18 years of age. The exclusion criteria from this study were contraindication to surgery; receiving any investigational agents; history of allergic reaction to iodine, seafood, or ICG; presence of uncontrolled intercurrent illness; or pregnancy or breastfeeding. All patients gave informed consent for this HIPAA-compliant study. The study was registered on clinicaltrials.gov website (trial ID no. NCT02316795).

The mean $\pm$ SD age and body mass index of all patients were 64 $\pm$ 14 years and 32.7 $\pm$ 6.9 kg/m<sup>2</sup>. Before the surgical procedure, <sup>99m</sup>Tc-sulfur colloid (834  $\mu$ Ci) and ICG (500  $\mu$ mol, 1.6 mL) were injected into patient's tumor area, followed by site massage for approximately 5 min. At 10-15 min post injection, physicians proceeded with the surgery per standard of care. Once the physician identified the SLNs using the visible properties of ICG (i.e., green color) and radioactivity using the gamma probe, the physician used my bio-inspired imaging system to locate the SLNs. The patients were imaged under simultaneous surgical light illumination (60 kLux) and laser light excitation power of 10 mW/cm<sup>2</sup> at 785 nm. The physician then proceeded with the resection of the SLNs. The imaging system was set up at a 1 m working distance, and the illumination module was placed at a 1 m distance. The color pixels' exposure time was set to 10 ms to ensure non-saturated color images were recorded, and the NIR pixels' exposure time was set to 35 ms to ensure imaging rates of 25 frames/sec. The average imaging time with my bio-inspired sensor was 2.5 $\pm$ 0.6 min.

In a pilot clinical trial, I investigated the utility of my bio-inspired image sensor to locate SLNs in human patients (n=3) with breast cancer using the ICG lymphatic tracer. ICG naturally exhibits a green color due to its absorption spectra, as well as NIRF at 800 nm. ICG passively accumulates in the SLNs and is cleared through the liver and bile ducts within 24-36 h post-injection.

Figure 5.12 presents images of SLN tissue resected from a patient and displayed on a monitor to the physician. The color images recorded by my sensor provide information about the anatomical features of the patient, while the NIR image provides information about the location of the sentinel lymph nodes. Because both images were inherently co-registered and with the help of superimposed color-NIR information, the physician can easily identify anatomical features that need to be resected (Figure 5.12 (d)) and identify healthy tissue that needs to be preserved.

At the same exposure times for both visible and NIR pixels, i.e., 10 ms, the color image (Figure 5.12 (c)) showed good contrast between various regions in the SLN and the surrounding tissue. However, the NIR pixels captured only few photons, and the NIR image (Figure 5.12 (a)) had poor contrast and a poor SNR. Hence, the physician was unable to locate the SLN with high confidence using the NIR image obtained with short exposure time. When the exposure time for the visible and NIR pixels was decoupled and the NIR exposure time was set to 35 ms, a brighter NIR image (Figure 5.12 (b)) was obtained and the locations of the sentinel lymph nodes were accurately determined and resected. Because the exposure time was optimized for the color and NIR pixels separately, a high contrast color image and high contrast NIR image were obtained during the surgical procedure and presented to the physician.

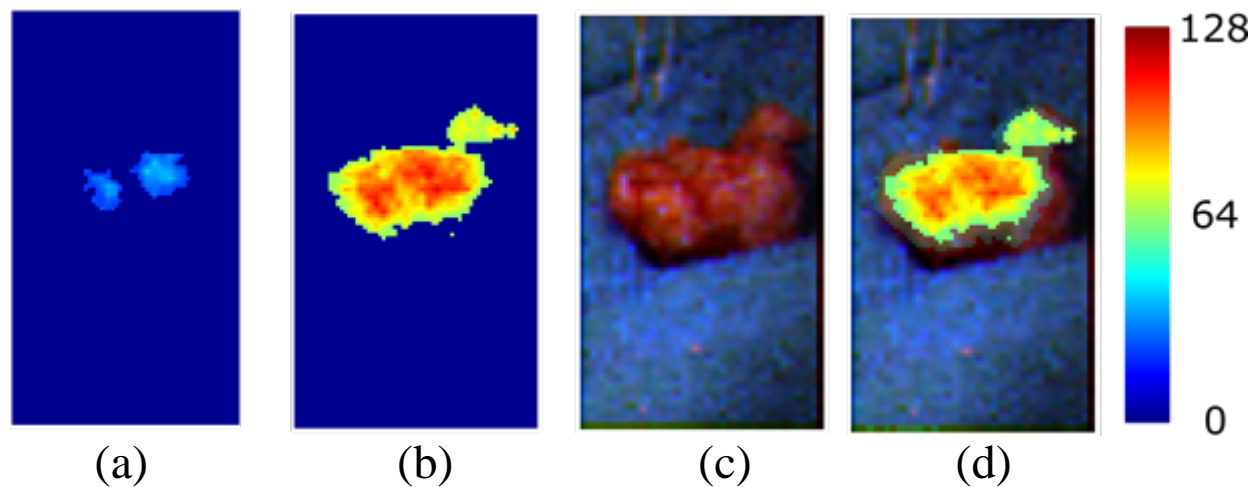


Figure 5.12 Human SLN surgery study. NIR images use jet color map. (a) Single-exposure NIR image; (b) multi-exposure NIR image; (c) color image; (d) superimposed image.

## 5.6 Conclusions

This chapter described a handheld, bio-inspired, multispectral image sensor for image-guided surgery. Due to the monolithic integration of spectral filters with an array of imaging elements, a compact and ergonomic imaging device is realized for evaluating incision wounds for residual



cancer cells. The sensor is used in preclinical experiments to detect tumor cells in PyMT spontaneous breast cancer model. I also translated this sensor in the operating room to detect lymph nodes in patients with breast cancer. The compact form factor of my sensor enabled both seamless integration of the sensor into the surgical suite and presentation of time-critical information to the physician.

# **Chapter 6: Head-Mounted Augmented Reality System with Microsoft HoloLens for Near-Infrared Fluorescence-Based Image-Guided Surgery**

## **6.1 Introduction**

The successful detection and complete removal of cancerous tissue without damaging surrounding healthy tissue remains a challenge [54]. Surgeons rely on traditional techniques, such as visual inspection and touch, as their primary sensing modalities. Due to low visual and structural contrasts, surgeons have to subjectively determine whether all cancerous tissues were removed and whether iatrogenic damage was introduced during surgery. Typically, secondary surgeries are required to remove any remaining tumor tissues and/or to repair damage inflicted to healthy tissue during the primary surgery. Approximately 20% to 70% of patients with breast cancer require additional surgeries [5].

To provide surgeons with additional anatomical information about tissues/organs, X-rays, computed tomography (CT), ultrasound, magnetic resonance imaging (MRI) and positron emission tomography (PET) greatly assist in preclinical diagnosis and surgical planning. However, because of their large footprints, ionizing radiation, and slow scanning time, these devices are difficult to adapt into the operating room to give intraoperative guidance.

Image-guided surgery (IGS) solves these problems by providing intraoperative structural and functional tissue or organ information to surgeons in clinical settings. Because near-infrared fluorescence (NIRF) has 1) low auto-fluorescence in human tissue, 2) low tissue scattering and absorption in the NIR region, and 3) an invisible fluorescent spectrum to the human eye, NIRF is

of particular interest for IGS [10]. Two non-specific NIR fluorescent dyes have been approved by the FDA: methylene blue (MB) [55] and indo-cyanine green (ICG) [56]. In addition, target-specific NIR dyes have been developed by laboratories in academia and industry in the past few years [56-58]. These dyes enable NIR IGS to provide high contrast deep imaging in the range of millimeters to a centimeter [32, 33, 59] and interference-free surgical workflow and light sources, allowing the surgeon to quickly and accurately identify tumors.

Because the NIRF wavelength is invisible to human eyes, specialized imaging systems are required. The systems should be capable of superimposing real-time NIRF images over visible anatomical features. The systems should also be compact and light enough to provide hands-free operation in the operating room. State-of-the-art NIRF IGS devices such as FLARE [32], SPY [33], and PDE [34] use two charge-coupled device (CCD) imaging sensors for visible spectrum imaging and NIR imaging. Using optimized dichroic beam splitters and spectral filters, color and NIRF images are captured and co-registered. However, these systems have several major shortcomings. As shown in Figure 6.1(left), one of the most severe shortcomings is that the combined NIR and color information is presented on a remote computer monitor. Surgeons have to look up at the monitor and memorize the image before continuing with the resection. Another shortcoming is the large footprint and high costs of these systems. These limit the intraoperative clinical translation of the systems.

Recently, video display goggles for NIRF IGS have been developed. Gao et al. developed a compact threshold detection-based complementary metal-oxide-semiconductor (CMOS) imaging goggle system [18]. Color and NIRF information was overlaid and displayed on a head-mounted device (HMD) with an opaque liquid crystal display (LCD) screen. This system had a minimized footprint and enabled hands-free operation without interfering with the surgical workflow.

However, the natural vision of the surgeon was blocked. Because surgeons are trained to use their natural vision, use of LCDs requires training and complicates the clinical translation of this technology. Liu [60], Armstrong [61], Shao [62] and Modal [19] developed transparent HMD using custom optics or Google Glass. Surgeons were able to see through the transparent display units. Although the virtual NIRF images captured by NIR cameras were correctly overlaid with the virtual color image captured by secondary cameras, none of these technologies co-registered the virtual fluorescence image with the natural vision of the surgeons. Liao [63] developed a see-through augmented reality system for MRI guided surgery. This system co-registered the imaging target, the virtual image and the vision of the surgeon using a half-silvered mirror. However, the virtual image and its location are calculated using pre-operative MRI data. No real-time data were transmitted. The virtual NIRF image always followed the surgeon's eyesight. The image either distorted, shifted, or even completely disappeared when the perspective changed. The structural and functional information that NIRF provides becomes less informative.

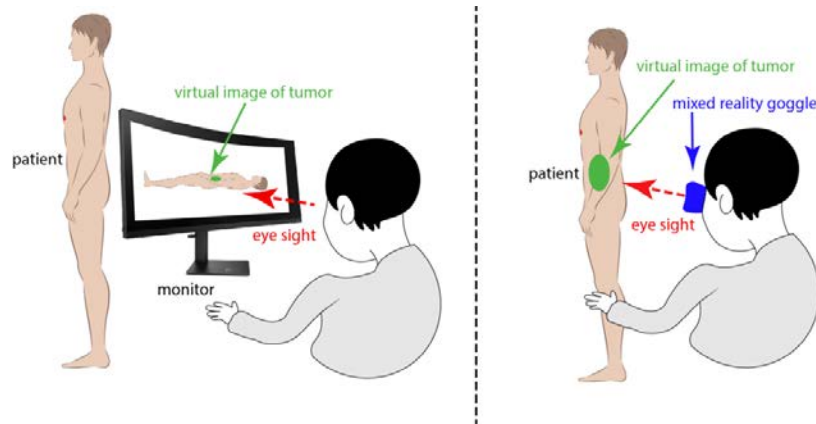


Figure 6.1 Comparison between the monitor-based display (left) and augmented reality-based display (right). Instead of displaying both the virtual NIRF image and virtual color image on a monitor, the augmented reality-based display system superimposes the virtual NIRF image directly on top of the patient's body.

In this chapter, I present an augmented reality NIRF imaging system using Microsoft HoloLens.

Unlike the traditional augmented reality systems presented by Haouchine [64], Badiali [65], and

Kang [66], which augmented virtual color images (displayed on monitors) with preoperative CT/MRI/ultrasound information, the HoloLens is an augmented reality (AR) HMD that allows users to combine real-world with real-time virtual images (holograms). The HoloLens uses a transparent display with light projectors to create holograms on the glass in front of the user's eyes. It contains multiple sensors to scan the environment, which enables the holograms to be placed at a specific location in the real world, as shown in Figure 6.1 (right). Compared with other HMDs, the imaging system I developed can ensure that real-time virtual images are correctly co-registered with real-world objects regardless of user head movement and without blocking natural vision. I designed the imaging system using a single CMOS imaging sensor placed on a custom printed circuit board (PCB). Spectral filters were placed on the imaging sensor so that the imaging system was optimized for NIRF. The custom signal processing algorithm including serial/wireless data transmission. Image calibration/co-registration was implemented on the computer and on the HoloLens. I also utilized a custom-built NIR spectrum calibration board that allowed for the automatic co-registration of virtual images and real-world objects. The system sensitivity and co-registration accuracy were evaluated. An animal model was used to demonstrate the application of this system. The advantages of this system are also discussed.

## **6.2 System Setup and Co-Registration Algorithm**

### **6.2.1 System Setup**

Figure 6.2 depicts the entire imaging system including the fluorophore excitation laser, custom NIR camera, calibration board, wireless router and the HoloLens.

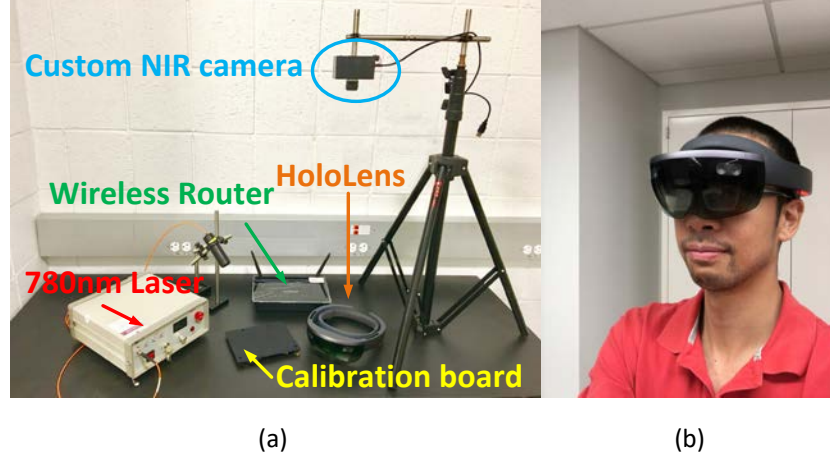


Figure 6.2 Augmented reality imaging system for NIRF IGS. (a) System setup including a custom NIR camera, a wireless router, a 780-nm laser with its optics, a calibration board and a HoloLens. (b) User wearing the HMD.

A 780-nm laser (BWF2-780-0.8, B&W TEK Inc.) was used to excite the fluorophores. The beam was coupled by fibers (M28L05, Thorlabs) and filtered by a laser clean-up filter (LL01-780-12.5, Semrock) to minimize leakage outside the desired bandwidth. The filtered laser beam was expanded by an aspherical lens (ACL25416U-B, Thorlabs) and a diffuser (47-997, Edmund Optics) to generate a  $10\text{ cm} \times 10\text{ cm}$  uniform pattern with approximately  $20\text{ mW/cm}^2$  excitation power.

The custom NIR camera was placed at 60-cm fixed working distance looking straight down. The camera consisted of a custom PCB, including a single-chip NIR CMOS image sensor, reference voltage regulators, a USB controller and a field programmable gate array (FPGA)-based image signal processor (XEM6310 Spartan 6, Opal Kelly). A high quantum efficiency at 800 nm for the CMOS imaging sensor allowed for the efficient imaging of fluorescence signals in the NIR spectrum. The small feature size allowed for full integration with the HMD in the next-generation device. The exposure time and readout gain of the CMOS imaging sensor were programmed by FPGA using a serial peripheral interface (SPI) bus. External triggers started image acquisition to synchronize with the rest of the imaging system. Once exposure was complete, raw data were sent

to the FPGA via a serial bus. The FPGA de-serialized the 12-bit raw data and sent the data to a PC via USB 3.0 bus to generate image frames. The sensor utilized a variable exposure time ranging from 2 ms to 33 ms. The frame rate was 30 frames per second.

To reduce the background noise level and collect light from 800 nm up to 1000 nm, a 780-nm notch filter (NF03-785E-25, Semrock) were placed in front of the imaging sensor to remove visible light and fluorophore excitation light. The maximum leakage from 400 nm to 800 nm was 1.01%.

To co-register the virtual image with natural vision, a calibration board was developed. The calibration board was 6 inches  $\times$  4 inches and consisted of 4 NIR light-emitting diode (LED) tracking pods on the same plane. The LEDs (SFH4557, Osram) were centered at 860 nm and placed at fixed positions on the calibration board. Because the LEDs were bright enough to saturate the imaging sensor, assuming that the rest of the image was not saturated, the location of the LEDs within the image were determined and used by the co-registration algorithm, which was implemented by custom C++ code and OpenCV APIs on a PC.

Once the image was correctly co-registered using the algorithm, the transformed image was sent wirelessly via TCP/IP protocol using a wireless router (AC1200, Netgear). A 1200 Mbps data rate ensured support for a 30 frames-per-second transmission. The HoloLens received and rendered the data using custom C# code and Unity APIs. All data transmission and processing were performed concurrently using multi-thread programming techniques.

The signal flow is shown in Figure 6.3.

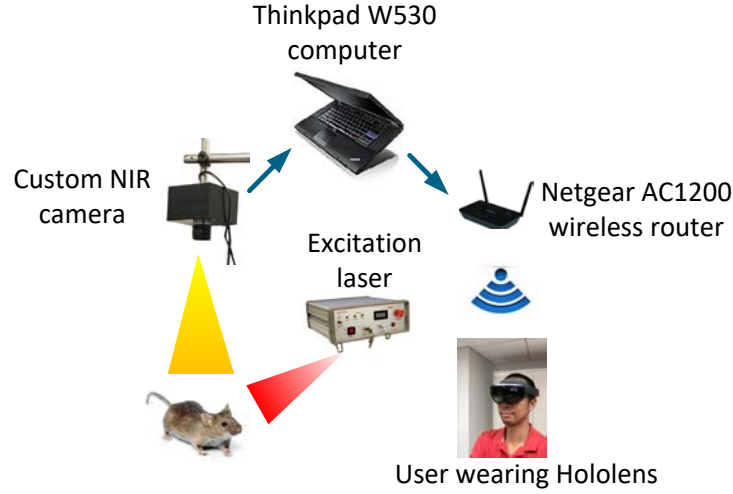


Figure 6.3 Typical signal flow using augmented reality for NIRF IGS. The custom NIR camera captures the NIRF from the target and sends the raw data to a PC. The processed data are sent wirelessly to the HoloLens.

### 6.2.2 Co-Registration Algorithm

A precise calculation of the disparity between hologram and natural vision is of great importance.

Miss-registration would result in an incorrect estimation of tumor position and lead to unsuccessful removal of all cancerous tissue and damage to healthy tissue. To co-register the imaging target between the hologram and natural vision, a co-registration calibration algorithm using an LED tracking pod was performed. The imaging region of interest (ROI) was defined by the position and size of the calibration board. Images of every target within the ROI were calibrated.

Before performing the co-registration algorithm, the camera calibration was performed. Unfortunately, all cameras are subject to distortion. Radial distortion is due to increased/decreased image magnification with distance from the optical axis, and tangential distortion is due to the imperfect alignment of optical elements with respect to the imaging plane. I used a black-white chessboard pattern to compute the distortion coefficient  $[k_1 \ k_2 \ p_1 \ p_2 \ k_3]^T$ . The distortion can be reduced by using equations (6.1) and (6.2) [67]:

$$x_{distort} = x(1 + k_1 r^2 + k_2 r^4 + k_3 r^6) + 2p_1 xy + p_2(r^2 + 2x^2) \quad (6.1)$$



$$y_{\text{distort}} = y(1 + k_1r^2 + k_2r^4 + k_3r^6) + 2p_2xy + p_1(r^2 + 2y^2) \quad (6.2)$$

where  $r^2 = x^2 + y^2$ ,  $(x, y)$  is the distortion-free points in the imaging plane and  $(x_{\text{distort}}, y_{\text{distort}})$  is the distorted points in the imaging plane.

Next, the user would use gesture and voice control to place the calibration hologram, which has a uniform default color, on top of the calibration board. The calibration hologram is the same size as the calibration board (6 inches  $\times$  4 inches), and the user would use their natural vision to ensure that the hologram is completely superimposed. This ensures that every object on this plane within the calibration board was co-registered with the user's natural vision after co-registration calibration. To evaluate the accuracy of this initial placement, the user would use a highly subjective standard. If the user was unable to determine a disparity, the initial placement was completed. Because the co-registration algorithm was completely independent of the initial placement, as long as the user was satisfied, the user will not find disparity between the real-world object and the later co-registered hologram. Once placed and once the user is satisfied with the alignment, the NIR camera would start capturing images, and the HoloLens would compute the position information of the hologram. The hologram remained at this position even if the user position changed. The hologram showed the un-calibrated image.

After the images were captured, a threshold applied to the pre-calibrated hologram. All pixel values below a threshold (95% of the dynamic range) were set to 0. Because the LEDs on the calibration plane emitted strong NIR signals, only the LEDs in the hologram were above the threshold and were detected. To compute the actual position of the LEDs in the pre-calibrated hologram, a contour detection was performed using the Canny edge detection method [68]. The positions of

the center of LEDs in the pre-calibrated hologram  $[x_{LED\_i} \ y_{LED\_i}]^T$  ( $i=1,2,3,4$ ) were defined as the image mass center of these contours.

Because the physical locations of the LEDs on the calibration plane were known, the locations  $[x_{LED\_i}' \ y_{LED\_i}']^T$  ( $i=1,2,3,4$ ) of the LEDs projected in the post-calibrated imaging plane (hologram) were easily calculated.  $[x_{LED\_i}' \ y_{LED\_i}']^T$  were co-registered with the user's natural vision. I defined the projection matrix  $T$  such that:

$$\begin{bmatrix} x_{LED}' \\ y_{LED}' \\ 1 \end{bmatrix} = T_{2 \times 3} \begin{bmatrix} x_{LED} \\ y_{LED} \\ 1 \end{bmatrix} = \begin{bmatrix} t_{11} & t_{12} & t_{13} \\ t_{21} & t_{22} & t_{23} \end{bmatrix} \begin{bmatrix} x_{LED} \\ y_{LED} \\ 1 \end{bmatrix} \quad (6.3)$$

$T$  can be retrieved by:

$$\begin{bmatrix} t_{11} \\ t_{12} \\ t_{13} \\ t_{21} \\ t_{22} \\ t_{23} \end{bmatrix} = (A^T A)^{-1} A^T b \quad (6.4)$$

where:

$$A = \begin{bmatrix} x_{LED\_1} & y_{LED\_1} & 1 & 0 & 0 & 0 \\ 0 & 0 & 0 & x_{LED\_1} & y_{LED\_1} & 1 \\ x_{LED\_2} & y_{LED\_2} & 1 & 0 & 0 & 0 \\ 0 & 0 & 0 & x_{LED\_2} & y_{LED\_2} & 1 \\ \dots & \dots & \dots & \dots & \dots & \dots \\ \dots & \dots & \dots & \dots & \dots & \dots \end{bmatrix}, b = \begin{bmatrix} x_{LED\_1}' \\ y_{LED\_1}' \\ x_{LED\_2}' \\ y_{LED\_2}' \\ \dots \\ \dots \end{bmatrix}$$

All pixels  $[x \ y]^T$  in the pre-calibrated hologram were transformed using  $T$  to obtain the calibrated value  $[x' \ y']^T$ , which was re-projected to the hologram. The co-registration algorithm was completed:

$$\begin{bmatrix} x' \\ y' \end{bmatrix} = T_{2 \times 3} \begin{bmatrix} x \\ y \\ 1 \end{bmatrix} \quad (6.5)$$

After this co-registration calibration, the hologram was co-registered with the real-world object on the calibration board and the user's natural vision. The flowchart of this algorithm is shown in Figure 6.4. Because the camera was placed at a fixed position, this co-registration was only required once to ensure that the user's initial natural vision was co-registered with the initial hologram. If the user's position changes, the HoloLens will transform the hologram to compensate for movement and to ensure that the hologram was co-registered with the user's natural vision.

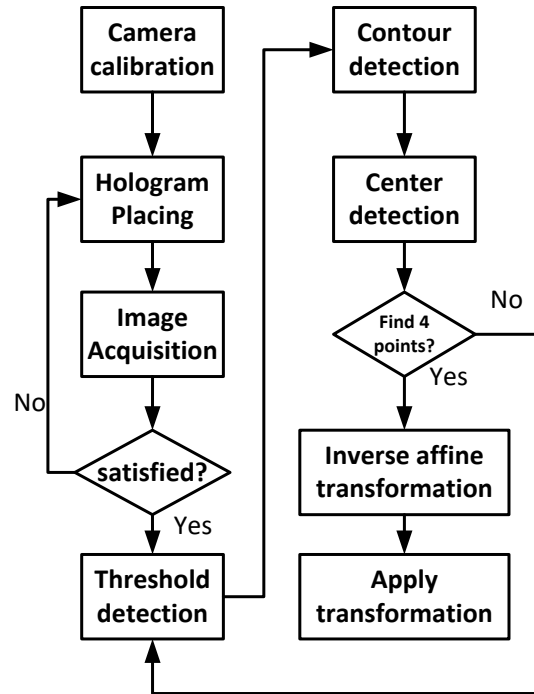


Figure 6.4 Co-registration calibration algorithm flow chart.

### 6.3 Input/Output Interface and Additional Features

In the operating room, the surgeons need distraction-free user interface. Traditional input/output (I/O) devices such as keyboards, mice, push buttons and touch screens interfere with the surgical workflow. The surgeons have to take off their gloves before selecting the desired function of an

instrument. To overcome this drawback, I implemented the voice and gesture I/O for the system. Using the HoloLens build-in microphone and infrared detector, the surgeon's voice and hand gesture can be tracked and recognized by the system to trigger the specific command.

Features such as displaying the X-ray, CT and MRI images are also implemented. The images were pre-loaded to the system prior to surgery. They provide additional information to the surgeons during operation (Figure 6.5).

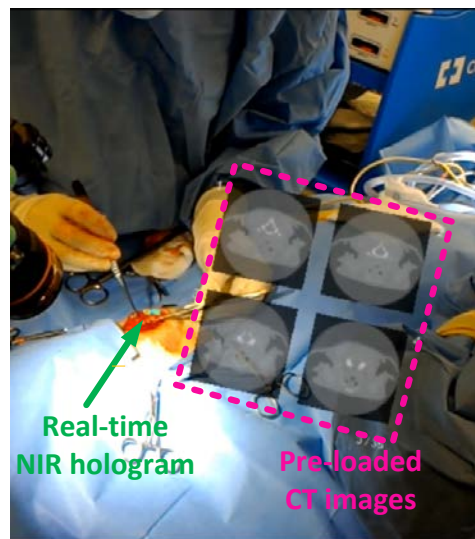


Figure 6.5 Pre-loaded CT images with the real-time NIR hologram. All commands such as zoom in/out of the CT images and going to next page is voice and gesture controlled.

## 6.4 System Evaluation

### 6.4.1 Sensitivity Evaluation

The sensitivity of this system is evaluated by NIRF signal responses for solutions with different ICG concentrations. ICG was diluted in de-ionized water. A control group with 100% de-ionized water is used as the background signal. The exposure time of the camera is set to 30 ms to ensure a 30 frames-per-second real-time video frame rate. Vials containing the different ICG concentrations are placed 60 cm from the custom NIR camera. They were illuminated with a 780-

nm laser at an optical power of 20 mW/cm<sup>2</sup>. The standard deviation ( $\sigma_c$ ) and mean value ( $\mu_c$ ) at concentration  $c$  mol/L (M) of a 10-pixel  $\times$  10-pixel ROI are calculated from the raw data.

The detection limit was defined by (6.6).

$$I_{limit} = I_0 + 3\sigma_0 \quad (6.6)$$

where  $I_{limit}$  is the photo response of the detection limit,  $I_0$  is the photo response of the reference sample, and  $\sigma_0$  is the standard deviation of the reference sample photo response. The fluorescence response of this imaging system is shown in Figure 6.6. The ICG concentration ranged from 500 pM to 10  $\mu$ M. The response is shown in a logarithm scale. Figure 6.6 shows a minimum detection limit of approximately 10 nM ICG under an excitation illumination of 20 mW/cm<sup>2</sup>.

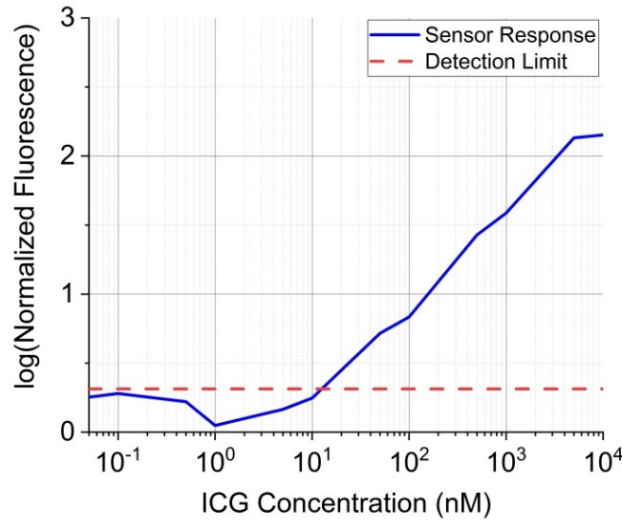


Figure 6.6 Contrast of the imaging system. The red line represents the contrast for each ICG concentration level. The horizontal blue line represents contrast equal to 2. The augmented reality system can detect as low as ~10 nM ICG under an excitation illumination of 20 mW/cm<sup>2</sup>.

### 6.4.2 Resolution Evaluation

To evaluate the resolution of the imaging system, I used the ISO 12233 test chart as an imaging target. The test chart is placed 60 cm from the camera and illuminated with a broad band light

source (OSL1, Thorlabs). A slant edge method is used to calculate the modulation transfer function (MTF) from the images acquired. The resolution is calculated by applying the Rayleigh criterion, which defines the resolution as the distance between two points that are resolved when the first minimum of one Airy disk is aligned with the central maximum of the second Airy disk. Under this criterion, the minimum resolvable distance corresponds to an MTF value of 26.4% [69].

Figure 6.7 shows the horizontal and vertical MTF. By applying the Rayleigh criterion, the resolution of my imaging system is 23.6 line pairs per millimeter along the horizontal direction and 29.8 line pairs per millimeter along the vertical direction.

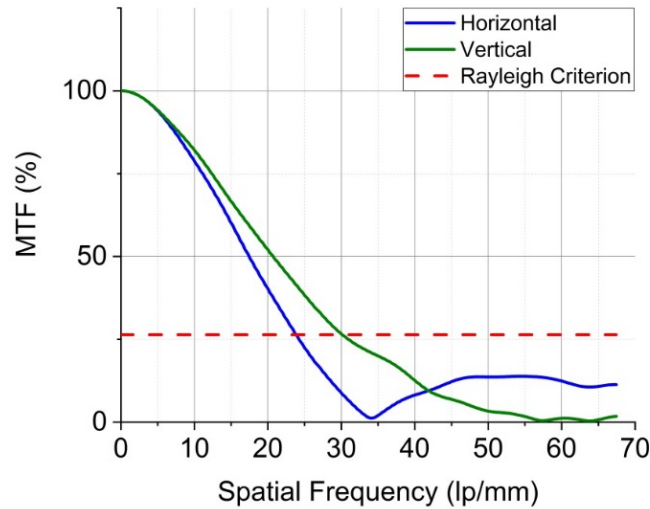


Figure 6.7 Horizontal and vertical modulation transfer function. The horizontal blue line represents the contrast under the Rayleigh criterion. The augmented reality system's resolution is 23.6 lp/mm and 29.8 lp/mm horizontally and vertically.

### 6.4.3 Co-Registration Evaluation

The co-registration calibrations are subject to errors, such as size mismatches of the initial calibration hologram and the calibration board, an inaccurate initial placement of calibration hologram and errors in LED tracking pod detection. These errors would accumulate, cause errors in the transformation matrix and affect the position of each pixel in the post-calibrated hologram.

However, because the user precedes the calibration after they are satisfied with the initial placement, these errors are negligible.

Because the hologram is a 2D plane superimposed on the calibration plane, the hologram of any non-planar real-world object would have additional co-registration errors with the user's natural vision. Figure 6.8 depicts the error model. The co-registration error ( $e_i$ ) between the real-world point  $P_i$  and the point indicated by the hologram  $P_i'$  is a function of both the height of the imaging object ( $h_i$ ) and the view angle of the user ( $\theta$ ). As the angle increased to 90 degrees, the error is minimized regardless of the height of the real-world object. When the user is looking at an angle between 0 degrees and 90 degrees, the error is calculated per (6.7):

$$e_i = \frac{h_i}{\tan \theta} \quad (6.7)$$

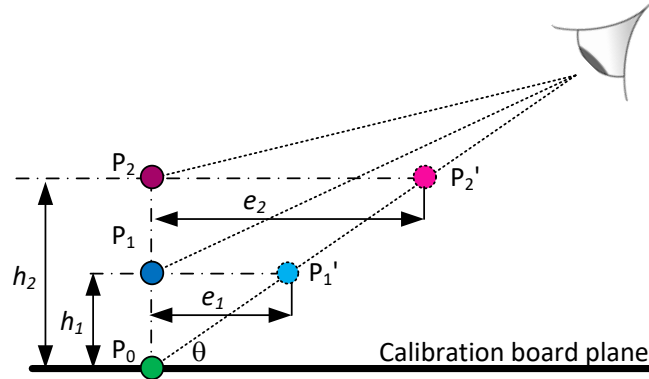


Figure 6.8 Co-registration error model. The error is a function of the target height and viewing angle.

Practically, the viewing angle is between 60 degrees and 90 degrees. When observed from a 90-degree angle, the error is minimized according to equation (6.7). To evaluate the maximum error, I used a black and white chessboard and a blue square target on the same plane to evaluate the co-registration error. The target is placed on the calibration board plane and then  $\pm 0.5$  cm,  $\pm 1$  cm,  $\pm 1.5$  cm, and  $\pm 2$  cm above/below the plane. The viewing angle is set to 60 degrees. I placed a web

camera behind the HoloLens optics to represent the user’s eye and to collect data. The web camera is pre-calibrated using the method described in [67]. A camera-to-world transformation matrix is acquired during the calibration. I computed the real-world coordinates of the blue square target and the holograms. The co-registration error is shown in Figure 6.9. The maximum error is approximately 12 mm.

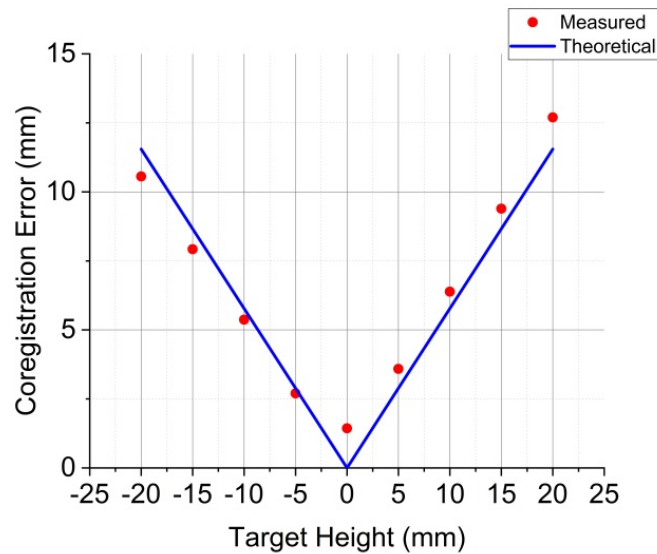


Figure 6.9 Co-registration error from a 60-degree viewing angle.

## 6.5 *In Vivo* and *Ex Vivo* Animal Study

The standard operating procedure for removing sentinel lymph nodes (SLNs) in veterinary surgery is to inject ICG into the lymphatic system. By tracking the visible green color of ICG, the physician removes the SLN relying on the unaided eyes. In this *in vivo* study, I used my head-mounted augmented reality system to help physicians locate SNLs by tracking NIR fluorescence emitted by ICG. The experiment is conducted at the University of Illinois Veterinary Teaching Hospital. Canine patients with head and neck cancer are imaged 20 minutes post-ICG injection. To maximize the fluorescence emission, the injected ICG dosage is diluted 20 times lower than typical



(0.5 mg/ml, inject 0.4 ml) to prevent fluorescence quenching. A 780-nm laser illuminated the surgical area (diameter = 20 cm) at 5 mW/cm<sup>2</sup> optical power.

Wearing the head-mounted augmented reality goggles, the physician detected SLNs with an overlaid jet color virtual image, indicating fluorescence intensity. As shown in Figure 6.10 (left), an image is captured by a second HoloLens from the physician's assistant's view. The same virtual images are displayed by two HoloLenses at the same position.

In the *ex vivo* study, the removed SNL was examined using the same optical and data acquisition setup. Figure 6.10 (right) shows that the virtual NIRF is correctly superimposed on the SNL.

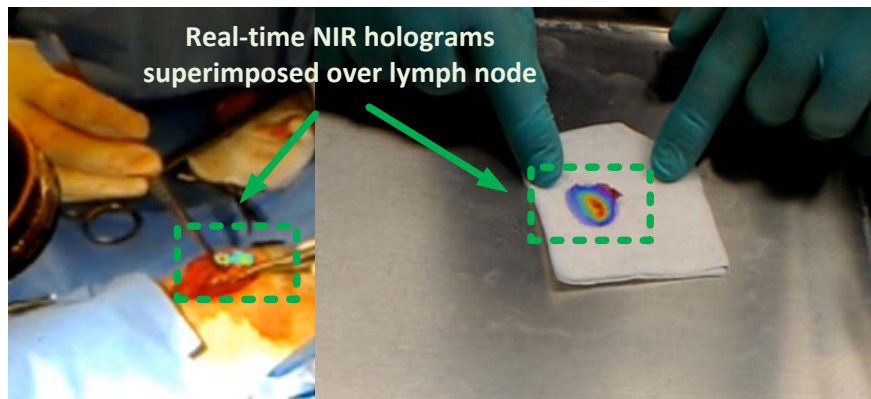


Figure 6.10 In vivo (left) and ex vivo (right) animal study for SNL removal assisted by the augmented reality HMD

## 6.6 Conclusions

In this chapter, I presented a head-mounted augmented reality system for NIRF image-guided surgery using a Microsoft HoloLens. The effectiveness of this technology is evaluated by *in vivo* and *ex vivo* animal studies. The holograms were correctly superimposed onto the lymph nodes and provided the physicians with real-time guidance during the surgery.

By using the augmented reality system, the physician was able to locate the 3-D anatomical features through the optics using their natural vision and see virtual holograms representing the

NIRF signal captured by my custom NIR camera. Compared with commercial NIRF imaging devices, this system is compact and wearable. Complex and heavy dichroic optical setups were replaced with a single CMOS camera. The NIRF was no longer displayed on the computer monitors, which would interfere with the surgical workflow. The virtual hologram was superimposed over anatomical features and correctly co-registered with the physician's natural vision using the calibration board and our co-registration algorithm. This guaranteed that the real-time data were co-registered after a one-time calibration process. To the best of my knowledge, this is the first HMD that co-registers a virtual image with human eyes and allows video rate image transmission. The comparison between commercial and state-of-the-art devices for IGS and this work is shown in Table 6.1.

Table 6.1 Summary and comparison between this augmented reality HMD and related work

<b>Description</b>	Display unit	Natural vision preserved?	Co-register with natural vision?	Real-time data?
<b>This work</b>	<b>HMD</b>	<b>Yes</b>	<b>Yes</b>	<b>Yes</b>
<b>Flare</b>	PC Monitor	No	No	Yes
<b>SPY</b>	PC Monitor	No	No	Yes
<b>PDE</b>	PC Monitor	No	No	Yes
<b>[51]</b>	PC Monitor	No	No	Yes
<b>[52]</b>	PC Monitor	No	No	Yes
<b>[53]</b>	PC Monitor	No	No	Yes
<b>[45]</b>	HMD	No	No	Yes
<b>[46]</b>	HMD	No	No	Yes
<b>[47]</b>	HMD	Yes	No	Yes
<b>[49]</b>	HMD	Yes	No	Yes
<b>[48]</b>	HMD	Yes	No	Yes
<b>[50]</b>	Half-silvered mirror	Yes	Yes	No

# **Chapter 7: Conclusions and Future Work**

## **7.1 Conclusions**

NIRF image-guided surgery is a powerful technique that helps the physician identify tumors for resection without damaging surrounding healthy tissue. State-of-the-art NIR fluorescence image-guided surgery instruments suffer from three critical problems: 1) they require multiple cameras and beam splitters to capture different wavelengths so that the instruments suffer from thermal expansion and non-deterministic co-registration error; 2) the intensities of the visible spectrum and the NIR spectrum span more than 5 orders of magnitude difference, and traditional CCD/CMOS sensors are unable to simultaneously capture this entire range; and 3) the display unit of these instruments is monitor-based. The physician cannot focus on the surgical area while performing surgery. These problems prevent the seamless integration of these instruments into the regular surgical workflow. In this dissertation, I presented bio-inspired sensing technologies and a display technology to solve the above-mentioned problems.

In Chapter 2, I reviewed the FDA regulation required specifications for intraoperative illumination and working condition of imaging systems. Based on the specifications, I analyzed the drawbacks of state-of-the-art FDA-approved instruments in depth.

Chapter 3 served as the major part of this dissertation. I investigated a bio-inspired multispectral CMOS logarithmic image sensor. The logarithmic image sensor has novel pixel architecture with forward-biased photodiodes. The novel architecture expands the physical limits of traditional 4-transistor CMOS image sensors, achieves a more than 140 dB dynamic range, and enables imaging fluorescence markers under surgical illumination with high sensitivity. Bio-inspired multispectral

filter array is monolithically integrated such that the temperature-dependent co-registration inaccuracy is removed.

In Chapter 4 I described our efforts to develop a time-domain PWM AER multispectral imaging system. The small foot print of the imaging system, coupled with the high dynamic range, and low cost can enable value-based health care in both resource-limited and resource-rich hospitals.

As explained in Chapter 5, I developed, designed and tested a compact, handheld, bio-inspired, single-chip, multispectral imaging device for image-guided cancer surgery. The image sensor is integrated with pixelated spectral filters. To further increase the DR, custom peripheral circuitry enables pixel wise control of light exposure. The compact form factor of my sensor enables both seamless integration of the sensor into the surgical suite and presentation of time-critical information to the physician.

Finally, I investigated the design of an augmented reality system for IGS using a Microsoft HoloLens platform. I integrated my image sensor with a holographic goggle platform to display real-time NIR fluorescent information to the physician. My key contribution is the accurate co-registration of NIR fluorescent information with the physician's natural eyesight. With the complete imaging and display system, the physician observes the patients with his or her natural eyesight, which is augmented with NIR information that highlights the location of the tumors.

Table 7.1 shows the comparison between this work and FDA-approved instruments. This work has addressed all the three major problems of FDA-approved instruments while maintain good benchmarks of other major performance indicators.

Table 7.1 Design Summary of this work and compression with the FDA-approved instruments.

Description	This work	Fluobeam	PDE	SPY Elite	Iridium	Spectrum
Designer	<b>Nan Cui</b>	FluoOptics	Hamamatsu	Novadaq	Vision Sense	Quest
FDA approved	<b>No</b>	Yes	Yes	Yes	Yes	Yes
Instrument type	<b>Single camera</b>	Single camera	Single camera	Two adjacent cameras	Beam splitter	Optical prism
Real-time color/NIR overlay	<b>Yes</b>	No	No	No	Yes	Yes
Surgical light	<b>On</b>	Dim	Dim	Dim	Dim	On
Sensor type	<b>Logarithmic CMOS</b>	CCD	CCD	CCD	CCD	CCD
Sensor bit depth	<b>14</b>	8	8	8	12	12
Exposure time	<b>Arbitrary</b>	1 ms to 1 s	NS	NS	NS	NS
Maximum FPS	<b>100</b>	25	20	20	NS	20
Sensor resolution	<b>302×240</b>	720 × 576	640 × 480	1024 × 768	960 × 720	1024 × 1024
Fluorescence Detection Limit	<b>~40nM</b>	~5nM	~15nM	~5nM	~50pM	~10nM
Display unit	<b>AR HMD</b>	monitor	Monitor	monitor	monitor	monitor

As the main contribution of this dissertation, the novel multispectral logarithmic CMOS image sensor has significant improvement over a state-of-the-art low-noise high-dynamic-range image sensor in major aspects, as shown in Table 7.2.

Table 7.2 The comparison between the major contribution of this dissertation and the state-of-the-art low-noise high-dynamic-range image sensor.

Description	This work	State-of-the-art	Improvement
# of transistors per pixel	down to 2	4	<b>Reduced 50%</b>
# of metal lines	down to 4	6	<b>Reduced 33%</b>
Dominant noise	equivalent thermal noise	photon shot noise	<b>Boost SNR</b>
Dynamic range	120dB logarithmic and more	95dB	<b>25dB and more</b>
Maximum SNR	56dB	45dB	<b>Increased 11dB</b>
Full well capacity	unlimited	450,000 electrons	<b>Boost DR</b>
Sensitivity	up to $\sim 6 \times 10^8 \mu\text{V}/(\text{mW}/\text{cm}^2)$	$\sim 2 \times 10^7 \mu\text{V}/(\text{mW}/\text{cm}^2)$	<b>~25 times</b>

## **7.2 Future Works**

This dissertation presented several technologies aimed at addressing problems with state-of-the-art NIRF IGS instruments. The proposed technologies have good optoelectronic performance and pre-clinical evaluation results. Nevertheless, these technologies are pre-production prototypes. To translate into mass production, additional work is required. For example, the pixel arrays of all image sensors should be expanded to higher resolutions, e.g., 1080p or 4k resolution. Such large arrays pose certain issues that would need to be addressed to produce readouts with desirable frame rates. More complex and optimized algorithms would have to be implemented for real-time image processing. Other important future work would be to extend the 2D augmented reality to 3D. To reconstruct a 3D surface of NIRF emission, 3D depth-sensing techniques such as time-of-flight or stereo image sensors should be incorporated.

# References

- [1] K. R. Yabroff, J. Lund, D. Kepka, and A. Mariotto, "Economic burden of cancer in the United States: estimates, projections, and future research," *Cancer Epidemiology and Prevention Biomarkers*, vol. 20, no. 10, pp. 2006-2014, 2011.
- [2] R. Siegel, J. Ma, Z. Zou, and A. Jemal, "Cancer statistics, 2014," *CA: a cancer journal for clinicians*, vol. 64, no. 1, pp. 9-29, 2014.
- [3] L. A. G. Ries *et al.*, "SEER cancer statistics review, 1975–2005," *Bethesda, MD: National Cancer Institute*, pp. 1975-2005, 2008.
- [4] B. A. Virnig, T. M. Tuttle, T. Shamliyan, and R. L. Kane, "Ductal carcinoma in situ of the breast: a systematic review of incidence, treatment, and outcomes," *Journal of the National Cancer Institute*, vol. 102, no. 3, pp. 170-178, 2010.
- [5] L. Jacobs, "Positive margins: the challenge continues for breast surgeons," *Annals of surgical oncology*, vol. 15, no. 5, pp. 1271-1272, 2008.
- [6] L. A. Ries *et al.*, "SEER cancer statistics review, 1975-2003," 2006.
- [7] M. L. Hinni *et al.*, "Surgical margins in head and neck cancer: a contemporary review," *Head & neck*, vol. 35, no. 9, pp. 1362-1370, 2013.
- [8] G. Moore, S. Hunter, and T. Hubbard, "Clinical and experimental studies of fluorescein dyes with special reference to their use for the diagnosis of central nervous system tumors," *Annals of surgery*, vol. 130, no. 4, p. 637, 1949.
- [9] W. Stummer *et al.*, "Fluorescence-guided surgery with 5-aminolevulinic acid for resection of malignant glioma: a randomised controlled multicentre phase III trial," *The lancet oncology*, vol. 7, no. 5, pp. 392-401, 2006.
- [10] S. Gioux, H. S. Choi, and J. V. Frangioni, "Image-guided surgery using invisible near-infrared light: fundamentals of clinical translation," *Molecular imaging*, vol. 9, no. 5, p. 7290.2010.00034, 2010.
- [11] A. L. Vahrmeijer, M. Hutteman, J. R. Van Der Vorst, C. J. Van De Velde, and J. V. Frangioni, "Image-guided cancer surgery using near-infrared fluorescence," *Nature reviews Clinical oncology*, vol. 10, no. 9, p. 507, 2013.
- [12] A. V. DSouza, H. Lin, E. R. Henderson, K. S. Samkoe, and B. W. Pogue, "Review of fluorescence guided surgery systems: identification of key performance capabilities beyond indocyanine green imaging," *Journal of biomedical optics*, vol. 21, no. 8, p. 080901, 2016.
- [13] Q. T. Nguyen and R. Y. Tsien, "Fluorescence-guided surgery with live molecular navigation—a new cutting edge," *Nature reviews cancer*, vol. 13, no. 9, p. 653, 2013.
- [14] N. Nishigori *et al.*, "Visualization of lymph/blood flow in laparoscopic colorectal cancer surgery by ICG fluorescence imaging (Lap-IGFI)," *Annals of surgical oncology*, vol. 23, no. 2, pp. 266-274, 2016.
- [15] M. Garcia *et al.*, "Bio-inspired imager improves sensitivity in near-infrared fluorescence image-guided surgery," *Optica*, vol. 5, no. 4, pp. 413-422, 2018/04/20 2018.
- [16] N. Cui *et al.*, "A 110× 64 150 mW 28 frames/s integrated visible/near-infrared CMOS image sensor with dual exposure times for image guided surgery," *IEEE Circuits and Systems*, pp. 101-104, 2016.
- [17] J. T. Alander *et al.*, "A review of indocyanine green fluorescent imaging in surgery," *Journal of Biomedical Imaging*, vol. 2012, p. 7, 2012.

- [18] S. Gao, S. B. Mondal, N. Zhu, R. Liang, S. Achilefu, and V. Gruev, "Image overlay solution based on threshold detection for a compact near infrared fluorescence goggle system," *Journal of biomedical optics*, vol. 20, no. 1, p. 016018, 2015.
- [19] S. B. Mondal *et al.*, "Optical see-through cancer vision goggles enable direct patient visualization and real-time fluorescence-guided oncologic surgery," *Annals of surgical oncology*, vol. 24, no. 7, pp. 1897-1903, 2017.
- [20] N. Zhu *et al.*, "Compact wearable dual-mode imaging system for real-time fluorescence image-guided surgery," *Journal of biomedical optics*, vol. 20, no. 9, p. 096010, 2015.
- [21] S. B. Mondal *et al.*, "Binocular Goggle Augmented Imaging and Navigation System provides real-time fluorescence image guidance for tumor resection and sentinel lymph node mapping," *Scientific reports*, vol. 5, p. 12117, 2015.
- [22] K. Sexton, K. Tichauer, K. S. Samkoe, J. Gunn, P. J. Hoopes, and B. W. Pogue, "Fluorescent affibody peptide penetration in glioma margin is superior to full antibody," *PloS one*, vol. 8, no. 4, p. e60390, 2013.
- [23] J. Sørensen *et al.*, "First-in-human molecular imaging of HER2 expression in breast cancer metastases using the <sup>111</sup>In-ABY-025 affibody molecule," *Journal of nuclear medicine*, vol. 55, no. 5, pp. 730-735, 2014.
- [24] S. B. Lee *et al.*, "Affibody molecules for in vivo characterization of HER2-positive tumors by near-infrared imaging," *Clinical Cancer Research*, vol. 14, no. 12, pp. 3840-3849, 2008.
- [25] C. H. Heath, N. L. Deep, L. Sweeny, K. R. Zinn, and E. L. Rosenthal, "Use of panitumumab-IRDye800 to image microscopic head and neck cancer in an orthotopic surgical model," *Annals of surgical oncology*, vol. 19, no. 12, pp. 3879-3887, 2012.
- [26] E. L. Rosenthal *et al.*, "Safety and tumor specificity of cetuximab-IRDye800 for surgical navigation in head and neck cancer," *Clinical Cancer Research*, vol. 21, no. 16, pp. 3658-3666, 2015.
- [27] J. Sørensen *et al.*, "Measuring HER2-receptor expression in metastatic breast cancer using [<sup>68</sup>Ga] ABY-025 Affibody PET/CT," *Theranostics*, vol. 6, no. 2, p. 262, 2016.
- [28] L. Ries *et al.*, "SEER Cancer Statistics Review, 1975–2005. National Cancer Institute; Bethesda, MD: 2008," Available at: [seer.cancer.gov/csr/1975-2001/](http://seer.cancer.gov/csr/1975-2001/), 2007.
- [29] M. Garcia, M. A. Zayed, K.-m. Park, and V. Gruev, "Near-infrared angiography for critical limb ischemia in a diabetic murine model," *Journal of biomedical optics*, vol. 22, no. 4, p. 046006, 2017.
- [30] M. Garcia, M. Zayed, K.-m. Park, and V. Gruev, "A 1600 by 1200, 300 mW, 40 fps multi-spectral imager for near-infrared fluorescence image-guided surgery," in *Circuits and Systems (ISCAS), 2017 IEEE International Symposium on*, 2017, pp. 1-4: IEEE.
- [31] M. Zimny *et al.*, "2-[Fluorine-18]-fluoro-2-deoxy-d-glucose positron emission tomography in the diagnosis of recurrent ovarian cancer," *Gynecologic oncology*, vol. 83, no. 2, pp. 310-315, 2001.
- [32] S. L. Troyan *et al.*, "The FLARE™ intraoperative near-infrared fluorescence imaging system: a first-in-human clinical trial in breast cancer sentinel lymph node mapping," *Annals of surgical oncology*, vol. 16, no. 10, pp. 2943-2952, 2009.
- [33] M. Takahashi, T. Ishikawa, K. Higashidani, and H. Katoh, "SPY™: an innovative intra-operative imaging system to evaluate graft patency during off-pump coronary artery bypass grafting," *Interactive cardiovascular and thoracic surgery*, vol. 3, no. 3, pp. 479-483, 2004.



- [34] N. Tagaya *et al.*, "Intraoperative identification of sentinel lymph nodes by near-infrared fluorescence imaging in patients with breast cancer," *The American Journal of Surgery*, vol. 195, no. 6, pp. 850-853, 2008.
- [35] C. Posch, D. Matolin, and R. Wohlgenannt, "A QVGA 143 dB dynamic range frame-free PWM image sensor with lossless pixel-level video compression and time-domain CDS," *IEEE Journal of Solid-State Circuits*, vol. 46, no. 1, pp. 259-275, 2011.
- [36] R. King *et al.*, "Band gap - voltage offset and energy production in next - generation multijunction solar cells," *Progress in Photovoltaics: Research and Applications*, vol. 19, no. 7, pp. 797-812, 2011.
- [37] B. Razavi, *Design of analog CMOS integrated circuits*. 清华大学出版社有限公司, 2001.
- [38] G. Inc. *GSENSE2020BSI*. Available: <http://www.gpixelinc.com/en/index.php?s=/b/104.html>
- [39] A. Van der Ziel, "Noise. Sources, characterization, measurement," *Prentice-Hall Information and System Sciences Series, Englewood Cliffs: Prentice-Hall*, 1970, 1970.
- [40] M. Garcia *et al.*, "Bio-inspired imager improves sensitivity in near-infrared fluorescence image-guided surgery," *Optica*, vol. 5, no. 4, pp. 413-422, 2018.
- [41] S. Kavadias, B. Dierickx, D. Scheffer, A. Alaerts, D. Uwaerts, and J. Bogaerts, "A logarithmic response CMOS image sensor with on-chip calibration," *IEEE Journal of Solid-state circuits*, vol. 35, no. 8, pp. 1146-1152, 2000.
- [42] G. Storm, R. Henderson, J. Hurwitz, D. Renshaw, K. Findlater, and M. Purcell, "Extended dynamic range from a combined linear-logarithmic CMOS image sensor," *IEEE Journal of Solid-State Circuits*, vol. 41, no. 9, pp. 2095-2106, 2006.
- [43] L.-W. Lai, C.-H. Lai, and Y.-C. King, "A novel logarithmic response CMOS image sensor with high output voltage swing and in-pixel fixed-pattern noise reduction," *IEEE Sensors Journal*, vol. 4, no. 1, pp. 122-126, 2004.
- [44] S. Decker, D. McGrath, K. Brehmer, and C. G. Sodini, "A 256/spl times/256 CMOS imaging array with wide dynamic range pixels and column-parallel digital output," *IEEE Journal of solid-state circuits*, vol. 33, no. 12, pp. 2081-2091, 1998.
- [45] P. Lichtsteiner, C. Posch, and T. Delbruck, "A 128 $\times$ 128 120 dB 15 $\mu$ s Latency Asynchronous Temporal Contrast Vision Sensor," *IEEE journal of solid-state circuits*, vol. 43, no. 2, pp. 566-576, 2008.
- [46] A. E. Profio, O. J. Balchum, and F. Carstens, "Digital background subtraction for fluorescence imaging," *Medical physics*, vol. 13, no. 5, pp. 717-721, 1986.
- [47] A. D. McNaught and A. D. McNaught, *Compendium of chemical terminology*. Blackwell Science Oxford, 1997.
- [48] B. Zhu, J. C. Rasmussen, and E. M. Seveck - Muraca, "A matter of collection and detection for intraoperative and noninvasive near - infrared fluorescence molecular imaging: To see or not to see?," *Medical physics*, vol. 41, no. 2, 2014.
- [49] Q. Chen *et al.*, "A CMOS image sensor integrated with plasmonic colour filters," *Plasmonics*, vol. 7, no. 4, pp. 695-699, 2012.
- [50] A. Lambrechts, P. Gonzalez, B. Geelen, P. Soussan, K. Tack, and M. Jayapala, "A CMOS-compatible, integrated approach to hyper-and multispectral imaging," in *Electron Devices Meeting (IEDM), 2014 IEEE International*, 2014, pp. 10.5. 1-10.5. 4: IEEE.
- [51] L. Frey *et al.*, "Color filters including infrared cut-off integrated on CMOS image sensor," *Optics express*, vol. 19, no. 14, pp. 13073-13080, 2011.

- [52] N. Zhu, S. B. Mondal, S. Gao, S. Achilefu, V. Gruev, and R. Liang, "Engineering light-emitting diode surgical light for near-infrared fluorescence image-guided surgical systems," *Journal of biomedical optics*, vol. 19, no. 7, p. 076018, 2014.
- [53] J. A. Hanley and B. J. McNeil, "A method of comparing the areas under receiver operating characteristic curves derived from the same cases," *Radiology*, vol. 148, no. 3, pp. 839-843, 1983.
- [54] R. Weissleder and M. J. Pittet, "Imaging in the era of molecular oncology," *Nature*, vol. 452, no. 7187, p. 580, 2008.
- [55] F. P. Verbeek *et al.*, "Intraoperative near infrared fluorescence guided identification of the ureters using low dose methylene blue: a first in human experience," *The Journal of urology*, vol. 190, no. 2, pp. 574-579, 2013.
- [56] B. E. Schaafsma *et al.*, "The clinical use of indocyanine green as a near - infrared fluorescent contrast agent for image - guided oncologic surgery," *Journal of surgical oncology*, vol. 104, no. 3, pp. 323-332, 2011.
- [57] E. Sevick-Muraca, "Translation of near-infrared fluorescence imaging technologies: emerging clinical applications," *Annual review of medicine*, vol. 63, pp. 217-231, 2012.
- [58] A. Taruttis and V. Ntziachristos, "Translational optical imaging," *American Journal of Roentgenology*, vol. 199, no. 2, pp. 263-271, 2012.
- [59] K. E. Adams *et al.*, "Comparison of visible and near-infrared wavelength-excitable fluorescent dyes for molecular imaging of cancer," *Journal of biomedical optics*, vol. 12, no. 2, p. 024017, 2007.
- [60] Y. Liu *et al.*, "Intraoperative detection of liver tumors aided by a fluorescence goggle system and multimodal imaging," *Analyst*, vol. 138, no. 8, pp. 2254-2257, 2013.
- [61] D. G. Armstrong, T. M. Rankin, N. A. Giovinco, J. L. Mills, and Y. Matsuoka, "A heads-up display for diabetic limb salvage surgery: a view through the google looking glass," *Journal of diabetes science and technology*, vol. 8, no. 5, pp. 951-956, 2014.
- [62] P. Shao *et al.*, "Designing a wearable navigation system for image-guided cancer resection surgery," *Annals of biomedical engineering*, vol. 42, no. 11, pp. 2228-2237, 2014.
- [63] H. Liao, T. Inomata, I. Sakuma, and T. Dohi, "3-D augmented reality for MRI-guided surgery using integral videography autostereoscopic image overlay," *IEEE transactions on biomedical engineering*, vol. 57, no. 6, pp. 1476-1486, 2010.
- [64] N. Haouchine, J. Dequidt, I. Peterlik, E. Kerrien, M.-O. Berger, and S. Cotin, "Image-guided simulation of heterogeneous tissue deformation for augmented reality during hepatic surgery," in *Mixed and Augmented Reality (ISMAR), 2013 IEEE International Symposium on*, 2013, pp. 199-208: IEEE.
- [65] G. Badiali *et al.*, "Augmented reality as an aid in maxillofacial surgery: validation of a wearable system allowing maxillary repositioning," *Journal of Cranio-Maxillo-Facial Surgery*, vol. 42, no. 8, pp. 1970-1976, 2014.
- [66] X. Kang *et al.*, "Stereoscopic augmented reality for laparoscopic surgery," *Surgical endoscopy*, vol. 28, no. 7, pp. 2227-2235, 2014.
- [67] Z. Zhang, "A flexible new technique for camera calibration," *IEEE Transactions on pattern analysis and machine intelligence*, vol. 22, no. 11, pp. 1330-1334, 2000.
- [68] J. Canny, "A computational approach to edge detection," in *Readings in Computer Vision*: Elsevier, 1987, pp. 184-203.

- [69] G. Themelis, J. S. Yoo, K. Soh, R. B. Schulz, and V. Ntziachristos, "Real-time intraoperative fluorescence imaging system using light-absorption correction," *Journal of biomedical optics*, vol. 14, no. 6, p. 064012, 2009.